Large–scale MIMO Textile Technology for Enhanced Terminals

by

Estefanía Crespo Bardera

A dissertation submitted in partial fulfillment of the requirements for the degree of Doctor of Philosophy in

Multimedia and Communication Interuniversity PhD Program

Universidad Carlos III de Madrid

Advisor and tutor:

Dra. Matilde Pilar Sánchez Fernández

July 2019

A mi familia.

Acknowledgements

Comenzaré agradeciendo a mis padres y a mi hermana su apoyo incondicional a lo largo de mi vida, y en especial durante esta etapa de mis estudios de doctorado. Gracias por estar en los momentos buenos y en los no tan buenos, gracias por vuestras palabras de ánimo y alegraros de cada uno de mis logros personales.

Agradecer también a otro de mis apoyos fundamentales durante esta etapa, mis compañeros y amigos, con los que tantos buenos momentos he compartido, entre ellos nuestros coffees diarios que tanto voy a echar de menos. Pablo, gracias por tus consejos y paciencia. Lore, siempre dispuesta a escuchar y ayudar, gracias. Iratxe, no sólo compartiste conmigo la primera etapa de mis estudios en la que fuiste un gran apoyo, sino también nuestras clases de zumba o nuestras meriendas dulces. Por último, pero no menos importantes, mis compañeros de despacho y de comidas diarias, especialmente Juan Carlos, Alberto y Borja.

Durante mi estancia en Chile, agradecer a todos por el trato excepcional que me dieron, pero especialmente a Manolo al que aprecio mucho y con el que lo pasé genial. Gracias por hacerme ver que es posible seguir viendo la parte positiva de las cosas aunque no siempre sea fácil.

A Eva, por su disposicíon para ayudarme con el diseño de antenas, así como sus palabras de ánimo y consejos cuando las cosas no parecían fáciles.

Quizás me olvido de mencionar a mucha gente, Ángel, Jesús, Aarón, ... personas de distintos lugares que siempre han estado ahí y que de alguna manera, también me han apoyado durante esta etapa.

Finalmente, a mi tutora, Mati, tengo que agradecerle su paciencia, apoyo y comprensión durante estos años, así como todas las oportunidades que me ha dado, entre ellas participar en proyectos de investigación enriquecedores, así como realizar estancias internacionales que puedo decir que me han enriquecido mucho como persona.

Published and submitted content

Journal Papers

- E. Crespo-Bardera, M. Rodríguez, M. Sánchez-Fernández, E. Rajo-Iglesias, R. Feick, and R. A. Valenzuela, "Empirical Rates Characterization of Wearable Multiantenna Terminals for First-Responders," IEEE Access, vol. 7, pp. 6990–7000, 2019.

  This article is wholly included in the Thesis. Specifically, the content has been included in Chapter 3 and it is not singled out with typographic means and references.

- E. Crespo-Bardera, A. Vega Delgado, A. Garrido Martín, A. Fernández-Durán, and M. Sánchez-Fernández, "Textile Multiantenna Technology and Relaying Architectures for Emergency Networks," Wireless Communications and Mobile Computing, vol. 2019, 2019.

  This article is wholly included in the Thesis. Specifically, the content has been included in Chapter 4 and it is not singled out with typographic means and references.

- E. Crespo-Bardera, A. Garrido Martín, A. Fernández-Durán, E. Rajo-Iglesias, and M. Sánchez-Fernández, "Design and Analysis of Conformal Antenna for Future Public Safety Communications," IEEE Antennas and Propagation magazine, in mess 2019.

  This article is wholly included in the Thesis. Specifically, the content has been included in Chapter 2 and it is not singled out with typographic means and references.

Conference Papers

- E. Crespo-Bardera, M. Sánchez-Fernández, A. Garcia-Armada, A. G. Martín, and A. F. Durán, "Analysis of a LTE-Based Textile Massive MIMO Proposal for Public Safety Networks," IEEE 86th Vehicular Technology Conference (VTC-Fall), pp. 1–5, 2017.

  This article is wholly included in the Thesis. Specifically, the content has been included in Chapter 4 and it is not singled out with typographic means and references.

Other research merits

- E. Crespo-Bardera, M. Sánchez-Fernandez, L. A. Talegón, and A. V. Delgado, "Feasibility of a Wearable Textile Antenna Hub based on Massive MIMO Systems," 2016 18th Mediterranean Electrotechnical Conference (MELECON), pp. 1–6, 2016.

Abstract

The increasing demand for higher data rates imposed by the next generation of wireless communication networks has postulated Multiple-Input Multiple-Output (MIMO) systems as one of the main technological solutions. While the development of a large number of antennas is relatively feasible at the base station (BS) side due to the available space, it is not so viable at the end user side. Therefore, the user end can be considered as a clear bottle–neck of the communication since in MIMO systems the throughput gains are limited by the minimum number of antennas existing at the transmitter or the receiver. With the aim of overcoming this limitation, in this Thesis textile multi–antenna based terminals are presented. Specifically, the textile solution based on large–scale MIMO technology explored in this work allows to provide the energy and spectral efficiency benefits offered by MIMO technology directly to the end user (e.g. exploiting their own garments or accessories) without compromising the size, weight and, ultimately the portability of the user equipment (UE).

Motivated with the aforementioned target, the main results provided by this Thesis can be classified in three.

First, the design, fabrication and experimental characterization of different textile antenna arrays is performed. Concretely, one design is developed to be integrated at the backside of a jacket operating at 3.5 GHz, while the other design is developed to be conformed in a helmet operating at 4.9 GHz. Additionally, due to the fact that the textile solution is developed to work in the very close proximity of the human body, offering information regarding the human exposure to electromagnetic fields (EMF) seems to be relevant. Thus, an study to quantify the specific absorption rate (SAR) is also performed. It should be noted that these designs can be applied to emergency scenarios, where first responders can improve their communication capabilities with the deployment of a large number of antennas in their garments.

Second, carrying out the experimental characterization of the performance in terms of achievable rates for a textile multi–antenna terminal in order to show the real advantages

of deploying a large number of antennas at the user end. With that objective, a measurement campaign that allows to model the wireless channel in relevant Outdoor-to-Indoor (O2I) propagation environments was performed in Valparaíso (Chile).

Finally, the third part of this Thesis pretends to evaluate the role that textile multi–antenna terminals might play as a part of future public safety network solutions. To this end, a two–hop link network proposal based on advanced long–term evolution (LTE) standard is also proposed. Among other things, the device technology and the network elements required to implement such a network concept, as well as, a possible design principle based on the reliable connectivity principle required by emergency communications, are presented.

Contents

List of Figures

List of Tables

Acronyms

1G	1^{st} **G**eneration of Mobile Communications
2G	2^{nd} **G**eneration of Mobile Communications
3G	3^{rd} **G**eneration of Mobile Communications
4G	4^{th} **G**eneration of Mobile Communications
5G	5^{th} **G**eneration of Mobile Communications
ABS	**A**crylonitrile **B**utadiene **S**tyrene
AF	**A**mplify–and–**F**orward
AWGN	**A**dditive **W**hite **G**aussian **N**oise
BS	**B**ase **S**tation
CCDF	**C**omplementary **C**umulative **F**unction **D**istribution
CDF	**C**umulative **F**unction **D**istribution
CSIT	**C**hannel **S**tate **I**nformation at the **T**ransmitter
CST MWS	**C**ST **M**icrowave **S**tudio
dB	**D**ecibels
DOA	**D**irection **O**f **A**rrival
DOD	**D**irection **O**f **D**eparture
DRR	**D**isaster **R**isk **R**eduction
EDGE	**E**nhanced **D**ata Rates for **G**SM **E**volution
EMF	**E**xposure to **E**lectromagnetic **F**ields
ERP	**E**ffective **R**adiated **P**ower
FCC	**F**ederal **C**ommunications **C**ommission
FDMA	**F**requency **D**ivision **M**ultiple **A**ccess
FFT	**F**ast **F**ourier **T**ransform
GPRS	**G**eneral **P**acket **R**adio **S**ystem
GPS	**G**lobal **P**ositioning **S**ystem

GSM	**G**lobal **S**ystem for **M**obile
GSMC	**G**eometry–based **S**tochastic **C**hannel **M**odel
HSDPA	**H**igh **S**peed **D**ownlink **P**acket **A**ccess
HSUPA	**H**igh **S**peed **U**plink **P**acket **A**ccess
I2I	**I**ndoor–to–**I**ndoor
IEC	European **I**nternational **E**lectrotechnical **C**ommission
IP	**I**nternet **P**rotocol
ISM	**I**ndustrial **S**cientific and **M**edical
KS	**K**olmogorov–**S**mirnov
LOS	**L**ine–**O**f–**S**ight
LS	**L**east **S**quares
LTE	**L**ong **T**erm **E**volution
LTE-A	**L**ong **T**erm **E**volution **A**dvance
MC	**M**utual **C**oupling
MIMO	**M**ultiple **I**nput **M**ultiple **O**utput
MISO	**M**ultiple **I**nput **S**ingle **O**utput
MLE	**M**aximum **L**ikelihood **E**stimation
MSE	**M**ean **S**quare **E**rror
NLOS	**N**on–**L**ine–**O**f–**S**ight
No–CSIT	**N**o **C**hannel **S**tate **I**nformation at the **T**ransmitter
O2I	**O**utdoor–to–**I**ndoor
O2O	**O**utdoor–to–**O**utdoor
PAS	**P**ower **A**ngular **S**pread
PDF	**P**robability **D**ensity **F**unction
PL	**P**ath–**L**oss
PMR	**P**rivate **M**obile **R**adio
RMSE	**R**oot **M**ean **S**quare **E**rror
RN	**R**elay **N**ode
SAM	**S**pecific **A**nthropomorphic **M**annequin
SAR	**S**pecific **A**bsorption **R**ate
SMA	**S**ubminiature version **A**
SF	**S**hadow **F**ade
SIMO	**S**ingle–**I**nput–**M**ultiple–**O**utput

SISO	**S**ingle–**I**nput–**S**ingle–**O**utput
SNR	**S**ignal–to–**N**oise **R**atio
SP4T	**S**ingle–**P**ole **F**our–**T**hrow
SVD	**S**ingular **V**alue **D**ecomposition
TAC	**T**otal **A**ccess **C**ommunication System
TDD	**T**ime **D**ivision **D**uplexing
TDMA	**T**ime **D**ivision **M**ultiple **A**ccess
UE	**U**ser **E**quipment
UMTS	**U**niversal **M**obile **T**elecommunication **S**ystem
UTFSM	**U**niversidad **T**écnica **F**ederico **S**anta **M**aría
UWB	**U**ltra–**W**ideband
VNA	**V**ector **N**etwork **A**nalyzer
WCDMA	**W**ideband **C**ode Division **M**ultiple **A**ccess
WF	**W**ater **F**illing
WiMAX	**W**orldwide **I**nteroperability for **M**icrowave **A**ccess
WLAN	**W**ireless **L**ocal **A**rea **N**etwork

Notation

a	Scalar.
$\mathbf{a}$	Vector.
$\mathbf{A}$	Matrix.
$\mathbf{A}^{-1}$	Inverse of the matrix $\mathbf{A}$.
$\mathbf{A}^{\dagger}$	Transpose and complex conjugate of the matrix $\mathbf{A}$.
$\mathbf{I}$	Identity matrix of the appropriate dimensions.
$\mathrm{Tr}\left\{.\right\}$	Trace operation.
$\mathrm{Tr}\left(\mathbf{I}\right)$	Identity matrix of the appropriate dimensions.
$\mathbf{A} \otimes \mathbf{B}$	Kronecker product of the matrices $\mathbf{A}$ and $\mathbf{B}$.
$\mathbb{E}\left\{\cdot\right\}$	Statistical expectation.
$\left\|.\right\|_F^2$	Square Frobenius norm.
$\log_2\left(\cdot\right)$	Base 2 logarithm.
$\mathrm{vec}\left(\mathbf{A}\right)$	Vectorization of the matrix $\mathbf{A}$.

Chapter 1

Introduction

Hitherto, mobile communications have been classified in different generations depending on their degree of technical evolution directly related to the way in which users communicate, access information and consequently the greater requirements for wireless communication systems. Each generation presents novel techniques, standards and capacities that differ from the previous one (see Fig. 1.1). A summary of the most important features in each generation is given below [1].

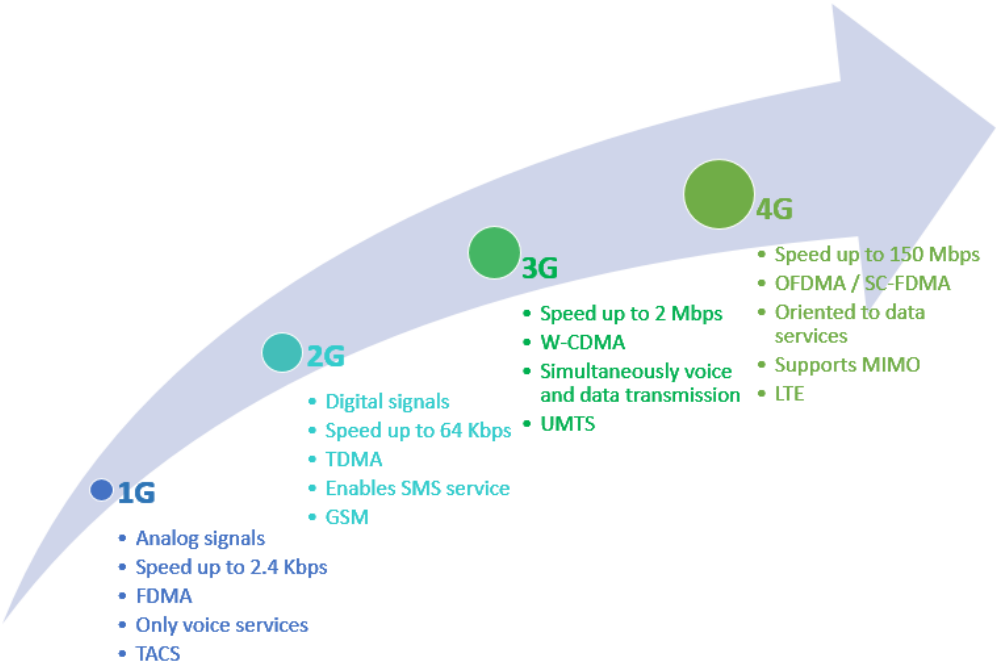

FIGURE 1.1: Mobile generations (1G-4G) and its main features.

The first generation (1G) of mobile communications offered only voice–centric services based on analog technology. Depending on the country different technological proposals

were presented. In Spain, Total Access Communication System (TAC) was adopted. It used Frequency Division Multiple Access (FDMA) with channels of 30 KHz, where each user consumes the whole available bandwidth leading to a limited number of uses derived from the low spectrum efficiency.

The second mobile generation (2G) mainly differs from the previous one in the use of digital technology for voice transmission and Time Division Multiple Access (TDMA), allowing in this way to increment the number of users and reduce the devices cost. In Europe, it was defined in the Global System for Mobile (GSM) standard which was permanently improved in order to offer better services giving rise to diverse technological solutions such as General Packet Radio System (GPRS) and Enhanced Data Rates for GSM Evolution (EDGE) known as 2.5G.

Probably, it can be considered that one of the greatest changes in terms of spectral efficiency came from the third mobile generation (3G), in Europe determined by the Universal Mobile Telecommunication System (UMTS) standard. A novel radio access scheme known as Wideband Code Division Multiple Access (W-CDMA) was proposed. It assigns each user a different code enabling this way users to transmit at the same time using the same carrier frequency. It is worth mentioning that this technology has also had different evolutions such as High Speed Downlink Packet Access (HSDPA) and High Speed Uplink Packet Access (HSUPA).

The fourth generation of mobile communications (4G) came with Long Term Evolution (LTE) and was later improved by Long Term Evolution–Advanced (LTE–A). It arose from the need to create an all–Internet Protocol (IP) communications system in which all services, including voice, were treated as data packets. Once again, to meet the incessant demands of spectral and power efficiency, technological solutions such as Multiple–Input Multiple–Output (MIMO) or new accessing techniques like Orthogonal Frequency Division Multiple Access (OFDMA) for downlink transmission and Single Carrier Frequency Division Multiple Access (SC–FDMA) for uplink transmission were proposed.

Currently, there is a huge proliferation of smart devices (e.g., smart glasses, smart watches, tablets, smartphones, etc.) and multimedia services (e.g., E-health, virtual reality, tactile internet) that has significantly transformed the classical concept of consumption and interaction with digital resources and that consequently has given rise to

an exponential demand of higher data rates. Unlimited access to information with data exchange anywhere or anytime arises as a novel trend forcing again to the evolution of mobile wireless communications towards the fifth generation (5G).

5G mobile generation refers to the next technological solutions beyond the current 4G mobile generation that will enable the following system requirements [2–4]:

- Higher data rates ranging from 1 up to 10 Gbps.
- Very low latency (1 ms). Almost 10 times lower than that offered by the previous mobile generation.
- High power efficiency.
- High density of devices simultaneously connected.
- Full coverage and almost 100% availability.

Taking these challenging requirements as a baseline, researchers and industries are collaborating together in order to find the specify technological solutions that enable to cope 5G performance. Concretely, in this Thesis the main goal is focused on looking for a technological solution that allows to deal with the requirement of offering higher data rates. Before presenting our technological proposal, it is important to understand how the data rates offered by mobile communication networks can be increased. There are three primary forms [2]: *i)* network densification to improve the area spectral efficiency (more nodes per unit area and Hz), *ii)* make better use of unlicensed spectrum in the low bands below 6 GHz (more Hz) or expanding the available spectrum by moving towards mm-Wave spectrum and finally, *iii)* increase the spectral efficiency through large-scale antenna systems, also known as MIMO systems (more bits/s/Hz). Focusing on the latest possibility, it should be noticed that the deployment of a large number of antennas may require structural changes in the user equipments and base stations [5]. In particular, the design of MIMO-based technological solutions should deal with some important restrictions imposed by the user end [6] like the very limited space to deploy a large number of antennas, the light weight or the cost, that converts the user end in a clear bottle neck within the communications link (from the achievable rate gains perspective).

Therefore, the main objective of this dissertation consists of evading the aforementioned bottle-neck and the problem of increasing the size and weight of the device by deploying a large number of antennas at the user terminal by means of textile technology. This technological solution will enable the achievement of symmetric data rates (in both uplink and downlink), and minimize the impact on the base station since it will be developed directly on the end user (i.e. exploiting their accessories or own clothing).

Another important aspect that adds value to the proposed textile solution, is that its design can be easily adapted to any frequency specification. Specifically, in this dissertation we focus on three different frequency bands (2.5 GHz, 3.5 GHz and 4.9 GHz) that are expected to be part of those assigned to future public safety communications, which are the case of application analyzed in this Thesis. As we will see in Chapter 4, such communications are currently conveyed through narrow band systems that cannot offer the high throughput requirements that future public safety communications will require. Specifically, the basic features of the three different designs that will appear throughout this Thesis are summarized in Table 1.1.

TABLE 1.1: Basic features of the textile multi–antenna terminals studied in this Thesis.

Working Frequency	2.5 GHz	3.5 GHz	4.9 GHz
Planar array size	$8 \times 5 = 40$	$6 \times 2 = 12$	$1 \times 4 = 4$
Inter–element distance	0.66λ	0.7λ	0.6λ
Dielectric substrate	Common felt	Common felt	Common felt
Metallization	Electrotextile material	Electrotextile material	Electrotextile material
Total array perimeter	2104 mm	1060 mm	400.44 mm
Place of deployment	Backside of a jacket	Backside of a jacket	Conformed in a helmet

As it is observed, two of them are specifically design to be deployed at the backside of a jacket while the other is a conformal array specifically designed to be integrated in a safety helmet. It should be noticed that the textile antenna array operating at 2.5 GHz had been previously designed before the beginning of this Thesis [7] and has been the seed for part of the research undertaken. In particular, in Chapter 4 we make use of its simulated performance in order analyze the benefits it may offer to future public safety communications.

1.1 Motivation and Contributions

This Thesis introduces a technological solution which pretends to offer an always-on connectivity with reliable high data rates anywhere, anytime, approaching recent and future communication necessities. Indeed, it should be considered as a feasibility study of the deployment of a large number of textile antennas at the user's end.

The main contributions are summarized as follows:

- Design, manufacture and empirical characterization of textile antenna arrays at different operating frequencies. Moreover, an analysis of the human exposure to electromagnetics waves is performed.
- Experimental channel characterization of a $6 \times 2 = 12$ textile multi–antenna terminal operating at 3.5 GHz to corroborate the rate performance of the textile-based solution. To this end, the empirical channel modeling of relevant propagation scenarios from the communications perspective is performed.
- A LTE-based network solution in which the textile multi–antenna terminal directly implemented at the user end is envisioned to be responsible for a physical layer improvement. Specifically, the main goal of the network solution based on two-hop links that seeks to reach locations with low coverage, consists of providing rescuers with a reliable connectivity that allows them the exchange multimedia information that.

1.2 Organization

Chapter 1 is introductory and brings us closer to the specific problems of wireless communication systems whose requirements are becoming more strict. Furthermore, the motivation and objectives of this Thesis are included. Chapter 2 presents the foundations about antenna designs as well as about textile technology. Additionally, the design, fabrication and empirical characterization of different textile antenna arrays developed in this Thesis are explored. In Chapter 3 the main goal consists of empirically characterizing the propagation channel and rate performance of a textile multi–antenna terminal in order to show the real benefits it can offer. To this end, in this chapter the required

theoretical background, the methodology and the results of the statistical modeling relevant for the rates estimation are provided. All the statistical models are obtained for particular Outdoor–to–Indoor (O2I) propagation scenarios where the user equipment (UE) is placed underground. Chapter 4 envisions the textile solution as a key enabler for future public safety wireless communications. Concretely, this chapter envisions as a technological solution the integration of textile multi–antenna terminals directly implemented on rescuer garments within a potential LTE network scenario. Specifically, the LTE-based network is designed to serve in emergency scenarios and eventually consider a two-hop architecture based on relaying, to provide reliable broadband services in scenarios with null or very low coverage. Finally, Chapter 5 shows the general conclusions of this Thesis and the proposed directions for future work.

Chapter 2

Textile MIMO Antennas for the User End

This chapter presents two wearable antenna models developed in this Thesis with the aim of providing solutions to the increasing demand for high data rates in cellular networks. A third design, is also going to be used in this Thesis (Chapter 4), however it is not detailed here since the design was already presented in [7]. In any case, all the designs are tailored to be directly deployed on the user side overcoming typical single-antenna communication scenarios and taking advantage of MIMO technology benefits.

The first design, a $1 \times 4 = 4$ conformal textile antenna, to be deployed in a helmet has a straight forward application in emergency scenarios and has been deployed as part of project "Comunicaciones Inalámbricas en Entornos de Seguridad y Emergencias" (CIES) funded by the Spanish Ministry of Economy and Competitiveness (RTC2015-4213-7).

The second design, a $6 \times 2 = 12$ planar array operating at 3.5 GHz, is the one to be used in Chapter 3 in order to empirically characterize the propagation channel model.

2.1 Introduction

In recent times, the demand for higher data transmission capacity in wireless systems due to the emergence of multimedia services (e.g., augmented reality, cloud computing, real-time video streaming) is exponentially growing. Current constraints regarding the

available spectrum and allowed power levels encourage the search for technological solutions like large–scale MIMO. In particular, large–scale MIMO aims to improve the spectral efficiency and consequently the system capacity via the deployment of multiple antennas on both communication ends, the base station and the user terminal while keeping the transmitted power constant. Nevertheless, the design of massive MIMO antenna solutions on the user end devices' has to face many challenges related to the reduced size, complexity and cost of the solution [8]. It must be noticed that these challenges are even more evident when the antenna is designed to cover frequency bands below 6 GHz now supported by broadband systems like LTE or LTE–A. In practice, MIMO antenna design efforts at the user end have to pay special attention to the isolation between individual radiating elements since it is vital to avoid mutual coupling effect. It usually appears as a result of sharing ground plane as well as the reduced inter–element distance among radiating elements. High level of mutual coupling can be considered as a destructive interference since a huge portion of the power fed into one port is coupled to the adjacent port instead of being radiated. Analyzing the consequences from the MIMO perspective, it can led to an increment of the correlation between the transmitted/received signals by each antenna, and this in turn reduces the number of independent parallel sub–channels that the MIMO system can reach, giving rise to a performance degradation in terms of capacity as it has been previously demostrated [9, 10].

In this Thesis, we will target the design of large–scale MIMO antenna solutions with reduced size, complexity and low cost to be deployed primarly at the user end. Specifically, the most challenging aspect is the reduced size that forces the antennas to get close, and therefore gives rise undesired effects such as mutual coupling and correlations.

Hitherto, many MIMO antenna designs presenting different decoupling methods have been proposed to overcome the limited space intended to the antenna emplacement inside mobile terminals. The design of a compact MIMO antenna for Ultra–Wideband (UWB) applications presented in [11] consists of two open L-shaped radiating elements placed perpendicularly to each other to achieve high isolation. Additionally, with the aim of reducing the mutual coupling, a narrow slot is added to the ground plane. In [12], the MIMO antenna consisting of two symmetric printed monopole antennas was developed to support five different frequencies (900, 1800, 2100, 3500 and 5400) MHz. The decoupling mechanism is integrated by two inverted-L branches and a rectangular

slot with one circular end etched on the ground plane. A ceramic based multiband MIMO antenna formed by two individual antennas covering several LTE bands is presented in [13]. Obviously, the novelty in this case comes from the ceramic material used for the antenna design. This material allows to reduce the antenna size improving in this way the utilization of the available space, and provides a very low correlation coefficient.

FIGURE 2.1: Textile multi–antenna deployed at user's garment. 8×5 MIMO textile antenna array deployed at the backside of a jacket (left side) and 4×4 textile antenna array deployed on a handbag (right side).

In this Thesis, as an alternative proposal to drastically overcome the limited space intended to the antenna emplacement inside mobile terminals, and consequently reducing the mutual coupling, we propose a MIMO antenna array design based on textile technology which will allow us to deploy personal area networks in the proximity of the human body. Specifically, as depicted in Fig. 2.1 our solution proposes to create wearable multi–antenna user terminals by means of disposing dozens of antennas on or as part of the user's garment or accessories (e.g., jacket, bags). Such an antenna solution would connect to any data-enabled user device, immediately improving its communication capabilities.

In the following sections, the fundamentals required to design the large textile antenna arrays, as well as the design and experimental characterization of two specific antennas will be explored.

2.2 Antennas fundamentals

2.2.1 Performance parameters

There are several parameters such as bandwidth, gain or radiation pattern which define antenna performance. Depending on the specific application for which an antenna is designed, each parameter plays different roles during the design process. In this subsection, most relevant parameters considered for the design of the wearable antennas developed in this Thesis are briefly introduced [14].

2.2.1.1 Radiation Pattern

It is a graphical representation or a mathematical function of the radiation properties of the antenna (e.g. directivity, electric field, radiation intensity or polarization) as a function of spatial coordinates. This representation is calculated in the farfield region and can be represented in two (2D) or three dimensions (3D) usually using polar coordinates. In a three dimensional representation of the radiation pattern there are two planes on which the points corresponding to the radiated energy of the antenna are plotted: azimuth and elevation. The first one depends on ϕ angle and can be seen as the horizontal plane with respect to the floor, while the second one is a function of the θ angle and can be idetify as the vertical plane with respect to the floor (see Fig. 2.2).

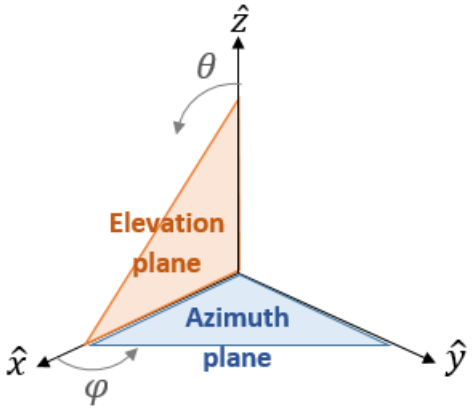

FIGURE 2.2: Azimuth and elevation planes.

Attending to the shape of its radiation pattern, an antenna can be classified into three different types (see Fig. 2.3):

- Isotropic: The antenna radiates the same power in all directions of the space.
- Omnidirectional: The antena presents a nondirectional pattern in a given plane (in azimuth) and a directional pattern in any orthogonal plane (in elevation).
- Directional: The antenna presents its maximum radiation in a particular direction.

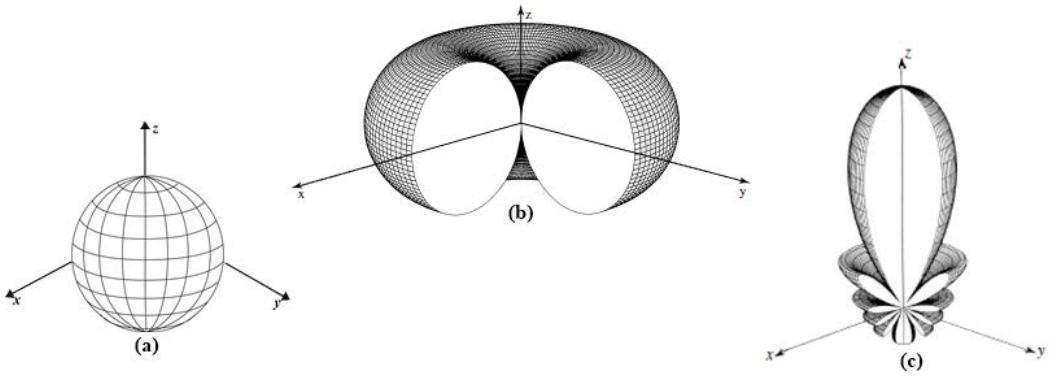

FIGURE 2.3: 3D view of (a) isotropic, (b) omnidirectional and (c) directional radiation (pencil beam) patterns [14].

2.2.1.2 S-Parameters

It is possible to evaluate the performance of an antenna by means of the S-parameters (scattering parameters). Specifically, when considering a multiport antenna (e.g. an array) these parameters provide information such as the reflected power, the transmitted power or the coupling between ports. Let us define S_{ii} as the reflection coefficient measured at the port i when the remaining ports are matched, while S_{ij} corresponds to the transmission coefficient between the port i and the port j when the remaining ports are matched. The first parameter enables to quantify the amount of energy which is reflected by the antenna. Theoretically, if power is totally reflected its value tends to be 0 dB. Conversely, if the power is totally absorbed and radiated by the antenna, the value will be $-\infty$ dB. Commonly, in antennas design a value equal to -10 dB is considered as reference (10% of the power is reflected). Regarding the second parameter, in this Thesis it allows to analyze the existing coupling between the radiating elements of an antenna array.

2.2.1.3 Bandwidth

It can be defined as the frequency range over which the operation of the antenna is satisfactory, that is, it can properly radiate or receive energy. Different criteria can be established taking into consideration the input impedance, the reflected power, the beamwidth or the side lobe levels among others to evaluate the adecuate antenna operation, being all of them equally valid. In this Thesis, the frequency range where the reflected power is less than 10% meaning that the reflection coefficient (S_{ii}) is below or equal -10 dB, is considered as the useful band. Then, the expression to compute bandwidth is given by:

$$BW = \frac{f_H - f_L}{f_o} \tag{2.1}$$

where f_H and f_L represents the upper and lower frequency values at which the reflected power by the antenna is still less than 10% and f_o is the center frequency also known as resonance frequency.

2.2.1.4 Input inpedance

The input impedance determines the ability of an antenna to accept power from a source. If the input impedance perfectly matches the output impedance of the source, then maximum power is transferred. It must be noticed that the radiating element will be matched to the transmission line and other associate equipment only within a bandwidth since the input impedance is a function of the working frequency.

2.2.1.5 Gain

It is defined as the ratio between the radiation intensity in one direction and the radiation intensity that would radiate an isotropic antenna, with equal distances and powers delivered to the antenna as defined in 2.2.

$$G = 4\pi \frac{U(\theta, \phi)}{P_{in}} \tag{2.2}$$

where $U(\theta, \phi)$ represents the radiation intensity in an specific angular direction and P_{in} is the total input accepted power. It must be noticed that if angular direction is not specified, gain is provided on the maximum radiation direction.

2.2.2 Patch antennas

Patch antennas, also known as microstrip antennas since their origin derives from this technology, were developed in the 1950s [15]. Nevertheless, first practical implementations [16] had to wait until 1970s when technological improvements in manufacturing methods, and the availability of new substrates with reduced loss tangents took place.

Regarding the patch antenna structure, in its simplest configuration it is formed by a ground plane, a dielectric substrate and a metallic patch of dimensions comparable to the wavelength as depicted in Fig. 2.4. Attending to the patch geometry, over the last decades patch antennas have been studied with great variety of geometries [17–19] (e.g. square, rectangular, circular, elliptical, ring-shaped or triangular) each of them providing specific properties in terms of bandwidth, radiation pattern, reflection coefficient, directivity, etc.

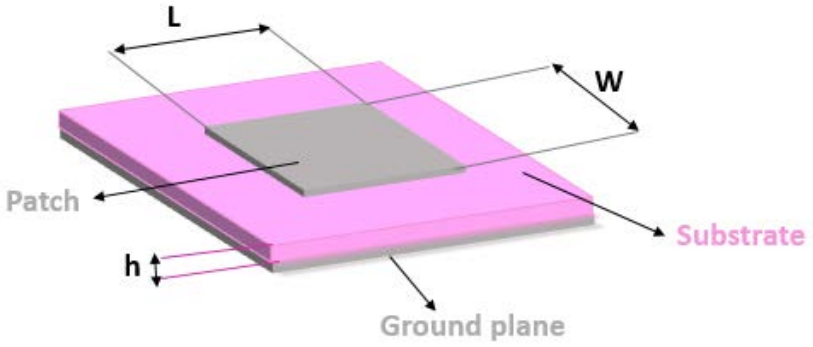

FIGURE 2.4: Square patch antenna scheme.

Other essential aspect to take into consideration for the proper antenna performance is the feeding technique. The four most popular feeding schemes can be classified into contacting and non-contacting categories depending on whether power directly feeds the radiating patch by means of a connecting element such as a coaxial probe or a microstrip line or if conversely power is transferred through electromagnetic coupling like in proximity and aperture coupling cases. A graphical description of the coaxial feed

method that we are applying in our designs is depicted in Fig. 2.5. In this feeding technique, the inner conductor of the coaxial connector extends from ground plane through the substrate and is soldered to the radiating patch, while the outer conductor extends from ground plane. Among the benefits of this type of feeding method are low spurious radiation, ease of manufacture and low cost [14].

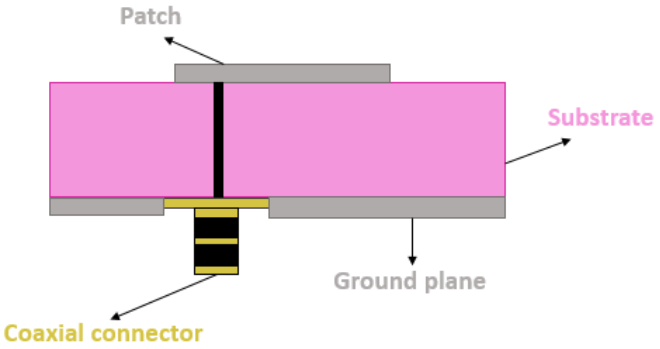

FIGURE 2.5: Patch antenna with coaxial feeding.

There are a number of potential advantages that patch antennas provide and that have had a great impact on their success in recent decades. Specifically, the miniaturization of the radiating element enables to design increasingly small scale and lighter devices making it the best choice for many mobile communication systems where the available space to locate the antenna is a critical factor [20, 21]. It is also important to highlight that these types of antennas are easy to make a conformal version since they adapt to all types of non-flat surfaces. They can be manufactured easily and inexpensively allowing large-scale production and they also offer easy integrability with microwave integrated circuits and into arrays [22].

2.2.2.1 Procedure to design rectangular patch antennas

Next, the detailed procedure to design a rectangular microstrip patch antenna is explained [14]. In order to design a patch antenna there are three essential parameters that must be known to ensure the required performance of the antenna: its desired resonance frequency, the dielectric constant of the substrate that is employed and its thickness.

The width of the patch (W, see also Fig. 2.4) will be determined by:

$$W = \frac{c}{2f_o}\sqrt{\frac{2}{\epsilon_r + 1}} \tag{2.3}$$

where c is the speed of ligth, f_o represents the resonance frequency and ϵ_r is the dielectric constant of the substrate.

Some of the electromagnetic waves propagating from the patch towards the ground plane go through the air, while the others go through the substrate (this is known as fringing effect). As the substrate and the air have different dielectric constants, it is necessary to define an additional variable, known as effective dielectric constant ϵ_{reff}, that takes into account this variation. Next, the effective dielectric constant will be calculated as

$$\epsilon_{\text{reff}} = \frac{\epsilon_r + 1}{2} + \frac{\epsilon_r - 1}{2}\left[1 + 12\frac{h}{W}\right]^{-\frac{1}{2}} \tag{2.4}$$

where h is the height of the substrate.

Additionally, due to the fringing effect the electrical dimensions of the patch tends to look greater than its physical dimensions. The characterization this length extension, ΔL, is given by

$$\frac{\Delta L}{h} = 0.412\frac{(\epsilon_{\text{reff}} + 0.3)(\frac{W}{h} + 0.264)}{(\epsilon_{\text{reff}} - 0.258)(\frac{W}{h} + 0.8)} \tag{2.5}$$

Finally, the patch will be totally determined by calculating its length (L, see also Fig. 2.4) as:

$$L = \frac{c}{2f_o}\sqrt{\epsilon_{\text{reff}}} - 2\Delta L \tag{2.6}$$

It must be noticed that for square microstrip patch antennas, widths are equal to lengths ($W = L$).

2.2.3 Antenna arrays

For future wireless systems single–element antennas are not enough to provide the expected requirements. As an alternative, we have previously mentioned that it is possible

to combine multiple element antennas to enhance the overall performance in terms of capacity of these systems.

Hence, once the basic radiating element has been studied, we will now focus on the array design. For this purpose, it is essential to briefly define what it is and how it works [14]. Traditionally, an array is defined as an antenna formed by a specific number of radiating elements, regularly ordered and fed to obtain a predefined radiation pattern. However, it must be noticed that in this Thesis we envision a MIMO application in which each element will work separately with the aim of transmitting independent flows of information (spatial multiplexing).

For arrays of identical radiating elements, there are some parameters that can modify the total field of the antenna. These are:

The physical geometry

Indicates the shape that the array takes and is defined by the position that each single element occupies in the space. Attending to its geometry three different types of arrays can be distinguished. An array is considered linear if the individual radiating elements that integrate it are arranged on a line. On the other hand, if the individual radiating elements are distributed on a plane the array is classified as planar. Finally, an array is considered shaped if its individual radiating elements are conformed on a curved surface. In Fig. 2.6 the two first geometries are represented.

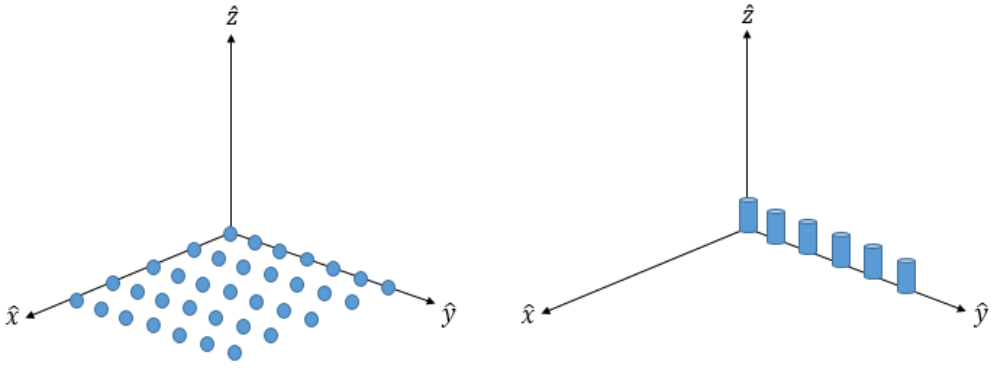

FIGURE 2.6: Example of two out of the three geometries: planar array (left side) and linear array (rigth side).

The spacing between elements:

It is defined as the distance between the centers of two contiguous elements in the array and can be considered as a key design parameter since varying it, the mutual coupling can be increased or decreased. It should be recalled that in MIMO systems antenna

arrays should be designed trying to reduce the mutual coupling since it may negatively interfere in the overall system performance. It has been proven that as the distance between elements increases the mutual coupling decreases [23]. Then, separating the elements as much as possible can be an option to reduce the mutual coupling.

The excitation of the individual elements (amplitude or phase)

It is possible to vary the directivity pattern of an antenna array through phase and amplitude control. Then, depending on the application it is possible to design array antennas where the elements are equally excited or not.

The radiation pattern of the individual elements

Its characteristics have a critical importance in the design, since they largely define the total antenna response.

2.3 Textile antennas

2.3.1 Basics

The emergence of textile antennas is determined by the search for technological solutions capable of adapting to the needs of the users of future communication systems. This type of antennas allows the development of lightweight, flexible communication systems of easy integration into the human body allowing free movements with minimal impact.

Regarding the most suitable antenna type for textile antennas development, patch antennas appears to be appropriate because of their radiation patterns that mainly radiate perpendicularly to the planar structure and the ground plane efficiently shields the biological tissues. Additionally, it should be noticed several advantages that can be offered such as low cost, lightweight, planar configuration and low volume. With regard to the narrow bandwidth they can offer, it is easily improved only incrementing the substrate height which has no impact in the textile antennas requirements.

In order to develop textile patch antennas such as those presented above, two types of materials are basically needed, one conductive for the patch and the ground plane, as well as a non-conductive which acts as a dielectric. It is important to remember that apart from being flexible and moldable to be integrated into the clothing, it is necessary to know the electromagnetic properties such as the permittivity and the loss tangent of these textile materials. In the literature there is a variety of materials that are briefly presented below.

Among the conductive materials also known as electrotextile materials, it can be distinguished those that are specifically designed for such an use: Shieldit [24], Flectron [24], Zelt [25], or Nora [26]. On the other hand, there are materials not specifically designed for being used as electrotextiles but that can meet the requirements. Among these are flexible polymers, copper, nickel-plated textile fabrics dipped in various metals such as copper or silver. Between the properties that this type of materials must offer it can be highlighted that the laminar resistance should not be very high in order to maintain the conduction losses at a minimum level, an adequate value will be less than $1\Omega/sq$, always being true for the frequency range in which the antenna should work.

Once the conductive material has been chosen, attention should be paid to the material that will act as a dielectric. A low and stable permittivity are some of the features that this material should possess in order to improve the radiant characteristics and ensure a constant behaviour in the working frequency band. In this case more conventional materials such as felt [27], fleece [24] or velcro [28] are used.

TABLE 2.1: Main features of conductive and non-conductive materials based on [29].

Conductive materials			*Non-conductive materials*		
Material	**Surface resistivity**	**Composition**	**Material**	**Loss tangent**	**Permittivity**
Shieldit	0.1	copper, nickel, polyethylene	Velcro	0.06	1.34
Flectron	0.07	nickel, copper, polyester nonwoven	Felt	0.023	1.38
Zelt	0.01	copper, tin, nylon	Fleece	0.0035	1.17
Nora	0.03	copper, nickel, nylon, silver			

To carry out the union of the materials that give rise to the patch antenna development, different processes have been used in the literature. The traditional sewing method or the use of adhesive sheets adhered by ironing are presented in [26] and other option would be the use of textile glue based on ammonia [30].

2.3.2 Brief literature overview

As it was mentioned before, textile antennas are designed with the aim of being part of garments, giving rise to a novel concept known as "smart clothing". This kind of antennas has emerged as a potential way to facilitate applications in different areas as explained below.

In [31] a dual polarized textile patch antenna operating at 2.4 GHz in the well-known Industrial, Scientific and Medical (ISM) band is designed with the aim of being integrated into protective garments. Regarding personal satellite communications, a dual-band (L-band and GPS) and circularly polarized textile patch antenna is presented in [32]. On the other hand, in [33] an all-textile antenna is proposed to be integrated into a military beret enabling in this way an indoor/outdoor positioning system. The antenna consists of a circular ring patch with four shorting vias operating at 915 MHz for indoor positioning systems, and a truncated patch designed for being used in outdoor propagation scenarios operating at 1.575 GHz for Global Positioning System (GPS) applications. Even for daily use, textile antenna designs have been proposed to be used in fashion or casual clothes, in [34] a dual-band textile Louis Vuitton logo (LV) antenna operating at 2.45 GHz and

4.25 GHz is proposed. Specifically, leather is chosen as non-conductive material as it is the common material used in the manufacture of handbags. In [35], as substrate commercially available blue jeans material is used to design a textile antenna operating at 5.2 GHz for wireless local area network (WLAN) and worldwide interoperability for microwave access (WiMAX) applications.

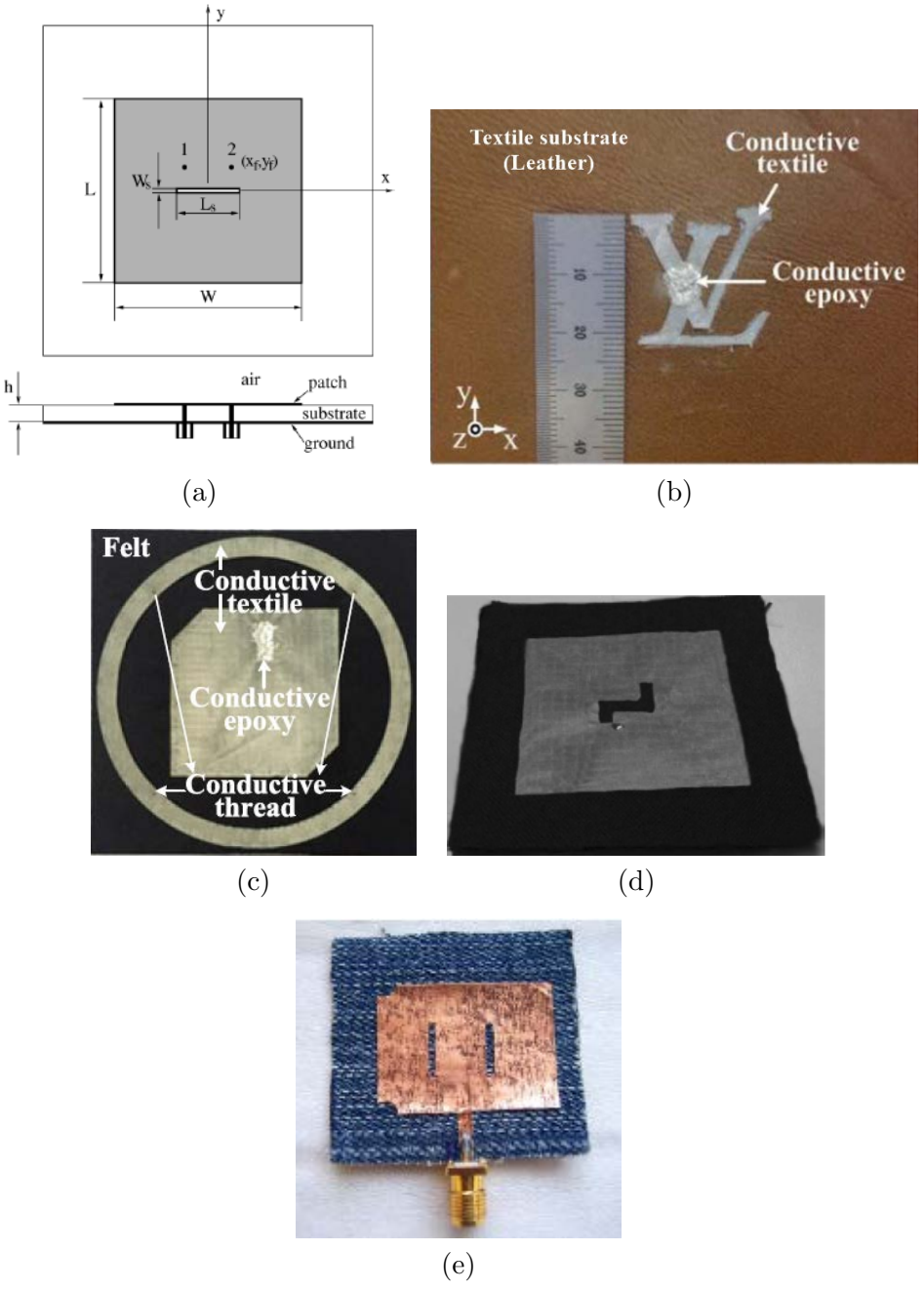

FIGURE 2.7: (a) Scheme of textile patch antenna designed to be integrated into protective garments [31] (b) Textile Louis Vuitton logo antenna extracted from [34] (c) Textile antenna integrated into a military beret extracted from [33] (d) Textile antenna for dual-band satellite use extracted from [32] (e) Textile antenna based on blue jeans fabric extracted from [35].

In view of the above, hitherto different designs of textile antennas for different applications have been proposed taking into consideration the wearable principles such as lightweight, miniaturization or flexibility. Next, we present the design of two antennas specifically designed in this Thesis to improve wireless communications with a focus on emergency scenarios.

2.4 Conformal MIMO array at 4.9 GHz

In this section, an antenna array based on textile technology is designed to be conformed on the cover of a safety helmet operating in the 4.9 GHz frequency band. This design is envisioned as a part of a LTE-based textile MIMO solution to enhance public safety communications (this issue will be deeply explored in Chapter 4).

2.4.1 Antenna design and simulation resuts

We select as optimal procedure of constructing the conformal antenna array, the design of a linear patch antenna array (see Fig. 2.9) that is later bent around an ellipsoidal surface which acts as a safety helmet, resulting in the desired conformed form. The planar geometry of the antenna is tailored to show a rectangular form once conformed. For that purpose, during the design stage, it was necessary to consider the effect of projecting a plane onto an ellipsoid as depicted in Fig. 2.8.

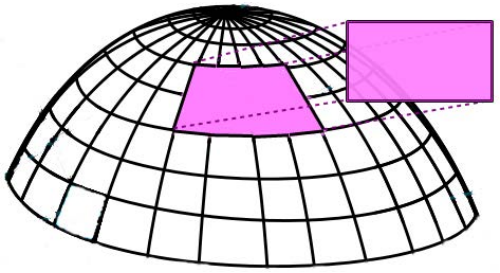

FIGURE 2.8: Projection of a plane onto an ellipsoidal surface.

The design of the conformal antenna with $M = 4$ radiating elements linearly deployed was performed using the commercial software, CST Microwave Studio. Common felt with thickness of 1 mm and permittivity equal to $\epsilon_r = 1.38$ was used as a dielectric and for its part, the metallization was developed with Flectron electro–textile material. For feeding, simple probe feeds with 50 Ω impedance are used. With regard to the safety helmet, we consider that its rigid outer section, known as shell, posses a standardized thickness of 3 mm and it is made of Acrylonitrile Butadiene Styrene (ABS), a kind of thermoplastic material whose dielectric constant is $\epsilon_r = 3$. The dimensions of the helmet are $225 \times 180 \times 130$ mm. Finally, the proposed antenna is assumed to operate in close proximity to human head which is modeled by Specific Anthropomorphic Mannequin (SAM) phantom. Specifically, it is composed by a shell filled with a liquid which allows to model the human head composition.

The fabric materials were sewn while the subminiature version A (SMA) connectors were soldered with tin.

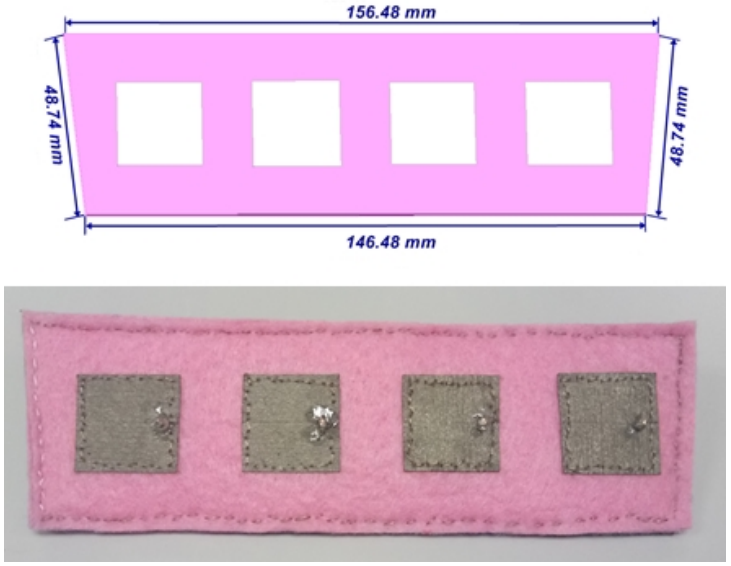

FIGURE 2.9: Schematic with optimized dimensions and real planar prototype of the proposed antenna.

The initial design parameters of the antenna (distance among elements, location of the feeding probes, thickness of the material used as substrate and patches sizes) are optimized in order to achieve low mutual coupling (MC), minimum reflection coefficient at the desired operating frequency and appropriate bandwidth. During the optimization procedure it has been necessary to counter a shift of the resonance frequency that was produced probably due to the the presence of a lossy medium like the biological tissue and the bend effect. In addition, considering this design as an intial proof–of–concept we also decided to analyze the behavior of the conformal antenna not only when it is conformed inside the helmet, but also when it is outside. The first option would possibly be the most appropiate from an industrialization point of view since the helmet may act as radome. In this case, the helmet does not have to be drilled or modified, preserving its protecting properties. Table 2.2 shows the dimensions of the array geometry after optimization by means of CST design and simulation.

The simulated results for the optimized design dimensions are provided in terms of the antenna radiation patterns and the S–parameters. The radiation patterns of each radiating element slightly vary, giving rise to antenna gains going from 7.81 to 8.47 dB depending on its relative position. Negligible backward power levels below -20 dB are also achieved. In Fig. 2.10 an example of the radiation pattern of one of the

TABLE 2.2: Optimized dimensions of the conformal antenna.

Parameter	Value (mm)
Inter–element distance	$35.77 \approx 0.6\lambda$
Substrate height (h)	3
Width of central patches ($W = L$)	22.17
Width of extreme patches ($W = L$)	22.4
Total array perimeter	400.44

radiating elements is given. On the other hand, information regarding S–parameters can be extracted from Fig. 2.11. Specifically, the simulated reflection coefficients with values around −18.8 dB and −23 dB (depending on the conformal antenna position) state that each radiating element is well matched at the operating frequency. Low MC (S_{21} and S_{23} parameters) of about −19 dB can be observed among adjacent antennas. Simulated bandwidths of 270 MHz and 310 MHz (outside and inside) are accomplished.

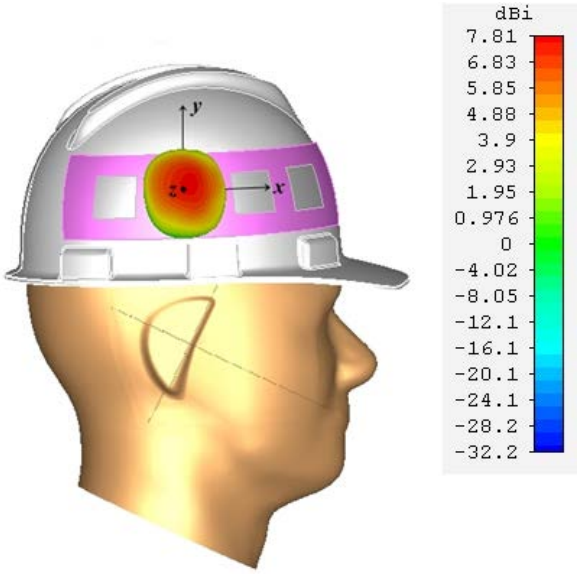

FIGURE 2.10: Conformal antenna deployment over a safety helmet and radiation pattern in 3D view for element placed approximately in the middle of the linear array.

2.4.2 Experimental results

To experimentally verify the proposed design, an antenna prototype manufactured by hand was developed as shown in Fig. 2.12. In this prototype the fabric materials were sewn while the SMA connectors were soldered with tin. It should be noticed that the dimensions of the design are equal to those previously described. The measurements

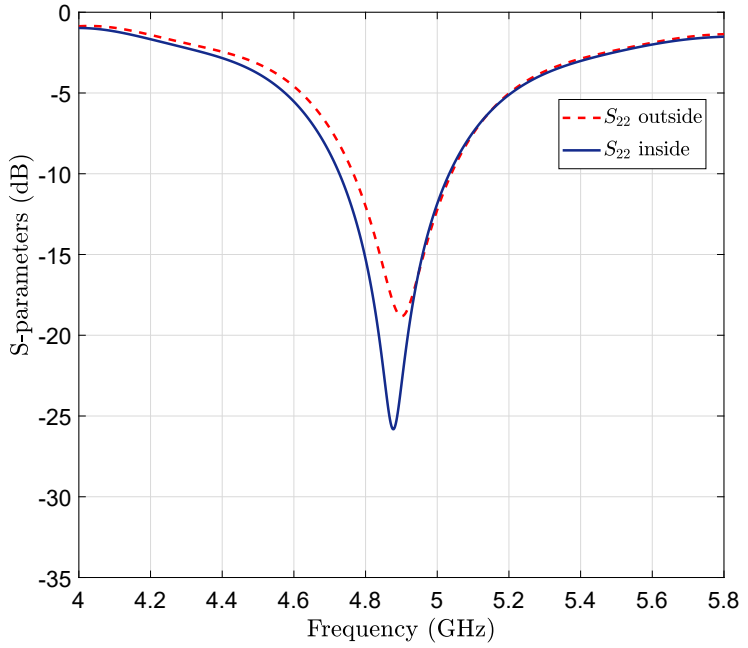

(a) Return losses (S_{22}).

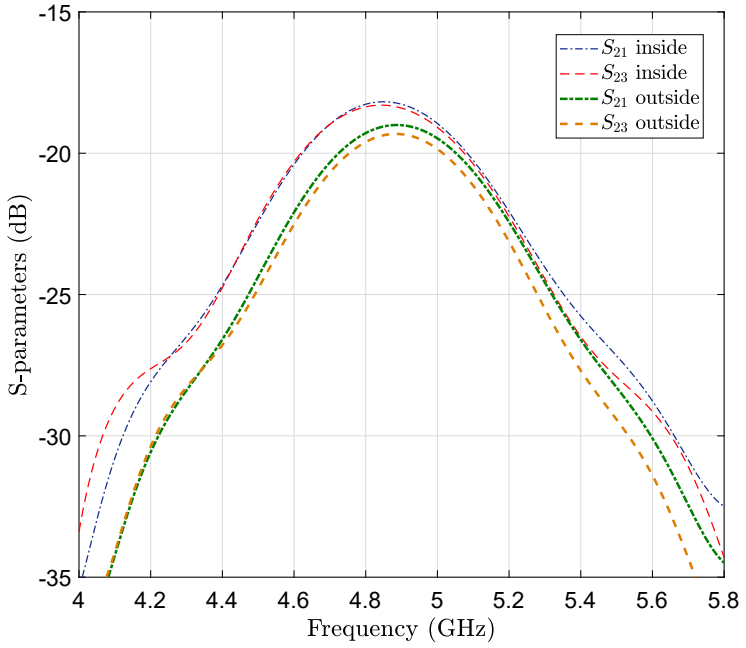

(b) Mutual coupling (S_{21} and S_{23}) with the two nearest antennas surrounding left and right, respectively.

FIGURE 2.11: Simulated performance of the textile antenna conformed inside and outside the helmet.

were performed with a vector network analyzer (VNA) in a frequency band between 3.8 GHz and 6 GHz.

FIGURE 2.12: Experimental prototype of the conformal antenna inside a safety helmet.

Fig. 2.13 presents the measured S–parameters. A reasonable agreement between simulations (see Fig. 2.11) and measurements is observed. A reflection coefficient of -16 dB is measured at the center frequency of the antenna, this implies that elements are still well matched. For its part, the measured bandwidth extends around 420 MHz. In relation to the MC, values below -17.5 dB have been registered.

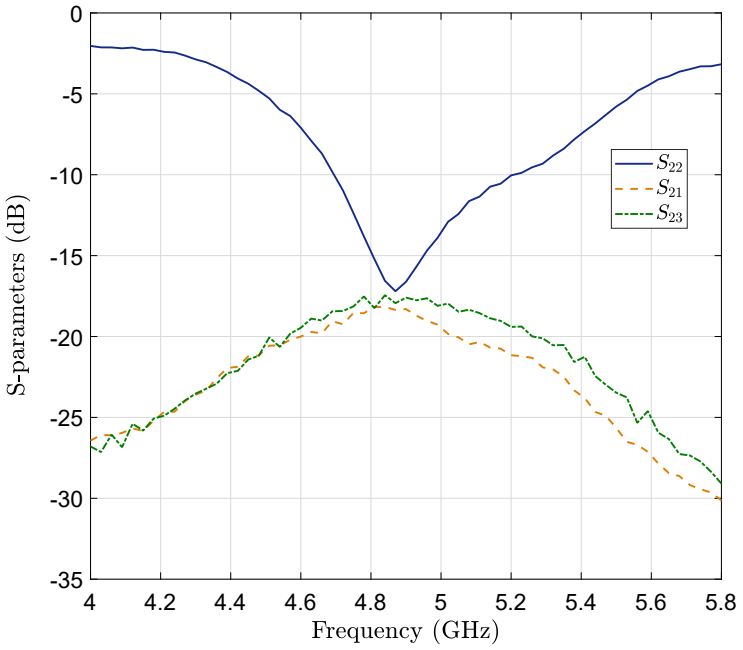

FIGURE 2.13: Measured reflection coefficient of the second antenna (S_{22}) and mutual coupling with the two antennas surrounding left and rigth (S_{21},S_{23}).

It should be clarified that small disagreements between simulations and measurements might be mainly caused by manufacturing inaccuracies as well as by assigning ideal

values to some features of the substrate such as the loss tangent during the simulation process. For example, the measured reflection coefficient in Fig. 2.13 has larger losses than the simulated in Fig. 2.11(a). If that is the case, the measured parameter shifts down compared to the simulated, and consequently bandwidth increases with the drawback of enlarging the losses.

2.4.3 Specific absorption rate analysis

The deployment of a large number of antennas around the user's personal sphere may usually generate hesitations owing to the possible effects on the human body. Hence, evaluating the energy which is absorbed by a biological tissue mass when it is exposed to a radio frequency electromagnetic field seems desirable during the design of a wearable antenna. Concretetly, the Specific Absorption rate (SAR) metric defined in (2.7) allows to quantify that effect by averaging over a specific sample volume of biological tissue (1 g or 10 g) or over the whole body.

$$\mathrm{SAR} = \frac{\sigma E^2}{2\eta} \qquad (\mathrm{W/Kg}) \tag{2.7}$$

where σ is the tissue conductivity, E^2 represents the electric field strength and η is the tissue density.

Based on the foregoing, an analysis of the electromagnetic energy absorbed by the human head when is located next to the ground plane of the proposed conformal antenna operating at 4.9 GHz is shown as follows. The SAR is computed in CST MWS using SAM phantom head model and the IEEE C95.3 [36] averaging method. As reference input power, we consider two different values, -40 dBm and 23 dBm, corresponding to the minimum and maximum transmitted power values for a LTE user terminal. Finally, as baseline for comparison in our analysis we considered as safer limits for a partial body part the ones established in the European Union by the European International Electrotechnical Commission (IEC) below 2 W/Kg for 10 g of tissue, and also those defined in United States by the Federal Communications Commission (FCC), that is, 1.6 W/Kg for 1 g of biological tissue volume.

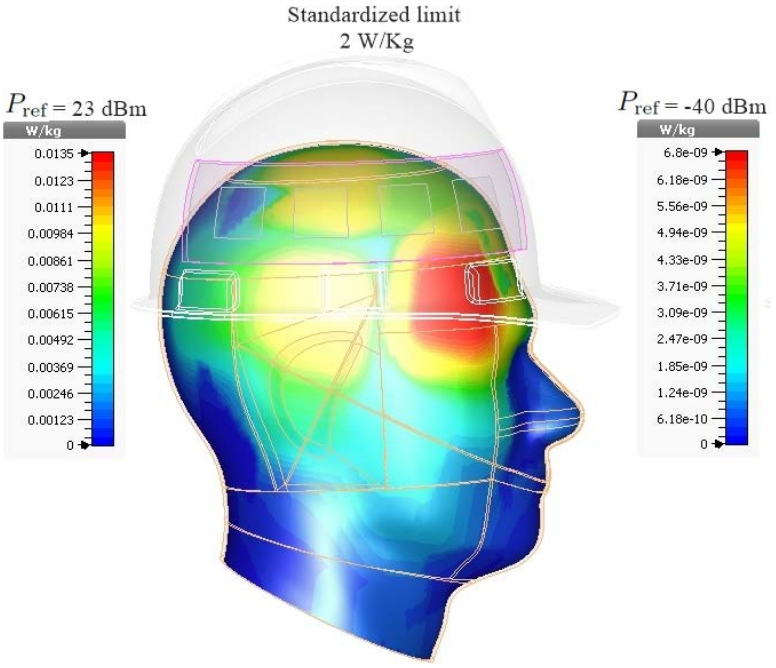

(a) Averaged over 10 g outside the helmet.

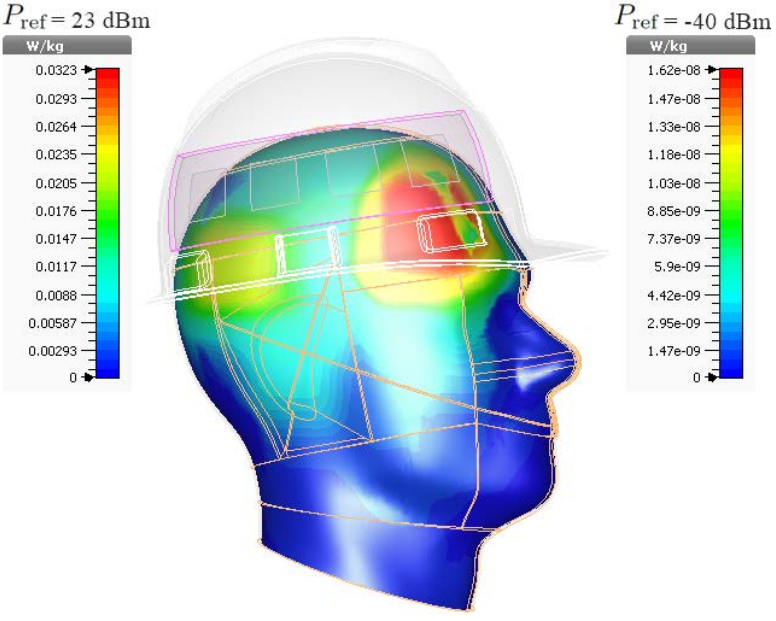

(b) Averaged over 10 g inside the helmet.

FIGURE 2.14: SAR distribution averaged over 10 g of tissue for different reference power values $P_{\text{ref}}(\text{dBm}) = \{-40, 23\}$ corresponding to the minimum and maximum transmitted power by a user terminal in LTE. Results are presented when the antenna is conformed outside and inside the helmet.

Fig. 2.14 and Fig. 2.15 show the SAR distribution when the proposed antenna is conformed outside and inside a safety helmet situated in a human head for the two reference input power values and averaging over different tissue volumes (1 g and 10 g). Unsurprisingly, higher SAR values are registered when the antenna is conformed inside

the helmet due to the close proximity with the biological tissue. In spite of this, simulation results show acceptable SAR values satisfying the aforementioned international standards. Lastly, it is worth noting that the proposed conformal antenna produces SAR levels in the same range as other antenna designs whose performance has been also evaluated in practical helmet models [37].

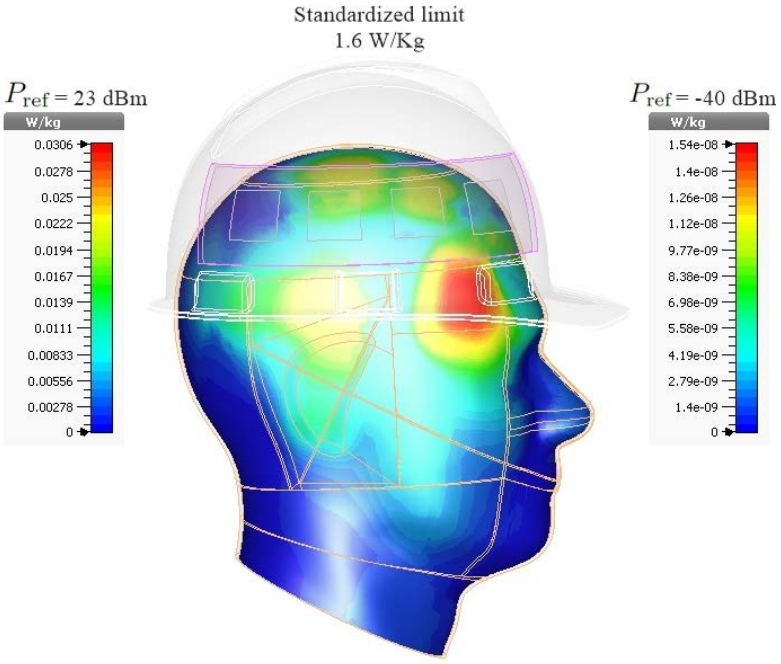

(a) Averaged over 1 g outside the helmet.

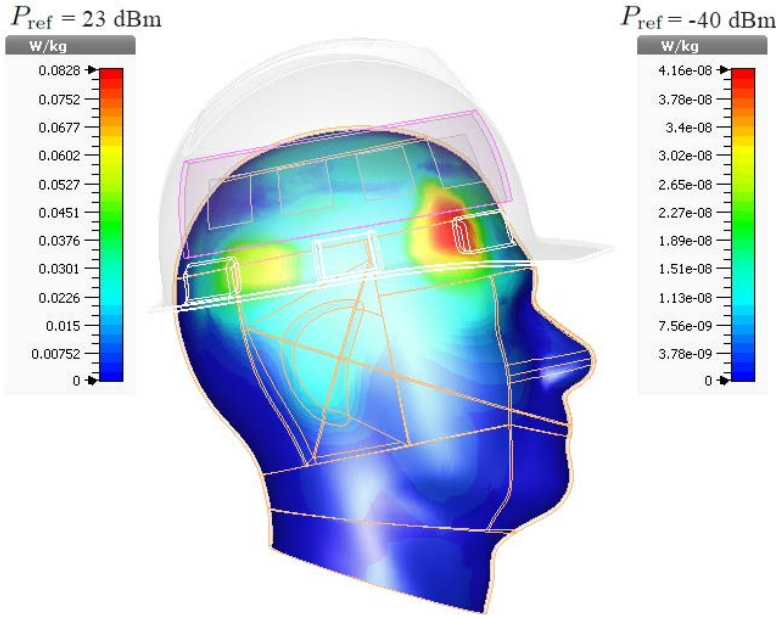

(b) Averaged over 1 g inside the helmet.

FIGURE 2.15: SAR distribution averaged over 1 g of tissue for different reference power values $P_{\text{ref}}(\text{dBm}) = \{-40, 23\}$ corresponding to the minimum and maximum transmitted power by a user terminal in LTE. Results are presented when the antenna is conformed outside and inside the helmet.

2.5 Textile MIMO array at 3.5 GHz

As an alternative to the previous design proposed to be integrated in a helmet, in this section we focus on the design of a planar array also based on textile technology, operating at 3.5 GHz that will be deployed in the back of the user's jacket. Since the available space in this case is higher, a larger number of antennas migth be integrated at the user end. As in the previous case, this textile antenna is also envisioned as a part of a technological proposal to enhance future public safety communications (see Chapter 5).

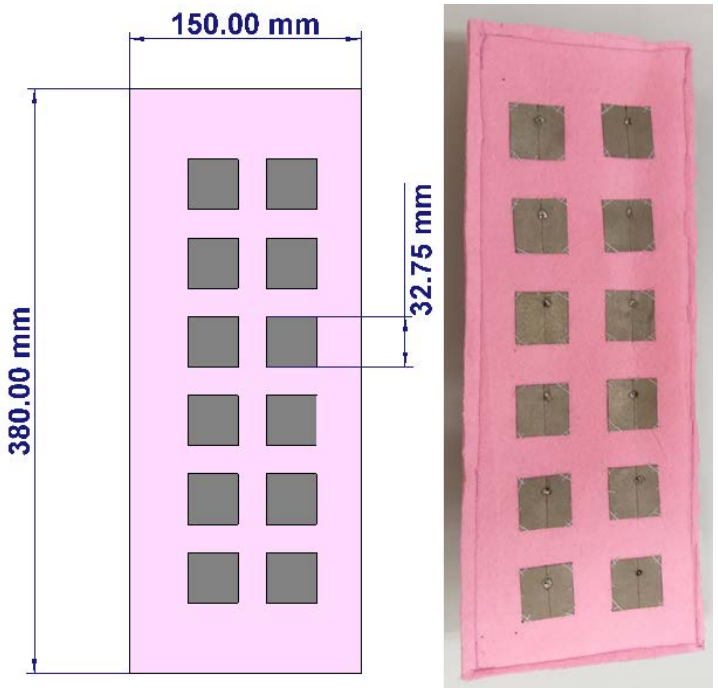

FIGURE 2.16: Schematic with optimized dimensions and real prototype of the proposed 6×2 planar array with textile antennas.

2.5.1 Antenna design and simulation results

The schematic and real prototype of the proposed textile planar array that consists of $M = 12$ radiating elements in a 6×2 rectangular configuration are illustrated in Fig. 2.16. The textile substrate used is commercial felt (with dielectric contant, $\epsilon_r = 1.38$). For all the conductive parts Flectron fabric material is chosen. To performe the union of the different materials the traditional sewing method was applied. The individual patches are fed by standard coaxials of 50 Ω that were soldered with tin. Once again, it is important to consider the interaction between the textile antenna and the human

body during the design phase since the biological tissue (in this case a human back) is a lossy medium that may vary the optimal design parameters, as well as to study the effects of the human body exposure to electromagnetic fields. For both purposes, the electromagnetic voxel model of the human body known as HUGO from the Visible Human Project® [38] is employed.

Firstly, the dimensions of the antenna to operate at the resonance frequency of 3.5 GHz were obtained using the expresions presented in subsection 2.2.2. Afterwards, the dimensions were optimized using CST Microwave Studio software and are summarized in Table 2.3. Considering the total perimeter of the textile array, it is worth noting that at 3.5 GHz it would be possible to deploy up to 54 radianting elements in a 9×5 rectangular geometry on the back of an adult due to the available space. Nevertheless, in our experimental design the number of radiating elements is restricted to $M = 12$ due to the capacity of the measurement setup that will be presented in Chapter 3.

TABLE 2.3: Optimized dimensions of the 6×2 planar array.

Parameter	**Value (mm)**
Inter–element distance	$51.1 \approx 0.6\lambda$
Substrate height (h)	3
Width of patches ($W = L$)	32.75
Total array perimeter	1060

With the optimized dimensions obtained, we can simulate the performance of the textile array. Fig. 2.17(a) shows the return loss and mutual coupling parameters as function of the frequency for one element situated in the center of the array. In view of the results, we can notice that the antenna is matched at the resonant frequency since $S_{ii} < -10$ dB, exhibits a bandwidth of 120 MHz and the coupling between adjacent elements ($S_{ij}, i \neq j$) is low, taking values below -18.8 dB. Regarding the radiation patterns, there are moderate differences between each of the individual elements that result in antenna gains varying from 7.58 to 8.1 dB depending on its location within the planar array and almost null back radiation levels below -19 dB are also achieved. Fig. 2.17(b) illustrates the radiation pattern of one of the elements placed approximately in the middle of the textile array.

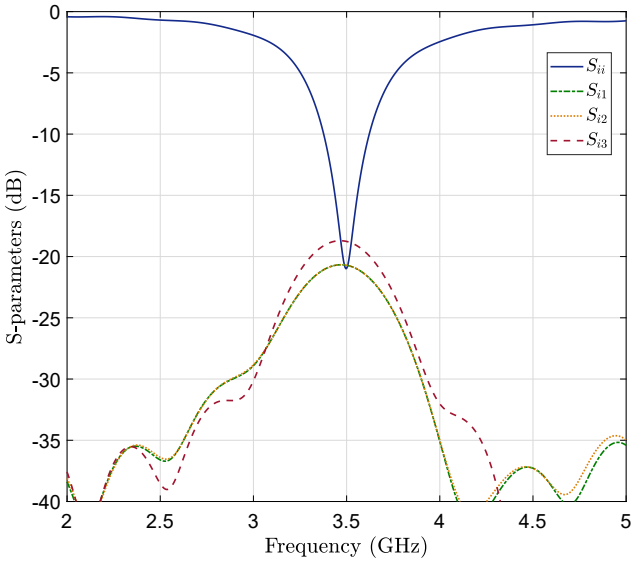

(a) Simulated return loss (S_{ii}) and mutual coupling (S_{ij}) with the three antennas surrounding left, up and down for element placed approximately in the middle of the 6×2 planar array.

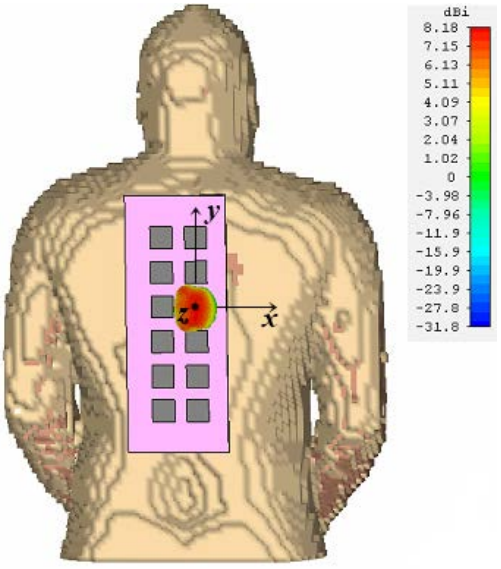

(b) Radiation pattern (3D view) for element placed approximately in the middle of the 6×2 planar array.

FIGURE 2.17: Simulated results of the 6×2 textile antenna array.

2.5.2 Experimental results

In order to validate the antenna properties, experimental measurements were carried out using a VNA. The dimensions of the prototype are the same obtained in the design procedure undertaken with CST. Once again, comparing Figs. 2.18 and 2.17(a) althougth

minor discrepancies between measurements and simulations that can be due to tolerances in manufacturing process exist, we can ensure that there is a good similarity and all results properly cover the operating frequency 3.5 GHz. Specifically, the measured reflection coefficient (S_{ii}) is equal to -17.5 dB, the measured MC ($S_{ij}, i \neq j$) is below -19.5 dB and the measured bandwidth is better than expected with a value around 360 MHz.

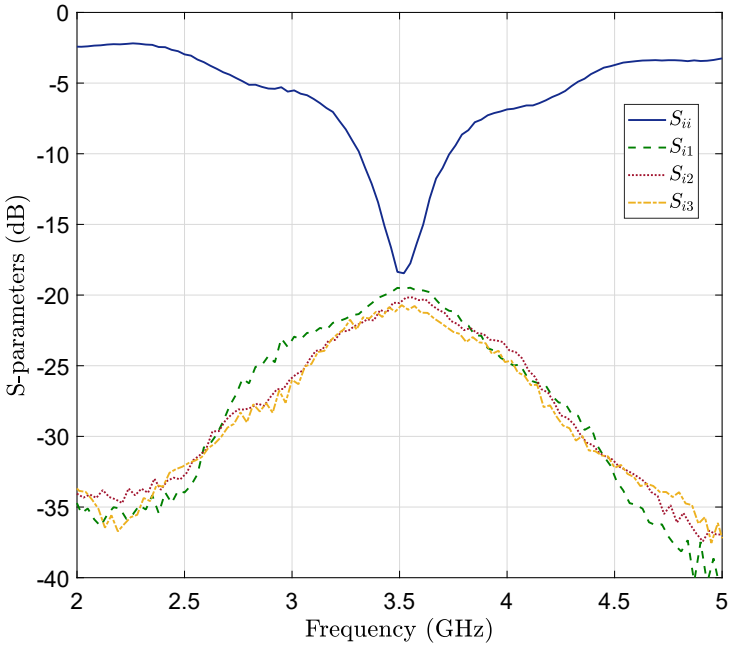

FIGURE 2.18: Measured return loss (S_{ii}) and mutual coupling (S_{ij}) with the three antennas surrounding left, up and down for element placed approximately in the middle of the 6×2 planar array.

2.5.3 Specific absorption rate analysis

SAR simulations were performed using the aformetioned human body model in CST Microwave Studio. It should be noted that to optimize the simulation time the voxel model was truncated, evaluating in this way only the upper part of the body.

TABLE 2.4: Simulated peak SAR values of the 6×2 planar array.

	Input power (dBm)	
	-40	**23**
SAR_{1g} (W/Kg)	$4.43e^{-9}$	0.008
SAR_{10g} (W/Kg)	$2.33e^{-9}$	0.005

Results shown in Fig. 3.17 proved that the textile antenna array is suitable for body-worn communications close to the human body since the peak SAR values summarized in Table 2.4 are below the standardized limits. In addition, these SAR levels perform similarly compared to those presented by other wearable antenna designs [39].

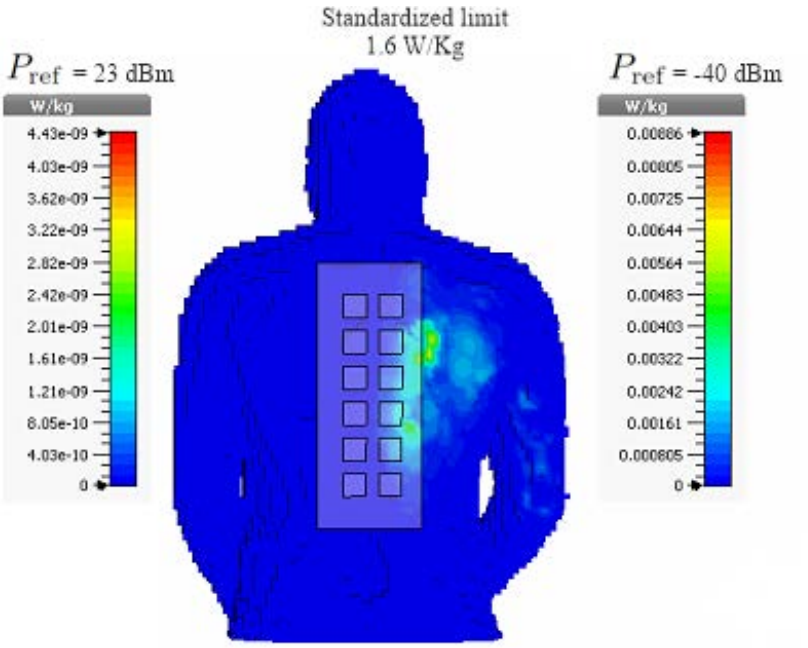

(a) Averaged over 1 g

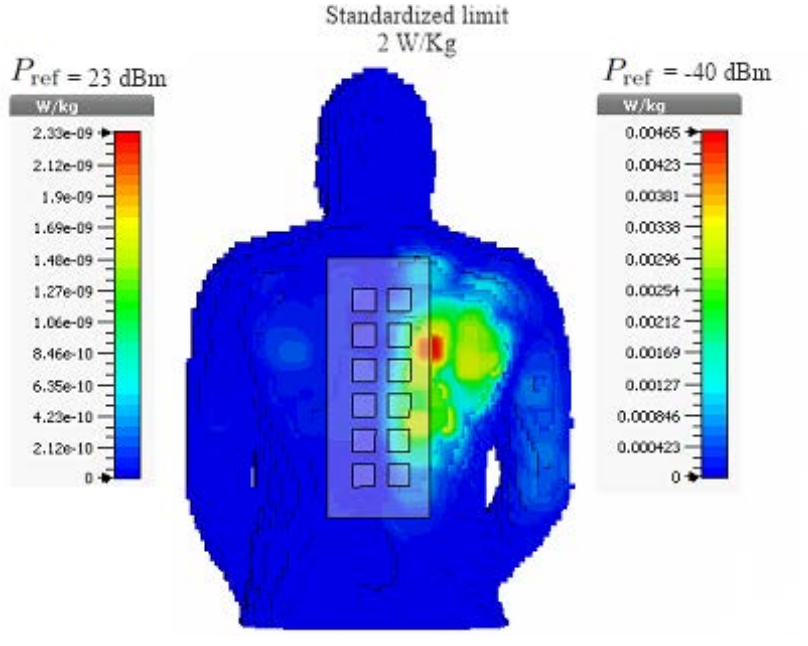

(b) Averaged over 10 g

FIGURE 2.19: SAR distribution averaged over 1 g and 10 g of tissue for different reference accepted power values $P_{\text{ref}}(\text{dBm}) = \{-40, 23\}$ corresponding to the minimum and maximum transmitted power by a user terminal in LTE. Results are presented when the antenna is situated in the back of a person.

2.6 Conclusions

In this chapter, a MIMO wearable antenna hub concept has been explored from the antenna design and performance point of view. To this end, the basics and criteria needed to face the design of this solution have been presented. Next, we performed the design, fabrication and experimental characterization of two MIMO body-worn antennas. The first design presents a linear array operating at 4.9 GHz with 4 antennas which is conceived to be conformed over a safety helmet while the second one presents a 6×2 planar array operating at 3.5 GHz conceived to be integrated in the back side of a jacket. In both cases, simulation and experimental results illustrate the viability of the proposed designs since suitable gains and reduced back radiation levels, proper bandwidths, low mutual couplings and SAR values below the standardized requirements were achieved. Finally, it is important to stand out that the multi–antenna solution is versatile since it can be easily suited for any specific application by simply adapting its resonant frequency and bandwith depending on the requirements. Nevertheless, in this Thesis we focus on analyzing the feasibility of the textile array as a part of a technological proposal whose main objective consists of improving future public safety communications (see Chapter 4).

Chapter 3

Experimental Characterization of a Textile Multi-antenna Terminal

This chapter explores the empirical characterization of a propagation environment where at one of the communication ends a textile multi-antenna terminal is deployed. The objective is to demonstrate the real benefits of seamless integrating a large number of antennas directly at the user end. Among the main contributions of this chapter are:

(i) The implementation of a measurement campaign at 3.5 GHz in several O2I underground propagation scenarios.

(ii) The statistical characterization of large–scale fading accounting for path–loss and shadow fading and affecting the received Signal–to–Noise ratio (SNR).

(iii) The statistical characterization of fading in these scenarios, particularly the narrow–band MIMO channel matrix comprising small–scale fading and spatial correlation, key for MIMO achievable rate evaluation.

(iv) The evaluation and comparison of the system achievable rates based on measured data with the synthetic rates generated using our fitted statistical models.

(v) Quantify how different factors such as spatial correlation or the normalization of the channel realizations, among others can impact the performance of the MIMO system.

3.1 Introduction

As in any branch of science, experimental measurements are key to develop mathematical models which faithfully simulate the real magnitude that is being represented. In the specific case of propagation measurements, these help to characterize in depth the features of wireless propagation channels. The main characteristic that is usually measured in these cases is the impulsive response between the transmitter and the receiver. Through this response it is possible to obtain secondary parameters of great utility that allow to characterize the performance of the system, for instance, in terms of capacity.

Given the above considerations, it is clear that limited or unmatched propagation information makes predicting performance on relevant scenarios a real challenge. Thus, a complete characterization of the performance of a textile MIMO-based solution in these scenarios is of high relevance. Many efforts have been devoted to characterize MIMO Indoor-to-Indoor (I2I) and Outdoor-to-Outdoor (O2O) scenarios [40–43]. Nevertheless, from the communications perspective, the characterization of O2I underground propagation environments such as basements, garages or tunnels is highly relevant since they are typical locations with low coverage where MIMO gains could make a difference. Concretely, these locations are highly dependent on the physical structure and materials of the buildings, as well as on the outside environment. In the literature, some authors have characterized other O2I propagation environments and evaluated their impact on MIMO system performance [44–46].

In contrast to these studies, the work developed in this Thesis is mainly focused on characterizing, to the best of our knowledge, unexplored indoor locations where the UE is a few meters below the ground level, modeling in this way realistic O2I environments where communications cannot be always guaranteed[1]. Additionally, we propose to integrate a portable, lightweight textile antenna array in the UE enabling the deployment of multiple antennas directly at the user end (e.g., accessories, clothing). Finally, empirically data rate performance characterization in these challenging O2I garage–type propagation scenarios where the base station (BS) is located outdoors at ground level and the UE is placed underground, is performed.

[1]It will be further explored in Chapter 4 that O2I underground environments may be the case of typical emergency scenarios that first responders have to face and where it is not possible to offer an always on connectivity with reliable high data rate.

3.2 Theoretical foundations

3.2.1 Wireless channel

The channel is defined as the physical medium that exists between the transmitter and the receiver by which signals are propagated and eventually corrupted with distortions. In the specific case of wireless channels, any electromagnetic signal that propagates through them will reach the destination by means of different paths commonly known as multipath. In a MIMO system, the channel impulse response defined between one specific antenna, j^{th}, at the transmitter ($j = 1, 2, ..., M$) and one specific antenna, i^{th}, at the receiver ($i = 1, 2, ..., N$) can be modeled by a discret number of impulses as addressed below [47]:

$$h_{ij}(\tau, t) = \sum_{d=1}^{D} a_d(t)\,\delta(\tau - \tau_d) \tag{3.1}$$

where D represents the number of different paths that reach the receiver, $a_d(t)$ is the path attenuation and τ_d defines the delay of each path. Then, from this definition the composed MIMO channel impulse response is given by the $N \times M$ matrix $\mathbf{H}(\tau, t)$ with

$$\mathbf{H}(\tau, t) = \begin{bmatrix} h_{11}(\tau, t) & h_{12}(\tau, t) & \cdots & h_{1M}(\tau, t) \\ h_{21}(\tau, t) & h_{22}(\tau, t) & \cdots & h_{21}(\tau, t) \\ \vdots & \vdots & \ddots & \vdots \\ h_{N1}(\tau, t) & h_{N2}(\tau, t) & \cdots & h_{NM}(\tau, t) \end{bmatrix} \tag{3.2}$$

For its part, the origin of the different paths arises from divers physical mechanisms that take place during the signal propagation. Next, the more relevant mechanisms are illustrated in Fig. 3.1 as well as briefly defined:

- Reflection: a portion of the incident energy is reflected when the signal strikes an object of large dimesions such as a building (considering as large dimensions those greater than the wavelength).
- Diffraction: takes place when the electromagnetic wave propagates close to sharp edges such as building corners. This phenomenon allows the wave to surround the

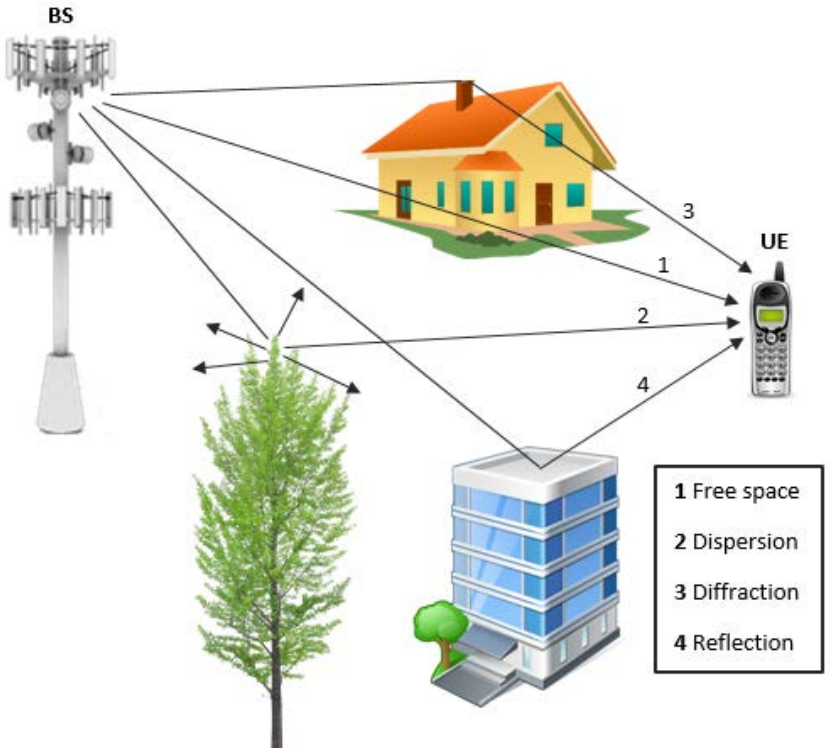

FIGURE 3.1: Example of multipath propagation environment.

obstacle by changing its trajectory, reaching the receiver even under non-line-of-sight (NLOS) conditions.

- Dispersion: occurs when an electromagnetic wave impinges on small size obstacles (again with respect to the wavelength) like branches of trees or irregular grounds. As a result the energy of the signal is dispersed into different directions of the space.

- Free space: propagation environment through wich an electromagnetic wave propagates without obstacles from the transmitter to the receiver and that presents electrical features identincal to those presented by the vacuum (ϵ_o, μ_o).

From the received signal point of view, any of the aforementioned effects end up being translated into fades, whose estimation is considered as one of the main challenges in communications. Considering them, a widely extended classification distinguishes between small–scale fading models that explain the behavior of the received signal power for short distances (comparable to the wavelength) and, on the other hand, large–scale fading models which explain the behavior of the received signal power for large distances (few hundreds of wavelengths). Fig. 3.2 shows an example of both of them.

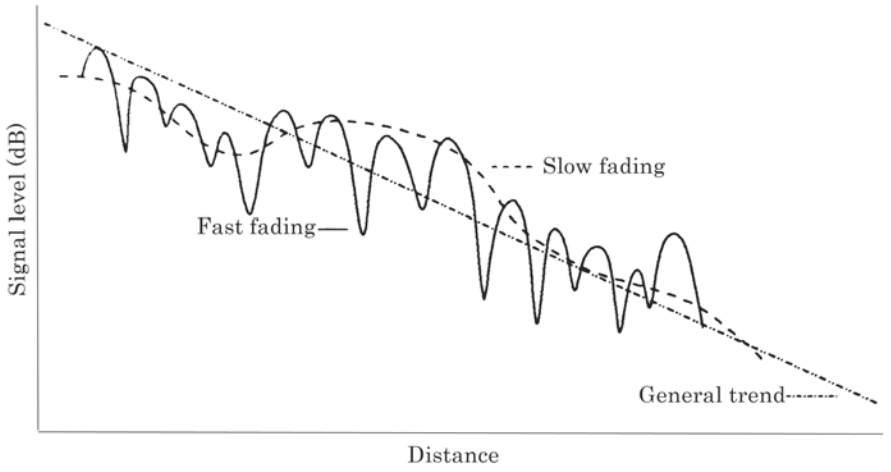

FIGURE 3.2: Signal power fluctuation as function of the distance [48].

3.2.2 Large–scale fading models

Large–scale fading corresponds to slow fluctuations of the received signal strength. There are two main components that characterize this type of fading. The first one refers to the propagation losses (path–loss) that are directly related to the distance between the transmitter and the receiver, as well as to the propagation environment (rural areas, urban areas, etc.). While the second component known as shadowing represents the fluctuations of the received signal strength with regard to the average and that usually occur due to obstructions.

Mathematically, it is possible to define the expression of the average received signal strength at a certain distance (d), including not only the path–loss effect, but also the shadowing, as shown below [49]:

$$P_R\,(d)\,[dBm] = \overline{P_R}\,(d_o) - 10\alpha \log_{10}\left(\frac{d}{d_o}\right) - X_s \tag{3.3}$$

where d represents the distance between the transmitter and the receiver, d_o is the reference distance, $\overline{P_R}\,(d_o)$ is the average received power strength at the reference distance, α refers to the path–loss exponent and X_s is the shadowing, characterized by zero–mean Gaussian random variable with standard deviation σ_{x_s} (both in decibels).

The $\overline{P_R}\,(d_o)$ value is usually obtained by means of propagation measures, although it can also be estimated as the received signal strength at the reference distance in free

space conditions (there are not obstructions in the path defined between the transmitter and the receiver). Attending to this last case, the value is calculated by means of the well known Friis equation [49] as follows:

$$\overline{P_R}\,(d_0)\,[dBm] = P_T + G_T + G_R + 20\log_{10}\left(\frac{\lambda}{4\pi d_o}\right) \tag{3.4}$$

where P_T is the transmitted power, G_T and G_R represent the transmitter and receiver antenna gains, λ is the wavelength and d_o is the aforementioned reference distance.

Regarding α, it can be considered as one of the most relevant parameters of the model defined in (3.3). It indicates the attenuation rate of the average received signal strength as a function of distance. Its value depends on the specific propagation environment and, therefore, there are many research works that have focused on its characterization [50–52]. Although there are several methods that can be applied to estimate this parameter, the linear regression analysis is one of the most frequently used, typically following the criterion of minimizing the mean square error (MSE) between the measured average received signal strength values and the values of the estimated regression line. Table 3.1 summarizes the most common values according to different propagation environments:

TABLE 3.1: Path–loss exponents for several propagation environments, adapted from [49].

Propagation environment	**Path-loss exponent (α)**
Free space	2
Urban area	2.7 - 3.5
Shadowed urban area	3 - 5
Buildings with line-of-sight (LOS) conditions	1.6 - 1.8
Obstructed factories	2 - 3
Obstructed buildings	4-6

On the other hand, paying attention to the random variable X_s, it has been observed through different experimental studies that it follows a normal distribution when is expressed in logarithmic units (e.g. in decibels) and is commonly known as log–normal distribution. It is defined by the following probability density function (PDF) [49]:

$$f_{X_s}\,(x_s) = \frac{1}{\sqrt{2\pi\sigma_{x_s}^2}}\exp\left(-\frac{x_s^2}{2\sigma_{x_s}^2}\right) \tag{3.5}$$

where $\sigma_{x_s}^2$ represents the variance of the long–term signal power fluctuation in dB.

Finally, it is worth noting that it would be possible to express (3.3) depending on the average path–loss of the link at a certain distance (d) instead of depending on the average received signal strength, as shown below:

$$P_L\left(d\right)\left[dB\right] = \overline{P_L}\left(d_o\right) + 10\alpha\log_{10}\left(\frac{d}{d_o}\right) + X_s \tag{3.6}$$

where $\overline{P_L}\left(d_o\right)$ represents the average path–loss at a certain reference distance (d_o) in free space conditions and is calculated as follows:

$$\overline{P_L}\left(d_o\right)\left[dB\right] = 20\log_{10}\left(\frac{4\pi d_o}{\lambda}\right) \tag{3.7}$$

3.2.3 Small–scale fading models

Small-scale fading corresponds to the rapid fluctuations of the received signal strength over small distance ranges (local area) and short periods of time. There are two statistical distributions widely used to describe the variations of the envelope of the received signal due to multipath effect in local areas [48].

Assuming that the fading is caused by the superposition of a large numer of independent multipath components and that none of them is dominant over the others, then it can be considered that the amplitude of the different components are in the same order of magnitude, and therefore the envelope of the received signal follows a Rayleigh distribution whose propability distribution function is given by

$$f_R\left(r\right) = \frac{r}{\sigma_r^2}\exp\left(-\frac{r^2}{2\sigma_r^2}\right) \qquad r \geq 0 \tag{3.8}$$

where r represents the envelope of the received signal and σ_r^2 its variance.

It is noteworthy that in case of requiring the instantaneous received power, that is, the square of the envelope, it has been shown that it follows an exponential distribution whose probability densisty function is defined as follows [53]:

$$f_S\left(s\right) = \frac{1}{2\sigma_s^2}\exp\left(-\frac{s}{2\sigma_s^2}\right) \tag{3.9}$$

where s is the square of the envelope of the received signal and again, σ_s^2 represents the variance.

Conversely, if there is a dominant component (perhaps LOS conditions), the envelope of the received signal tends to be distributed according to a Rice distribution, whose probability density function is:

$$f_R(r) = \frac{r}{\sigma_r^2} \exp\left(-\frac{A^2 + r^2}{2\sigma_r^2}\right) I_o\left(\frac{Ar}{\sigma_r^2}\right) \qquad (r \geq 0, A \geq 0) \tag{3.10}$$

where r continues representing the envelope of the received signal, A is the envelope of the dominant component and $I_o(\cdot)$ is the modified Bessel function of the first kind and zero–order.

At the same time, the Rice distribution is characterized by a parameter commonly known as Ricean factor or K–factor which is defined as:

$$K = \frac{A^2}{2\sigma_r^2} \tag{3.11}$$

where A^2 represents the power of the dominant component and $2\sigma_r^2$ the variance of the multipath. As the dominant component decreases, the K–factor tends to zero ($-\infty$ dB), thus the Rice distribution turns into a Rayleigh distribution. Fig. 3.3 illustrates the Ricean PDF for different K–factor values.

Lastly, it is important to remark that even though the aforementioned distributions are the most used since they constitute a theoretical basis that has been tested experimentally in a huge variety of propagation scenarios, they are not enough to characterize the fluctuations of the received signal strength in all cases. For instance, other distributions like Weibull or Nakagami has been employed in experimental outdoor propagation scenarios [54, 55].

3.2.4 Amplitude and phase small–scale modeling for MIMO channels

As it was commented before, channel modeling is of critical importance for the design, evaluation and optimization of wireless communication systems. It can be performed in different ways, with different levels of complexity depending on the approach adopted.

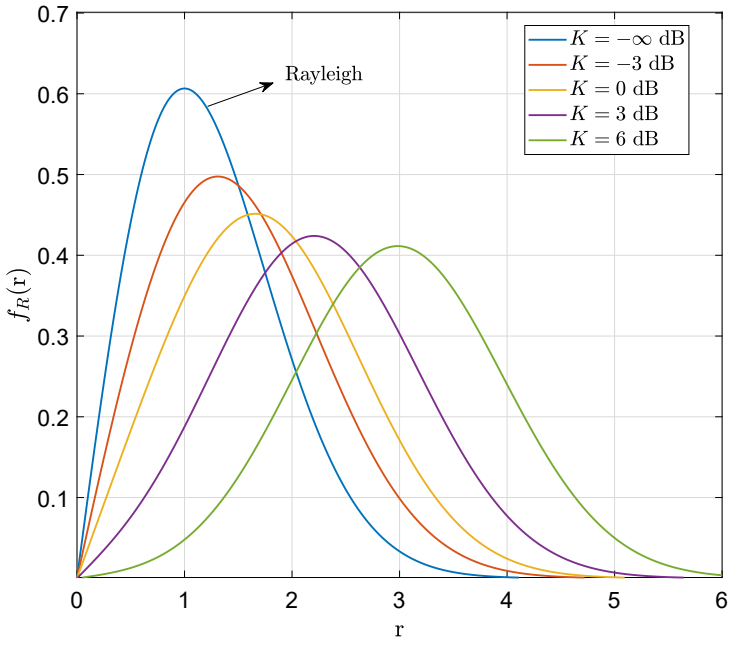

FIGURE 3.3: Rice probability density function for several K–factor values.

As a result, there are also several forms to classify channel models. Attending to the channel type, it is possible to distinguish between narrowband and wideband models as well as between time-varying and time-invariant models.

In the first distinction, the channel is considered as narrowband or wideband depending on the relationship between the system bandwidth, B, and the coherence bandwidth of the channel, B_c, which is understood as the bandwidth in which the frequency response of the channel remains approximately constant. Specifically, if $B_c > B$ the channel is considered narrowband and is characterized by the power levels and the multipath fading. Conversely, if $B_c < B$ the channel is considered broadband, the power delay profile and the autocorrelation function in frequency are required for its characterization. In the second distinction, a channel is considered to be linear time-invariant when the transmitter, receiver and the environment are all stationary, and then the attenuations and propagation delays of the channel impulse response (see equation (3.1)) do not depend on time. Otherwise, the channel is classified as time-varying and a channel characterization that accounts for its temporal evolution according to determined Doppler features is required.

If, on the other hand, only the channel modeling method is being considered, it is possible to distinguish between physical and non-physical models [56]. In this Thesis,

this last classification attending to the channnel modeling method is selected in order to explore the modeling of MIMO channel realizations. An overview of this classification is depicted in Fig. 3.4.

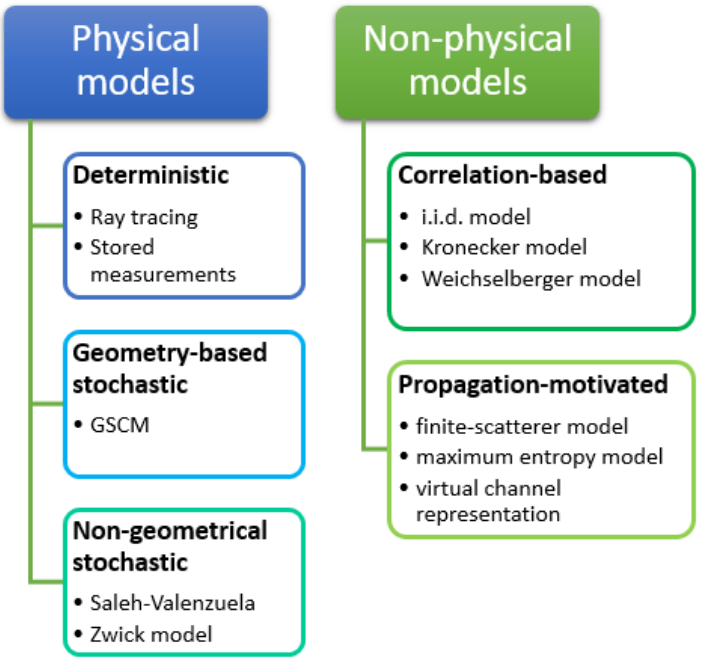

FIGURE 3.4: Physical and non-physical models classification based on [56].

Physical channel models

Physical channel models are focused on the propagation mechanisms that take place between the transmitter and the receiver describing the multipath components parameters like the direction of arrival (DOA), the direction of departure (DOD) or the delay of the multipath components. These models are very useful because of their independence with the antenna configuration (number of antennas, radiation pattern, array geometry, mutual coupling) and because they describe the propagation on their own. Withing physical propagation models three subgroups can be distinguished: deterministic, stochastic based on geometry and stochastic without geometric input.

Physical channel models are considered deterministic when their objective consists of reproducing the exact physical radio propagation for a precise location. Therefore, in this case very detailed information of the propagation environment such as the location, geometry, electromagnetic features of each and every one of the objects or physical conditions is required. With these data is possible to generate databases with the aim that the specific propagation process can be latter simulated. Among the benefits presented

by deterministic models underline their accuracy and physically meaningful of the propagation environment they offer. They are very useful when carrying out a measurement campaign is not feasible. Among the drawbacks is the large computational load that is required. Within the deterministic subcategory we should remark the commonly used Ray-Tracing model [57, 58] where basically the transmitter and receiver locations are specified and from them and according to geometric considerations and the geometrical optics rules, all existing paths among them are determined.

For its part, any channel model based on geometry is determined by the scatterer positions. In deterministic geometrical approaches like the aforementioned Ray-Tracing, those positions are collected in a database. Unlike them, geometry-based stochastic channel model (GSMC) select the scatter positions in a random (stochastic) manner following a certain probability distribution. Finally, other category of stochastic models but not based on the geometry of the propagation environment can be distinguished. There are two classes reported in the literature. The first one uses clusters of multipath components and is known as the extended Sale-Valenzuela model since it generalized the model proposed in [59], while the second one called Zwick model deals with the multipath components individually [60].

Non-physical channel models

Unlike physical models, non-physical channel models analytically characterize the channel matrix (impulse response) without explicitly taking into consideration the wave propagation. This type of channel models can be splitted into propagation-motivated models and correlation-based models. The first subcategory models the channel realizations by means of propagation parameters [61, 62], while the second subcategory models the MIMO channel matrices statistically according to the existing correlation between subchannels. The most outstanding models based on correlation include Weichselberger [63, 64] and Kronecker [65, 66] models. Since the correlation–based model will be used as baseline model to generate the synthetic MIMO channel matrices of this chapter, it will be explored with further detail below.

In most propagation environments, channel small–scale statistics are expected to follow a Rayleigh/Ricean distribution. If that is the case, it is common to assume that a narrowband MIMO channel sample should match the following model at each time instant.

$$\mathbf{H} = \sqrt{\frac{K}{K+1}}\mathbf{H}_{\text{LOS}} + \sqrt{\frac{1}{K+1}}\mathbf{H}_{\text{NLOS}} \tag{3.12}$$

This model characterizes the channel as a combination of both specular and diffuse propagation signal components. The former are represented by the deterministic gain–matrix $\mathbf{H}_{\text{LOS}}$, while the latter are characterized by the matrix $\mathbf{H}_{\text{NLOS}}$, which consists of complex Gaussian elements. K is the Rician K–factor, which contributes to the small–scale fade behavior for each of the $N \times M$ propagation channels conforming the $\mathbf{H}$ matrix [67]. We note that while the notation may suggest that for LOS scenarios only the first term exists and conversely for NLOS $\mathbf{H} = \mathbf{H}_{\text{NLOS}}$, actual channels will normally not match such extreme conditions. Specifically, a dominant signal component may exist even in severely obstructed environments, while the LOS condition does not preclude the presence of diffuse multipath propagation.

Now, we focus on the definition of the NLOS part of the channel matrix given by (3.12). Specifically, it can be defined in different manners depending on the selected correlation model. In its most general sense, the NLOS correlation matrix can be defined as follows:

$$\mathbf{R}_{\text{NLOS}} = \mathbb{E}\left[\text{vec}\,(\mathbf{H})\,\text{vec}\,(\mathbf{H})^{\dagger}\right] \tag{3.13}$$

where vec (.) denotes the vec operator. Taking into account this definition of the correlation matrix, the $N \times M$ complex Gaussian random matrix $\mathbf{H}_{\text{NLOS}}$ with zero mean and unit variance can be modeled as

$$\mathbf{H}_{\text{NLOS}} = \text{unvec}\,(\mathbf{h}_{\text{NLOS}}) \quad \text{with } \mathbf{h}_{\text{NLOS}} = \sqrt{\mathbf{R}_{\text{NLOS}}}\mathbf{h}_{\text{iid}} \tag{3.14}$$

Here, $\mathbf{h}_{\text{iid}}$ defines a $NM \times 1$ vector composed by zero mean and unit variance i.i.d. complex Gaussian random elements and $\sqrt{\mathbf{R}_{\text{NLOS}}}$ denotes any matrix square root fulfilling $\mathbf{R}_{\text{NLOS}} = \sqrt{\mathbf{R}_{\text{NLOS}}}(\sqrt{\mathbf{R}_{\text{NLOS}}})^{\dagger}$.

It should be noticed that the direct application of the model defined in (3.14) requires full knowledge of the spatial correlation. Therefore, with the aim of alleviating this requirement different models (i.e. Kronecker, Weichselberger) that establish a certain structure for the correlation matrix have been proposed.

Firstly, we explore the Kronecker model [65, 66] which assumes that the spatial correlation at the transmitter and the receiver are separable. Mathematically this is equivalent to express the correlation matrix via the Kronecker product as follows:

$$\mathbf{R}_{\mathrm{NLOS}} = \mathbf{R}_{\mathrm{T}} \otimes \mathbf{R}_{\mathrm{R}} \tag{3.15}$$

where $\mathbf{R}_{\mathrm{T}}$ and $\mathbf{R}_{\mathrm{R}}$ model the spatial correlation at the transmitter and receiver respectively that depend on the antenna deployments and on the scattering characteristic of the channel [68], its calculation will be described in Section 3.4.

Under the above definition of the NLOS correlation matrix, the $\mathbf{H}_{\mathrm{NLOS}}$ matrix which is a $N \times M$ complex Gaussian random matrix with zero mean and $\mathbb{E}\left[\|\mathbf{H}_{\mathrm{NLOS}}\|_F^2\right] = N \times M$ can be defined as:

$$\mathbf{H}_{\mathrm{NLOS}} = \sqrt{\mathbf{R}_{\mathrm{R}}}\mathbf{H}_{\mathrm{iid}}\sqrt{\mathbf{R}_{\mathrm{T}}} \tag{3.16}$$

where $\mathbf{H}_{\mathrm{iid}}$ is an i.i.d. complex Gaussian random matrix that would account for the diffuse propagation with no correlation.

Based on the previous model, it is easy to analyze the particular i.i.d MIMO model, also known as canonical, which is considered as the simplest one. In this particular case, all subchannels that integrate the MIMO channel matrix $\mathbf{H}_{\mathrm{NLOS}}$ are uncorrelated. Physically, this model refers to a rich scattering propagation environment and also contemplates a distance among the antenna elements (inter–element distance) large enough at both transmitter and receiver, giving rise in this way to statistically independent multipath components [69, 70]. In this case, the correlation matrix is defined as:

$$\mathbf{R}_{\mathrm{NLOS}} = \mathbf{R}_{\mathrm{T}} \otimes \mathbf{R}_{\mathrm{R}} = \mathbf{I}_{NM} \tag{3.17}$$

where $\mathbf{I}_{NM}$ is the $NM \times NM$ identity matrix. Consequently, the NLOS MIMO matrix is given by:

$$\mathbf{H}_{\mathrm{NLOS}} = \sqrt{\mathbf{I}_N}\mathbf{H}_{\mathrm{iid}}\sqrt{\mathbf{I}_M} \tag{3.18}$$

Despite the fact that these two previous models are the ones that will be employed in this Thesis, it should be noticed that as stated above, in the literature other correlation-based models have appeared like the Weichselberger model [63, 64] that tries to alleviate the separability restriction established by the Kronecker model and takes into account the existing coupling between the transmitter and the receiver. With this aim $\mathbf{H}_{\text{NLOS}}$ considers in its definition the eigenvalue decomposition of the transmitter and receiver correlation matrices:

$$\mathbf{H}_{\text{NLOS}} = \mathbf{U}_R \left(\widetilde{\Omega} \odot \mathbf{H}_{\text{iid}} \right) \mathbf{U}_T^{\intercal} \tag{3.19}$$

where $\mathbf{U}_T$ and $\mathbf{U}_R$ are unitary matrices whose columns are the eigenvectors of the transmitter and receiver correlation matrices, respectively, $\odot$ represents the Hadamard product and $\widetilde{\Omega}$ is the element–wise square root of a coupling matrix Ω whose elements represent the average power coupling between the transmitter and receiver eigenmodes.

3.3 Measurement Description

With the aim of empirically characterize the large–scale fading and the MIMO channel realizations that enables to model the small–scale fading, an O2I measurement campaign was performed at Universidad Técnica Federico Santa María (UTFSM) in Valparaíso (Chile), in two different locations as illustrated in Fig. 3.5, using a narrow–band channel sounder which operates at 3.5 GHz. In order to assure the stability of the channel conditions, measurements were performed at night avoiding the presence vehicles or pedestrians. It should be remarked that despite the use of a narrow–band sounding system, our measurements are applicable to broadband communication scenarios since multi–carrier modulations enable a broadband transmission over multiple narrow–band channels.

FIGURE 3.5: Location map of the UTFSM university and the two different scenarios where the measurement campaign was performed.

3.3.1 Measurement scenarios

Two different buildings (B1 and B2) considered as representative locations to emulate O2I propagation environments, where conventional communications are not always guaranteed, were selected to perform the measurement campaign. The continuous wave 3.5

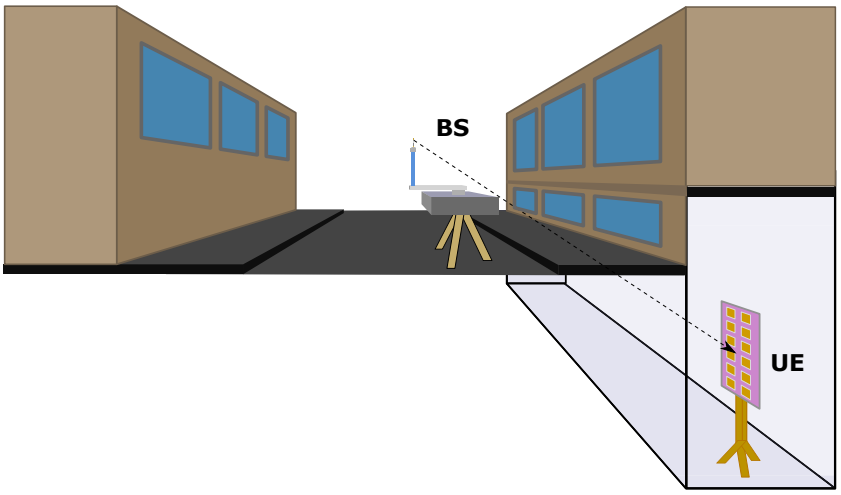

FIGURE 3.6: Representation of the O2I measurement configurations.

GHz BS was placed in several outdoor locations on the street next to the buildings, while the UE, which consists of a planar array of textile antennas, was placed in various indoor locations underground with respect to the street level (see Fig. 3.6) either in B1 or B2. More details about these two scenarios are given as follows:

- Building 1 (B1)

  The first underground location has a floor level 2 m below street level, and the underground room where the UE is situated is 3 m high. In addition, this indoor room is separated from adjacent spaces (e.g. hall, rooms, etc) by concrete walls. For its part, the upper portion of the steel–reinforced concrete wall facing the street has 1 m high glass windows. There are no doors in the facade that stand between the BS placed outdoor and the UE placed indoor.

- Building 2 (B2)

  The second underground placement consists of a tall garage with large 15 m^2 glass windows facing a street. Floor level is approximately 3 m below street level, and the total height of the room is 7 m. The building is separated from the street by thick 1 m high steel–reinforced concrete walls supporting the aforementioned windows. Again there are no doors in the facade that stand between the BS placed outdoor and the UE placed indoor.

  It should be noted that both indoor locations were not unobstructed spaces, but there were different scattered obstacles, mainly office furniture.

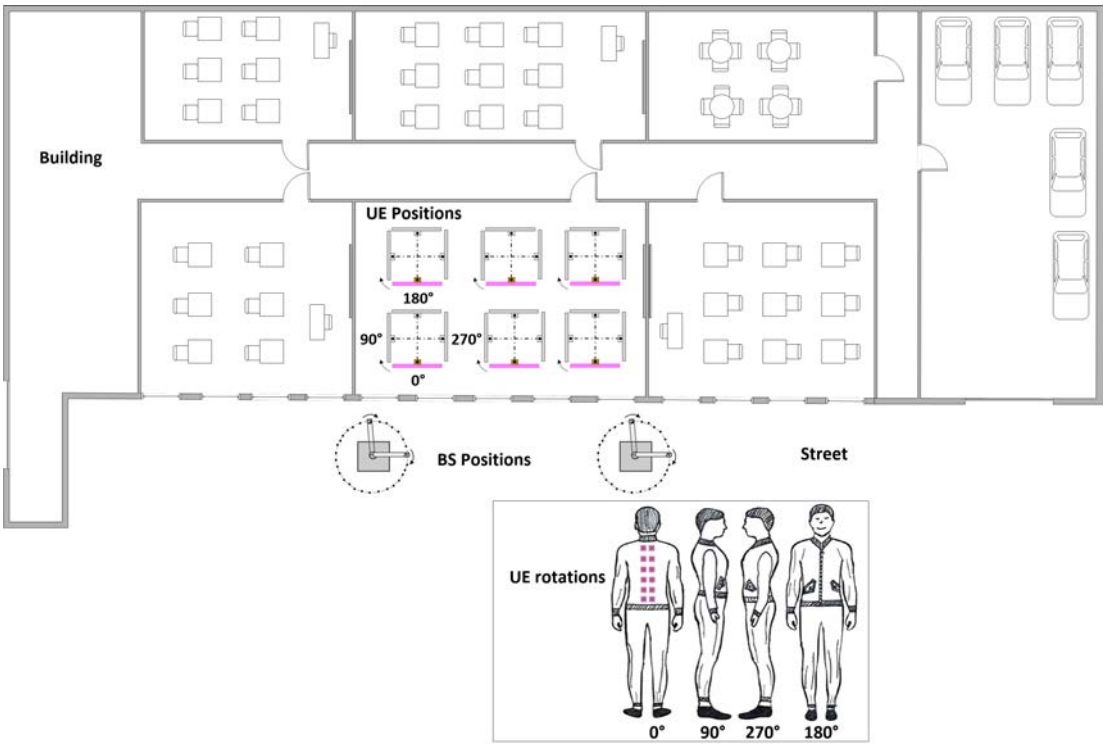

(a) Measurement location map of Building 1 (B1). Two outdoor positions for the transmitter with the rotating arm (BS) and six indoor positions for the UE, each position with four rotations in 0°, 90°, 180° and 270° with respect to the BS.

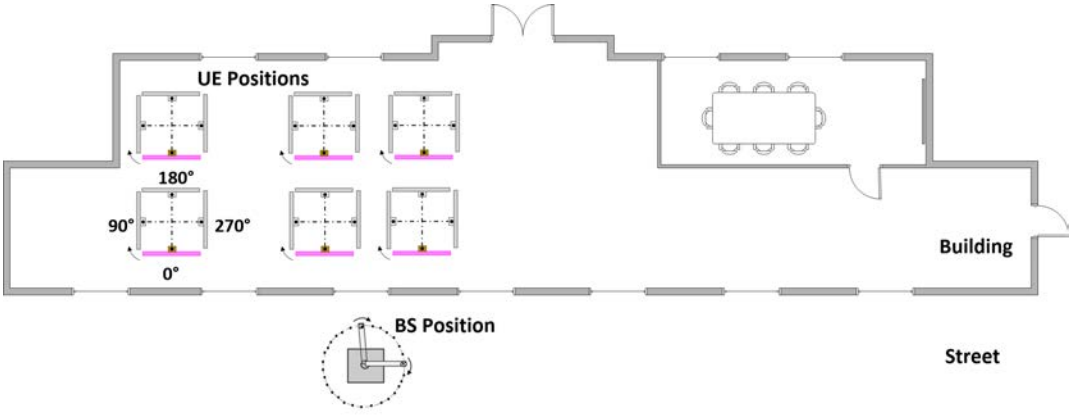

(b) Measurement location map of Building 2 (B2). One outdoor position for the transmitter with the rotating arm (BS) and six indoor positions for the UE, each position with four rotations in 0°, 90°, 180° and 270° with respect to the BS.

FIGURE 3.7: Schematic representation of the two buildings (B1 and B2) chosen for the measurement campaing.

The transmitter simulating a base station was placed at two outdoor locations facing B1 and one outdoor location facing B2, respectively. The measured placements in both B1 and B2 are represented in Fig. 3.7 (not drawn to scale). On the other hand, it is observed that the planar array integrated by textile antennas was placed in 6 different positions within the underground sites. For each of the six indoor locations, the UE antenna was

oriented in four different angles with regard to the BS (0°, 90°, 180° and 270°, see Fig. 3.7) imitating in this way a scenario where users have the wearable UE integrated in their clothing and they are constantly moving. As a result, a total of 72 links (different relative positions of the transmitter and receiver) were tested, corresponding 48 of them to building 1 and 24 to building 2.

3.3.2 Experimental setup

To perform an experimental characterization of the MIMO–textile solution, the automated sounding system represented in Fig. 3.8 is employed. It is important to note that this channel sounder has been designed for the direct measurement of 1×4 single-input multiple-output (SIMO) channels at the same time.

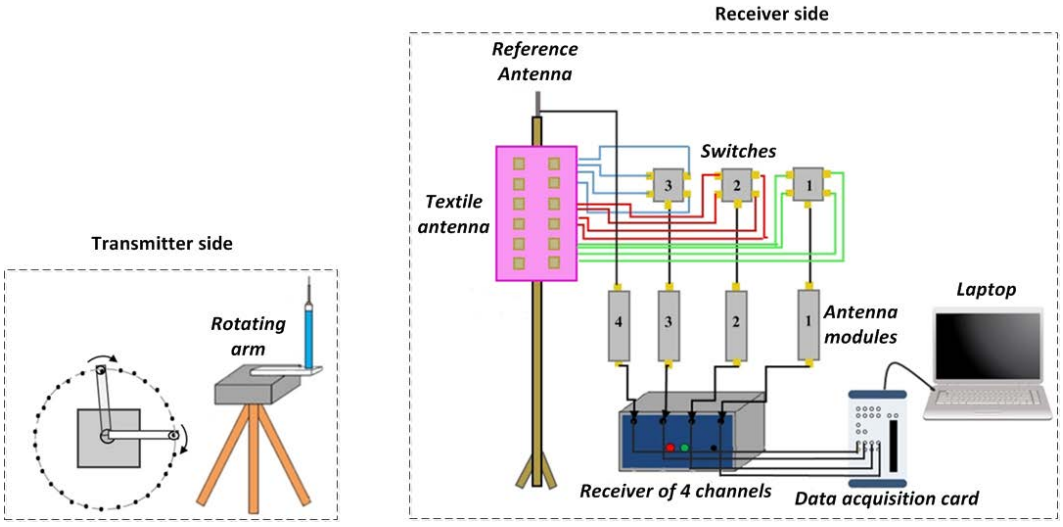

FIGURE 3.8: Channel sounder. Description of the transmitter side with a dipole antenna connected to a rotating arm implementing 30 different positions for the transmit antenna. Description of the receiver side including the textile planar array, the 4–channel receiver module, data acquisition card and processing laptop.

The narrow–band MIMO transmitter consists of a classic virtual array [71] created through a dipole antenna and a mechanical 0.5 m rotating arm. Specifically, the transmitting dipole is mounted on the rotating arm and moved step-wise under computer control via software tools implemented in Matlab and LabVIEW, in 12° angular increments, leading to the creation of a circular array integrated by 30 radiating elements as illustrated in Fig. 3.8. The inter-element distance is $\times 2.8$ the half wavelength assuring minimal MC. In this scenario the transmitter correlation will mostly be dependent on the channel scattering features.

For its part, the receiver is connected through a set of switches to a 6×2 element textile antenna array deployed at the user equipment. In particular, groups of 4 antennas are connected to 3 Single–Pole Four–Throw (SP4T) switches, which sequentially connect one antenna from each group to the input of the 4–channel receiver. Meanwhile, the fourth receive channel is permanently connected to a reference antenna. This way for each transmit antenna position, 12 channels to the respective UE antennas are measured. The logical sequence of performed operations is synthesized as follows:

1. The transmitting antenna is continuously emitting a 14.4 dBm wave carrier at 3.5 GHz.
2. At the receiver side, the first antenna of each set of switches is activated and samples are acquired (activated antennas at the receiver are 1-5-9-Ref).
3. At the receiver side, the second antenna of each set of switches is activated and samples are acquired (activated antennas at the receiver are 2-6-10-Ref).
4. At the receiver side, the third antenna of each set of switches is activated and samples are acquired (activated antennas at the receiver are 3-7-11-Ref).
5. The rotating arm is displaced 12° clock–wise.

The above sequence is repeated until completing 30 different positions for the rotating arm, which is equivalent to a 360-degree turnaround.

Regarding the textile antenna deployed at the receiver side, the design process followed was presented in Chapter 2. The textile antenna array is integrated by 12 individual squared patch antennas of length 3.3 cm using a 0.3 cm thick felt (with permittivity ϵ_r = 1.38) as a dielectric material. Its geometry follows $N_h = 2$ columns in the horizontal plane and $N_v = 6$ antenna rows in the vertical plane. Then, the total array size is $N = N_v \times N_h = 12$ antennas occupying 15×38 cm^2. To minimize MC between antennas at the receiver we selected an inter-element distance of 0.7λ, obtaining simulated MC values below -20 dB. The design and characterization of antenna parameters such as MC were performed using CST Microwave Studio.

Then, keeping in mind the explained above, the measured MIMO channel matrices are obtained by combining the captured SIMO channels. Concretely, in this work 72 MIMO

channel matrices formed by $12 \times 30 = 360$ SISO channels each have been measured. As a result, a total of ≈ 26.000 SISO channel fading samples have been measured.

The channel sounder uses the procedure described in [72] to measure the complex path–gains that form the MIMO channel matrix for each of the $L = 72$ radio links (each corresponding to a different relative position of the transmitter and receiver). The carrier frequency is down-converted to baseband by the 4–channel receiver, giving rise to outputs at 10 kHz that are sampled at 2×10^5 samples/s by a data acquisition card for 1 second. This time record is partitioned into 100 subintervals, each of which contains an integer number of cycles of the received sinusoid. To extract the amplitude and phase of the fading coefficient, we apply the Fast Fourier Transform (FFT) to the samples for each subinterval. The fact that for each 1-second acquisition we obtain 100 closely-spaced measurements allows verifying proper equipment operation as our measurement procedure includes verifying that these are consistent. In the case of the amplitude this corresponds to variations of less than 0.5 dB. Averaging these 100 measurements further reduces the measurement noise.

TABLE 3.2: Summary of measurement conditions.

Operating frequency	3.5 GHz
Tx power	14.4 dBm
Number of measured links	72
Distance range	5.2-11.2 m

Finally, the relative phase of each channel was obtained as the phase difference with respect to the reference antenna. Transmitter and receiver oscillators were locked to GPS disciplined sources to ensure phase coherence during the measurements for each group of 3 UE antennas. The phase shift that occurs at the transmitter while sequentially switching between each group of 3 antennas is compensated using the reference channel which continuously tracks this phase.

3.4 Empirical channel statistics and modeling

The measurement campaign undertaken to characterize the O2I underground scenario, as detailed in Section 3.3 provides the relevant information to statistically model the selected O2I propagation scenarios. In this section, we firstly introduce the normalization procedure of the measured MIMO channel matrices and try to understand it from a physical perspective. Then, a brief theoretical background for the model–parameter estimation, which includes the choice of estimators and the validation of the model fit is presented. A total of 72 12×30 channel matrices were measured and processed to extract all the required parameters. Specifically, the characterization of large–scale fading and small–scale fading is described, providing the basis for the experimental performance evaluation in terms of achievable data–rate to be discussed in Section 3.5.

From now on, it should be underlined that each baseband measured channel realization, $\mathbf{H}_{\text{meas}}$, following the channel model presented in (3.2) and (3.12), can be modeled as

$$\mathbf{H}_{\text{meas}} = \sqrt{G\frac{1}{d^{\alpha}}X_s}\left(\sqrt{\frac{K}{K+1}}\mathbf{H}_{\text{LOS}} + \sqrt{\frac{1}{K+1}}\mathbf{H}_{\text{NLOS}}\right) \tag{3.20}$$

where the term G denotes a gain due to the communication equipments, etc. and it is common to all the antennas, while $\frac{1}{d^{\alpha}}$ and X_s represent the path–loss and the shadow fading contributions, respectively. Taking the above definition into account the square Frobenius norm of each measured channel matrix $\mathbf{H}_{\text{meas}}$, or in other words, the received power can be decomposed as follows

$$\|\mathbf{H}_{\text{meas}}\|_F^2 = G\frac{1}{d^{\alpha}}X_s \|\mathbf{H}\|_F^2 = G\frac{1}{d^{\alpha}}X_s MN \tag{3.21}$$

3.4.1 Normalization of the measured channel realizations

It is of high relevance to consider that the achievable rate of MIMO systems is highly dependent on the normalization of the channel realizations [73]. Specifically, a proper normalization of the MIMO channel matrices enables to carry out fair comparisons (equal power) when the UE is located at different positions. In this Thesis, the normalization is

carried out on each channel realization, leading to the common assumption of constant received SNR.

Let us define the normalized MIMO channel matrix as

$$\mathbf{H}_{\text{norm}} = \frac{\mathbf{H}_{\text{meas}}}{\delta} \tag{3.22}$$

where δ is the normalization constant and its definition directly impacts on the meaning that the received power takes.

Once the basic concept has been defined, next one of the most widely extended procedures of normalization is explored [73]. This procedure considers that the normalization constant is defined as

$$\delta = \sqrt{\frac{\|\mathbf{H}_{\text{meas}}\|_F^2}{MN}} \tag{3.23}$$

At this moment, it is worthwhile to keep in mind that every time $\mathbf{H}_{\text{meas}}$ is divided by its square Frobenius norm during the normalization procedure, the aforementioned effects that contribute to the total received power value are being disregarded. Having said that, the normalization corresponding to the normalization constant defined above is given by

$$\|\mathbf{H}_{\text{norm}}\|_F^2 = MN \tag{3.24}$$

Furthermore, depending on the normalization procedure adopted, the physical meaning of the SNR significantly varies. Then, if we want to provide meaningful performance results, the normalization should be carefully selected. In this Thesis, the normalization procedure presented above will be applied with some nuances since the received Signal–to–Noise ratio will be dependent on the shadow fading ($\mathsf{SNR} = \mathsf{SNR}_{\text{ref}} X_s$), assuming that distance dependent path–loss is compensated by means of transmit power control. This is again detailed in Subsection 3.5.2. It should be noticed that the opposite situation of considering the different pathloss values would lead to obtain different values of received SNR. This case may correspond to a MIMO system with fixed transmit power as considered in [74].

3.4.2 Large–scale fading

The measurements were carried out for 72 links with distances between the transmitter and receiver ranging from $5.2 - 11.2$ m, so the fluctuations in received power are proportional to distance–dependent path–loss (PL) variations and random shadow fade (SF). The variations in received power were obtained from the squared Frobenius norm of the measured channel matrices, $\mathbf{H}_{\text{meas}}$, at the different positions.

It is possible to determine the path-loss exponent value from the combined path–loss and shadowing effect described in (3.6). Considering a reference distance $d_o = 1$ m, the next equality is reached:

$$\underbrace{P_L\left(d\right)\left[dB\right] - 20\log_{10}\left(\frac{4\pi}{\lambda}\right)}_{y} = \underbrace{\alpha}_{slope}\underbrace{10\log_{10}\left(d\right)}_{x} + \underbrace{X_s}_{intercept} \tag{3.25}$$

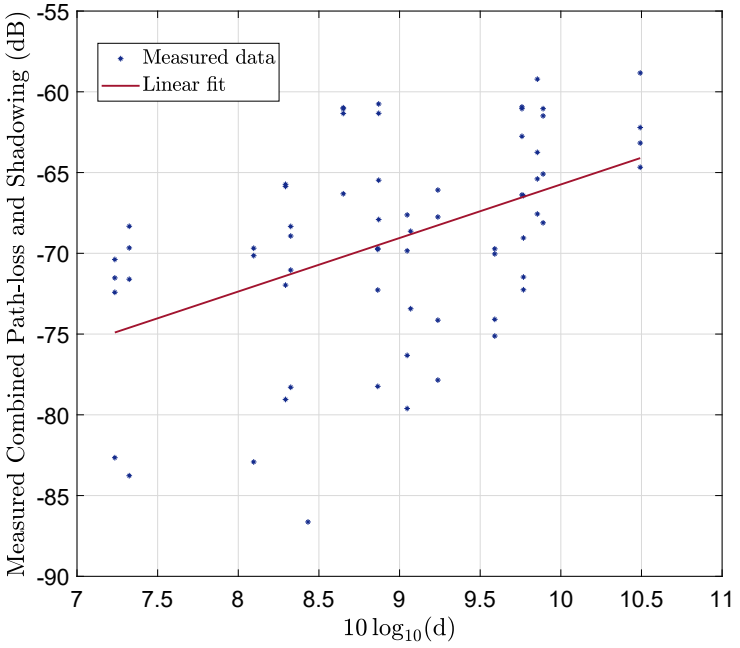

FIGURE 3.9: Measured combined path–loss and shadowing and linear regression analysis with $\alpha = 3.32$.

It must be noticed that knowing the BS–UE distances, $P_L\left(d\right)\left[dB\right]$ can be calculated as the difference between the transmitted power and the 72 empirical values of the received power, each one measured at a certain distance d. Finally, the path–loss exponent is

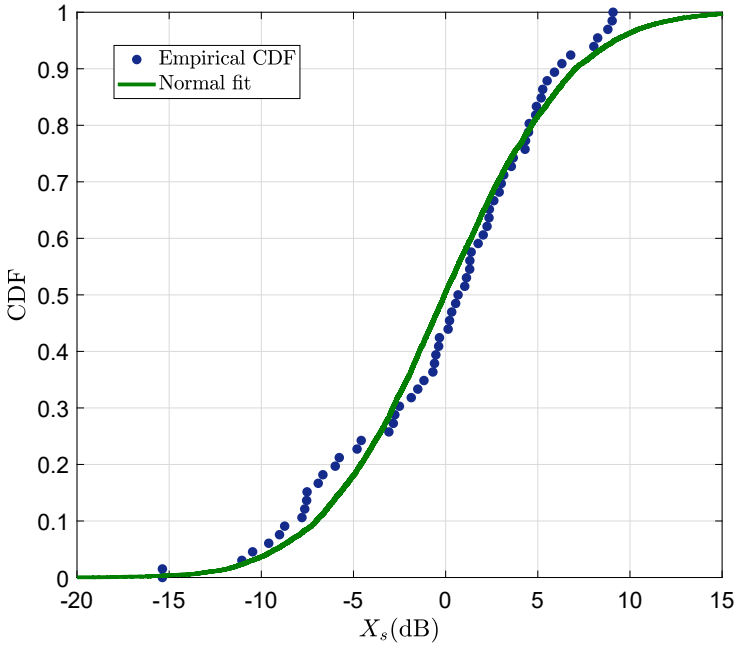

FIGURE 3.10: Measured CDF for normalized shadow fade statistics. The Normal fit for the distribution in dB is provided with parameters $\mu_{x_s} \approx 0$, $\sigma_{x_s} = 5.5$ dB.

obtained using LS linear regression fit as shown in Fig. 3.9. The PL exponent α, which matches the slope of the regression line, is estimated to be $\alpha = 3.32$.

SF values for each link/distance, noted as P_{x_s}, are obtained from the received power as the power deviation from the PL computed with path–loss exponent $\alpha = 3.32$. Applying the KS test with a significance level of 0.05 it was confirmed that the cumulative function distribution (CDF) of the empirical values for P_{x_s} matched the classical Log–Normal model [71] very well as shown in Fig. 3.10. Again, the model fit was obtained applying MLE method. The mean and standard deviation for this model were $\mu_{x_s} \approx 0$ dB and $\sigma_{x_s} = 5.5$ dB, respectively.

3.4.3 Small-scale fading

Under the assumption that the small–scale fading behavior can be extracted from (3.20), there are three parameters, the Ricean K–factor and the two channel correlation matrices that need to be estimated from the measurements. This is going to be done in subsections 3.4.3.1 and 3.4.3.2 respectively. With this aim K will be modeled as a position–dependent random variable, i.e. as a function of the specific characteristics of the place where the terminal is positioned. Given the nature of the test locations of

interest, we will be facing the challenging condition of estimating small Ricean K–factor values [75]. With regard to the correlation matrices, we will make the simplifying assumption that they do not vary significantly with location and that thus one set of values adequately models our environment. As it will be seen in Section 3.5, with proper choice of parameters, this simple model adequately describes the achievable spectral efficiency, illustrating its reduction with respect to assuming a strictly Rayleigh channel ($K = 0$).

3.4.3.1 Characterization of the K–factor

As it is illustrated in Fig. 3.11, the measurement campaign described in Section 3.3 has provided 72 different channel matrices representing different positions between the transmitter and receiver with $N = 12$ receivers in the textile planar array and a range of transmitters going from $M = 1 \dots 30$. Then, in each of the 72 positions, $30 \times 12 = 360$ fading coefficients which present the same K–factor have been measured. Without loss of generality we assume that in a static environment as the one measured and independently of the number of antennas considered, the K–factor does not change unless the surroundings of the transmitter and receiver vary. Therefore, the Ricean factor will change as soon as the position between transmitter and receiver varies. Based on these assumptions, it can be considered that the K–factor has a statistical behavior which can be described through an empirical CDF that will be latter calculated.

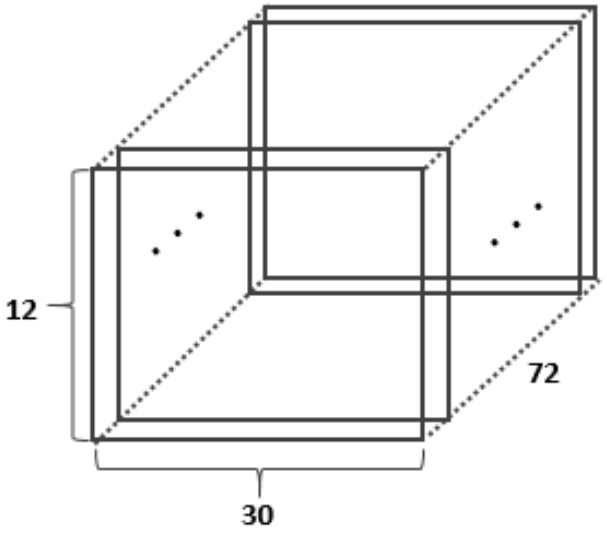

FIGURE 3.11: Graphical representation of the dimensions of the measured data.

The methods available to estimate the K–factor based on channel samples depend on the level of information available about the fading coefficients. For SISO links if only the fading coefficients amplitude is available, several approaches explore the relation between different statistical moments of the random envelope to estimate K [76, 77]. If both phase and amplitude are available, more accurate methods exist [78, 79], including some that can alleviate/eliminate the bias that affects amplitude-based methods [80]. Next, the performance of both, amplitude-based and I/Q-based estimation methods is characterized. Additionally, it is important to take into account that regardless of the estimation method, the K–factor CDF estimation is also very sensitive to the number of fading coefficients L_{est} used for obtaining each of the K estimates ($\hat{K}$) and also, the number of values $L_{\hat{K}}$ of $\hat{K}$ that would eventually provide the Ricean factor CDF. This is even more certain when low K values are expected. As L_{est} grows, $\hat{K}$ bias and variance is reduced, as $L_{\hat{K}}$ grows we would obtain a more accurate estimated CDF for K. In our measurement campaign there is a clear trade-off between both parameters given that we have a fixed number of channel matrix measurements. In order to determine which is the best estimation strategy given that $L_{est} \leq 30 \times 12 = 360$, the performance of the different estimators is simulated for different number of fading coefficients used to estimate each K value $L_{est} = \{12, 30, 360\}$. It should be noticed that these three numbers correspond to consider: the 12 fading coefficients that are defined between 1 antenna at transmitter and all the antennas at the receiver, the 30 fading coefficients that are defined between all the antennas at the transmitter and 1 antenna at the receiver or the 360 coefficients that are defined between all the antennas at the transmitter and receiver.

To carry out the performance characterization, firstly the mathematical definition of both approaches will be presented.

In the case of the amplitude-based estimator, $\hat{K}_{\mathrm{A}}$ is defined as follows [76]:

$$\hat{K}_{\mathrm{A}} = \frac{\sqrt{1-\gamma}}{1-\sqrt{1-\gamma}} \tag{3.26}$$

where γ is given as follows by the ratio of the variance of the received signal power and the mean of the received signal power.

$$\gamma = \frac{\mathbb{E}\left[|h|^4 - \mathbb{E}\left[|h|^2\right]^2\right]}{\mathbb{E}\left[|h|^2\right]^2}, \tag{3.27}$$

h is the complex channel coefficient of a SISO link and $|\cdot|$ represents the amplitude.

For its part, the I/Q-based estimation method can be defined as [79]:

$$\hat{K}_{\mathrm{IQ}} = \frac{|\mathbb{E}[h]|^2}{\mathbb{E}\left[|h - \mathbb{E}[h]|^2\right]} \tag{3.28}$$

Additionally, as it was mentioned before there are improved versions of the estimators based on both amplitude and phase. Specifically, a unbiased version of the I/Q-based estimator is given by [80]

$$\hat{K}_{\mathrm{IQ}_u} = \frac{1}{S}\left((S-2)\frac{|\mathbb{E}[h]|^2}{\mathbb{E}\left[|h - \mathbb{E}[h]|^2\right]} - 1\right) \tag{3.29}$$

where S represents the channel sample size available for the estimation.

Next, in Fig. 3.12 the simulated performance for the aforementioned estimators, obtained with 3000 synthetic channel samples is shown. The performance of these estimators is studied for $L_{est} = \{12, 30, 360\}$ providing the average $\mathbb{E}[\hat{K}]$ that gives information about the bias of the estimator and the confidence interval at 90% of $\hat{K}$. It is observed that the best estimation, as expected, is achieved by the unbiased version of the amplitude and phase estimator ($\hat{K}_{\mathrm{IQ}_u}$), obtaining estimated mean values equal to the real ones. Additionally, the amplitude-based estimator ($\hat{K}_{\mathrm{A}}$) presents the worst performance. Regarding to the fading coefficients L_{est} available for obtaining each of the K estimates ($\hat{K}$), it is clear that the lower its value, the less accurate the estimate will be. For instance, for $L_{est} = 12$ and $K = -10$ dB using the biased version of the amplitude based estimator, there is a difference of approximately 1 dB between the K estimate and the real one. However, for $L_{est} = 30$ and $L_{est} = 360$ the difference is reduced to 0.5 dB and 0 dB, respectively.

Similarly, in MIMO links the estimation of the Ricean component can be done using only the amplitude information of the components of the channel matrix applying the

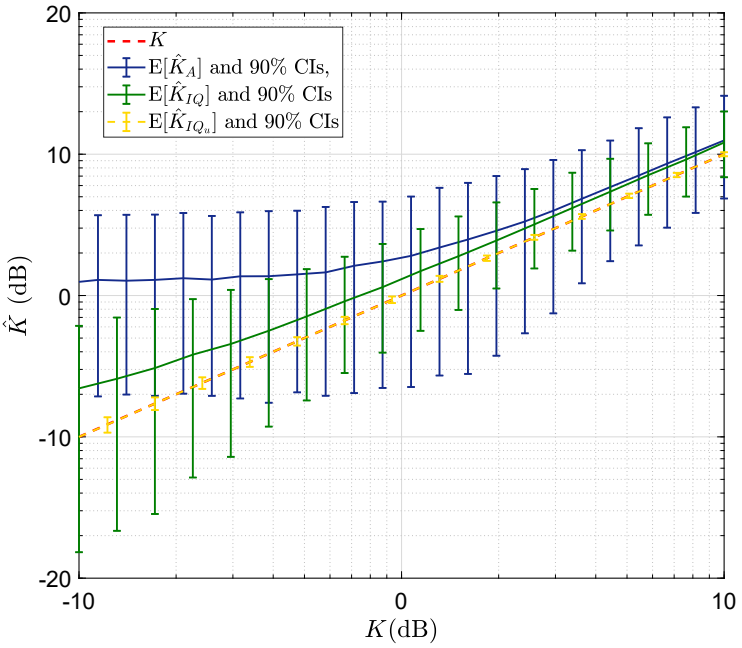

(a) $L_{est} = 12$

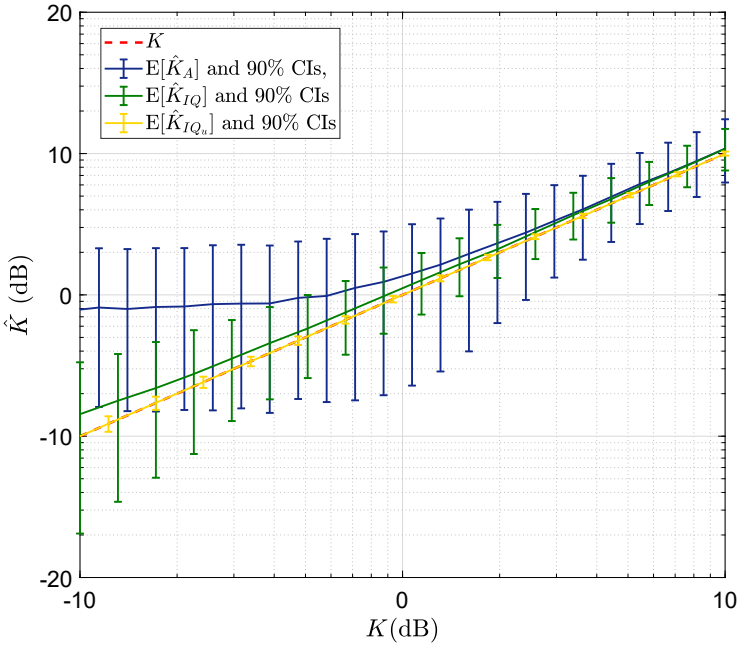

(b) $L_{est} = 30$

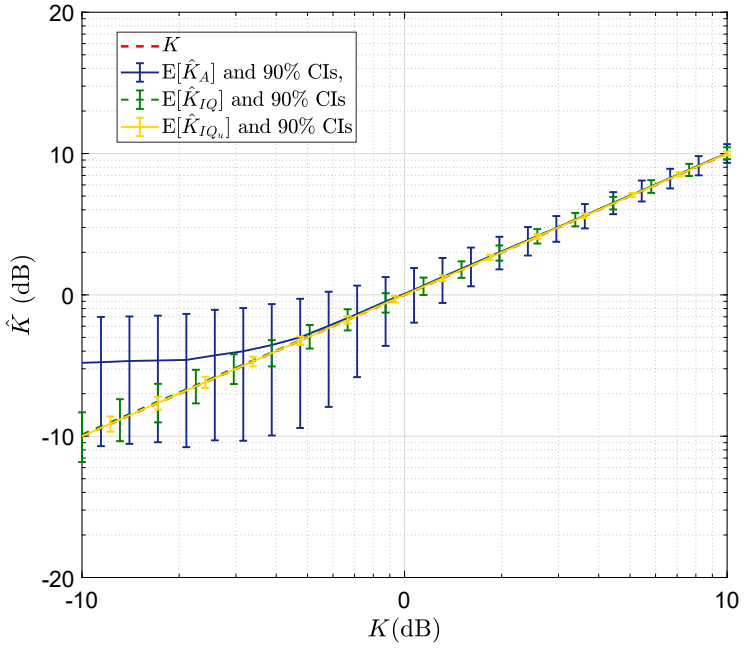

(c) $L_{est} = 360$

FIGURE 3.12: Simulated performance of different K–factor estimators ($\hat{K}_{\mathrm{A}}$, $\hat{K}_{\mathrm{IQ}}$ and $\hat{K}_{\mathrm{IQ}_u}$) with 90% confidence interval and $L_{est} = \{12, 30, 360\}$.

SISO philosophy [76, 77]. If the phase information is to be used in MIMO to estimate the K–factor, one must first estimate the phase variations of the dominant component resulting from the transmit antenna movement of the virtual array from those due to the diffuse components. This phase estimation has been reported in practice [81] for straight line movement but is very complex for a MIMO geometry with body worn antennas and a circular BS array such as here tested. Thus, given the difficulty of using phase information with body worn antennas, in this Thesis from now on, the amplitude–based estimator $\hat{K}_{\mathrm{A}}$, which is defined in expressions (3.26) and (3.27), will be employed.

Once the estimator has been selected, only its performance is characterized. In order to evaluate the impact that the number of fading coefficients L_{est} used for obtaining each of the K estimates $\hat{K}_{\mathrm{A}}$ have in the estimation quality, we show in Fig. 3.13 the simulated performance of the amplitude-based estimator for different number of fading coefficients $L_{est} = \{12, 30, 360\}$. For each L_{est} scenario, we provide the average $\mathbb{E}[\hat{K}]$ that gives information about the bias of the estimator and the confidence interval at 90% of $\hat{K}$. It is observed that in the three cases the estimator is biased. However, $L_{est} = 360$ bias is

negligible for a larger range of values of K ($K > -3$ dB). In addition, there is a clear trend, as L_{est} grows, $\hat{K}$ bias and variance is reduced.

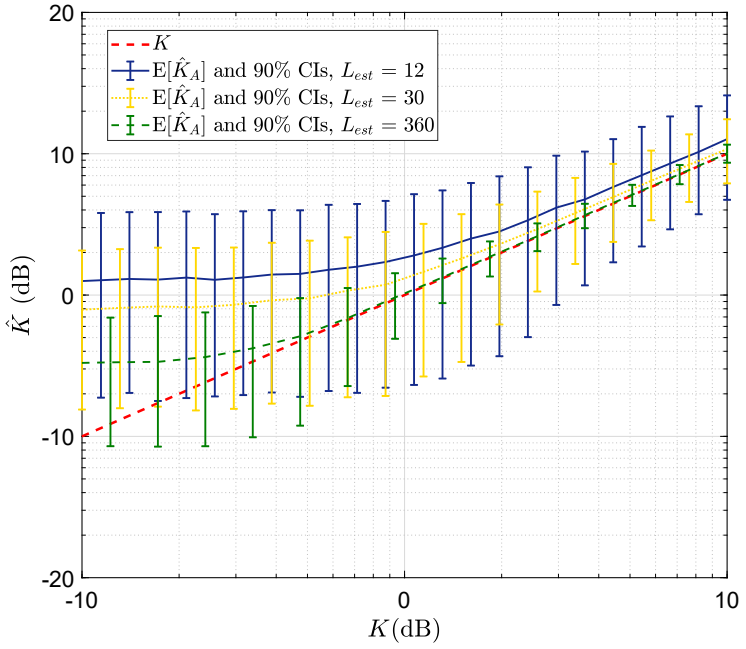

FIGURE 3.13: Performance of the amplitude-based K–factor estimator ($\hat{K}_{\mathrm{A}}$) with 90% confidence interval for different number of fading coefficients available for estimation $L_{est} = \{12, 30, 360\}$.

Therefore, once again, as expected, it is confirmed that using higher number of samples during the estimation process ($L_{est} = 360$) outperforms both in terms of lower bias and better (smaller) confidence interval the case of using less number of samples ($L_{est} = 12$) . Then, from now on $\left(L_{est} = 360, L_{\hat{K}} = 72\right)$ estimation parameters will be used to obtain the estimated CDF of the Ricean component in the measured scenarios.

Additionally, to complete the analysis of the sensitivity of the amplitude-based estimator with respect to the number of available fading coefficients, Fig. 3.14 illustrates the evolution of the normalized root mean square error (RMSE) in decibels, as a function of the number of fading coefficientes available for estimation. Specifically, the normalized RMSE enables to quantify the differences between the values predicted by the estimator and the real values. In view of the results, again it is confirmed that these differences increases as the number of fading coefficients decreases.

Based on our measured data we will illustrate that under the assumption of a channel model described by (3.20), a single value of the K–factor does not properly describe our O2I measured scenario, so the K–factor is going to be be modeled next

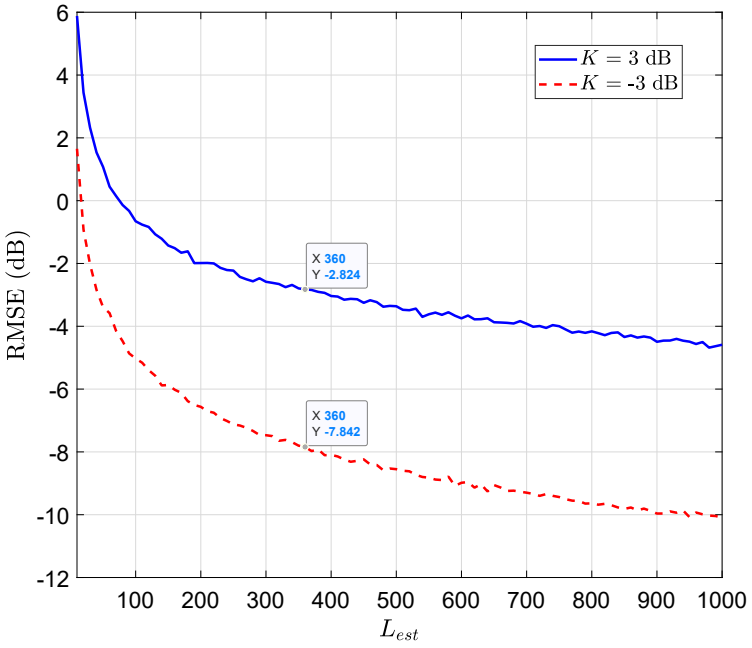

FIGURE 3.14: Normalized RMSE for $K = -3$dB and $K = 3$dB as a function of the number of fading coefficients available per channel sample (L_{est}).

as an environment–dependent random variable. As a first step, we have applied the Kolmogorov-Smirnov goodness–of–fit test (KS test) with a significance level of 0.05 to each of the 72 measured MIMO links. Thus implies that we are testing the statistical distribution of the 12×30 fading samples available in each measured link. As it has been previously mentioned, we assume that all the 360 fading share the same K value, therefore with the KS test we determine with proper choice of parameters that the links' small–scale fading statistics fits either a Rayleigh or a Rice distribution. This means that there is LOS type small–scale fade behavior with measurable specular component, despite the heavily obstructed nature of the channel at some nominally NLOS locations.

In each position of the transmitter and receiver (link), we obtain an estimation for the K-factor using (3.26) and (3.27). For each emplacement we use $L_{est} = 30 \times 12 = 360$ available fading coefficients to estimate the averages in (3.27), allowing a reasonably accurate estimation of the K–factor in that position [76]. Indeed, we have found via simulation that for this number of samples $\hat{K}_{\mathrm{A}}$ has a normalized root mean square error (RMSE) of -2.8 dB for $K = -3$ dB and -7.8 dB for $K = 3$ dB (see Fig. 3.14). Also, it is well known that the estimator $\hat{K}_{\mathrm{A}}$ in (3.26) provides negative non–feasible values for very low–values of K. In this scenario, there are different options that have been previously reported in the literature, one consists of setting these values to zero assuming

that a low K value was being estimated, while other consist of setting these values to its absolute value. In the results shown next we will use the latter.

Given that $L_{est} = 360$, for each of the 72 links we have one estimate for K, and from this we obtain the empirical CDF for the K–factor as shown in Fig. 3.15. The model fit was obtained applying maximum likelihood estimation (MLE) resulting in average $\mu_{\hat{K}_\mathrm{A}} = -3.5$ dB and standard deviation $\sigma_{\hat{K}_\mathrm{A}} = 3.3$ dB. Applying the KS test with a significance level of 0.05 we have verified that our estimated values can be assumed to have a Log–Normal distribution. The Log–Normal distribution of the K–factor in other measured environments has been reported before in the literature and used for channel modeling [71, 82, 83]. Finally, the CDF shown in Fig. 3.15 indicates that a significant specular component may be present despite the heavily obstructed nature of the channel.

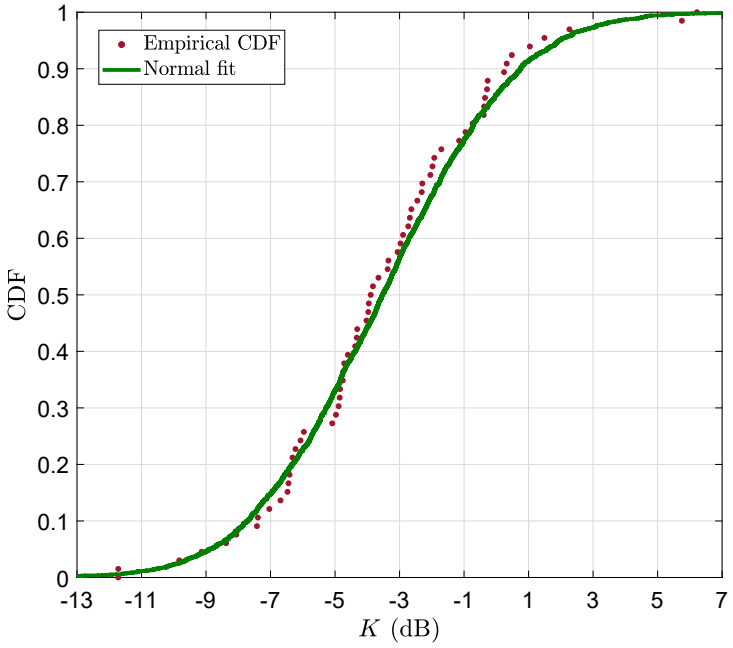

FIGURE 3.15: Estimated CDF for the Ricean factor. A Normal fit for the $\hat{K}$ distribution in dB is provided with parameters $\mu_{\hat{K}_\mathrm{A}} = -3.5$ dB and $\sigma_{\hat{K}_\mathrm{A}} = 3.3$ dB.

Comparing our results for a particular O2I propagation scenario (see Section 3.3) with those obtained in an urban O2O propagation scenario as the one reported in [83], it is concluded that in our case the values are typically lower, no more than 6 dB vs. 15 dB for O2O. On the other hand, if we compare our results with those obtained in other O2I environment (not underground) [71] we see a relative similarity corroborating that indoor locations tend to be very rich in multipath.

To conclude, it is important to highlight that the above statistical characterization of the K–factor allows us to classify the measured O2I scenario as a quasi–NLOS scenario, opening up the possibility of comparing in following sections the behavior of the empirical achievable rates with respect to that which would be achieved both in pure NLOS locations and in locations with K distribution following Fig. 3.15.

3.4.3.2 Spatial correlation modeling

In general, the basic idea behind the spatial correlation concept makes reference to the degree of statistical similarity that exists between two channels whose transmitting and/or receiving antennas are separated by a certain distance. In the literature, the characterization of the MIMO correlation has been addressed in different ways either through geometric models of the channel [84], simulations such as ray tracing [85, 86] or measurement campaigns [87, 88]. The analysis performed in this section aims to be a contribution to the study of spatial correlation an its influence on the performance of MIMO systems using antenna textile technology.

The spatial correlation depends on several factors. On the one hand, it depends on the antenna geometry (linear array, planar array, circular array, etc.) and its features (inter–element distance, radiation patterns, efficiency, mutual coupling, etc.). For instance, in [65] it is shown how increasing the distance between the elements that integrate the transmitter and receiver arrays leads to a reduction of the correlation and consequently the capacity is improved. In [89] a closed-form expression for the spatial correlation of a circular antenna array geometry is derived. On the other hand, the spatial correlation depends on the characteristics of the propagation environment which directly influence on the richness of the scattering and therefore condition the statistical characterization of the power angular spread (PAS) at the transmitter and receiver sides. In the literature, different approaches have been presented to model this function like the n^{th} power of a cosine function [90], the truncated Gaussian distribution [91], the uniform distribution [68] or the Laplacian [68, 90, 92]. Depending on the propagation environment some of those methods have been proven to yield a more accurate description of the PAS behavior. For instance, in [93] it is shown that the Laplacian distribution presents the best fit describing the measurement results in urban and rural macrocellular environments.

As indicated above, both the physical parameters of the antenna arrays and the characteristics of the propagation environment influence in the spatial correlation. In [94] is remarked that if there is a rich scattering environment, then the inter–element distance between the antennas has a limited impact, specially for separations equal or higher than $\lambda/2$ since low correlation is presented. However, if we talk about low scattering propagation environments, the inter-element distance is key to decorrelate the channels.

3.4.3.2.1 Mathematical perspective

To explore mathematically the concept, let's assume the separable correlation model for the generation of the NLOS channel component $\mathbf{H}_{\mathrm{NLOS}}$ as detailed in (3.16). Then, it is possible to write the $M \times M$ symmetrical complex transmit correlation matrix $\mathbf{R}_{\mathrm{T}}$ and the symmetrical complex $N \times N$ receive correlation matrix $\mathbf{R}_{\mathrm{R}}$ as [95]:

$$\mathbf{R}_{\mathrm{T}} = \begin{pmatrix} t_{11} & t_{12} & \cdots & t_{1M} \\ t_{12}^{*} & t_{22} & \cdots & t_{2M} \\ \vdots & \vdots & \ddots & \vdots \\ t_{1M}^{*} & t_{2M}^{*} & \cdots & t_{MM} \end{pmatrix} \tag{3.30}$$

$$\mathbf{R}_{\mathrm{R}} = \begin{pmatrix} r_{11} & r_{12} & \cdots & r_{1N} \\ r_{12}^{*} & r_{22} & \cdots & r_{2N} \\ \vdots & \vdots & \ddots & \vdots \\ r_{1N}^{*} & r_{2N}^{*} & \cdots & r_{NN} \end{pmatrix} \tag{3.31}$$

where t_{jl} and r_{ik} represent the spatial complex correlation coefficients between two elements j and l at the transmitter and i and k at the receiver, respectively. In Fig. 3.16 these coefficients are represented for a 2×2 MIMO case. It should be noticed that because of the hermitian nature of the correlation matrices [96], $t_{jl}{=}t_{lj}^{*}$ and $r_{ik}{=}r_{ki}^{*}$. Therefore, the calculation of the correlation matrices can be simplified to the calculation of the coefficients that are above the main diagonal as shown in (3.30) and (3.31).

Finally, the definition of these correlation coefficients is given by

$$t_{jl} = \langle h_{nj}, h_{nl} \rangle \qquad r_{ik} = \langle h_{im}, h_{km} \rangle \tag{3.32}$$

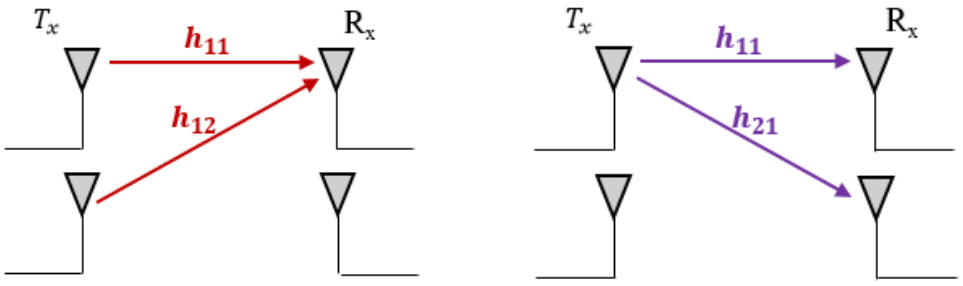

(a) t_{12} (b) r_{12}

FIGURE 3.16: Example of correlation coefficients for a 2×2 MIMO case : a) t_{12} is the correlation coefficient on transmission which represents the spatial correlation between channels with different transmitter ($j = 1$ and $l = 2$) but the same receiver ($n = 1$), b) r_{12} is the correlation coefficient on reception which represents the spatial correlation between channels with the same transmitter ($m = 1$) but different receiver ($i = 1$ and $k = 2$).

where $\langle v, u \rangle$ denotes the correlation coefficient between the random variables v and u and is defined as follows:

$$\langle v, u \rangle = \frac{\mathbb{E}\left[vu^*\right] - \mathbb{E}\left[v\right]\mathbb{E}\left[u^*\right]}{\sqrt{\mathbb{E}\left[|v|^2 - \left(\mathbb{E}\left[v\right]\right)^2\right]\mathbb{E}\left[|u|^2 - \left(\mathbb{E}\left[u\right]\right)^2\right]}} \tag{3.33}$$

3.4.3.2.2 Experimental characterization

Taking into account the separable correlation model [97] for the NLOS channel component $\mathbf{H}_{\text{NLOS}}$ defined in (3.16), both symmetrical complex correlation matrices at transmitter and receiver can also be written as [98]:

$$\mathbf{R}_{\text{T}} = \frac{1}{N}\mathbb{E}\left[\left(\mathbf{H}_{\text{meas}} - \mathbb{E}\left[\mathbf{H}_{\text{meas}}\right]\right)^{\dagger}\left(\mathbf{H}_{\text{meas}} - \mathbb{E}\left[\mathbf{H}_{\text{meas}}\right]\right)\right] \tag{3.34}$$

$$\mathbf{R}_{\text{R}} = \frac{1}{M}\mathbb{E}\left[\left(\mathbf{H}_{\text{meas}} - \mathbb{E}\left[\mathbf{H}_{\text{meas}}\right]\right)\left(\mathbf{H}_{\text{meas}} - \mathbb{E}\left[\mathbf{H}_{\text{meas}}\right]\right)^{\dagger}\right] \tag{3.35}$$

where $(\cdot)^{\dagger}$ represents the conjugate transpose.

Considering that all 72 links are geometrically similar, then PAS would not change among the different locations where we place the transmit and receive antennas. Given this, we can estimate both matrices in (4.2) and (3.35) from the channel measurements.

From these estimated correlation matrices, next a matching to an analytical correlation model for the transmitter and receiver respectively is provided. To do it, it is necessary to explore the several factors mentioned previously (array geometry, PAS, etc) since they determine the structure of the correlation matrices.

The virtual circular array at the transmitter with $M = 30$ should theoretically provide a $M \times M$ symmetric Toeplitz correlation matrix [68], where we can characterize the full matrix if we have the correlation between one of the antenna elements and the other 29 elements (i.e. one of the correlation matrix rows). Furthermore, we have an additional symmetry within the matrix rows due to the circular geometry of the transmitter array which implies that the correlation between one element and the closest 15 elements going through the array clock–wise is the same than moving counter clock–wise. Then, in this scenario, we could fully characterize the channel correlation matrix at the transmitter if we have the correlation between one antenna element and its 15 neighbors in any direction along the circle since $t_{12} = t_{130}$, $t_{13} = t_{129}$, $t_{14} = t_{128}$ and so on (see Fig. 3.17(a)).

When estimating the channel correlation at the transmitter defined in (4.2) with the channel measurements, we can easily identify in the obtained correlation matrix the symmetry behavior previously described. Therefore, we proceed to fit correlation coefficients for the 15 antenna elements using the least-squares (LS) method and from there expand to the full correlation matrix. Correlation models proposed in the literature [68] depend on the PAS distribution. Here, we test 3 alternatives to model the correlation through $\mathsf{sinc}(\cdot)$, $\mathsf{exp}(\cdot)$ and rational functions [68] as shown in Fig. 3.18. Using the least-squares criterion to find the best match to the measurements we found that the rational function provides the best fit, with an RMSE value of 0.08. For the correlation matrix first row we have $t_{1l} = \frac{b_{\mathbf{R}_\mathrm{T}}}{a_{\mathbf{R}_\mathrm{T}}} \frac{a_{\mathbf{R}_\mathrm{T}}}{(l-1)+b_{\mathbf{R}_\mathrm{T}}}$ with $l = 1 \ldots 16$ and $t_{1l} = (\mathbf{R}_\mathrm{T})_{1,M+2-l}$ for $l = 17 \ldots 30$ with coefficients $a_{\mathbf{R}_\mathrm{T}}$ and $b_{\mathbf{R}_\mathrm{T}}$ as in Table 3.3. From the 30×30 correlation matrix, we can also obtain the correlation matrix for different antenna deployments $M < 30$ at the transmitter, simply defining a new Toeplitz matrix truncating the first row t_{1l} to $l = 1 \ldots M$.

The correlation at the receiver is an $N \times N$ matrix with $N = 12$ that again, theoretically, could be fully characterized if we model the correlation between one of the antenna elements and the other 11 (i.e. one of the correlation matrix rows). It should be

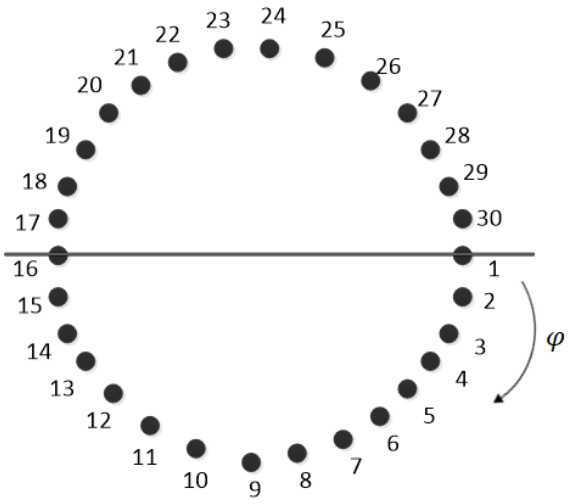

(a) Circular array geometry at transmitter.

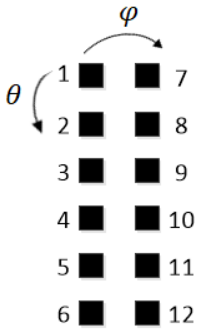

(b) Planar array geometry at receiver.

FIGURE 3.17: Graphical interpretation of the spatial correlation behavior at transmitter and receiver respectively.

TABLE 3.3: Fitting coefficients for spatial correlation matrix modeling at the transmitter $\mathbf{R}_{\mathrm{T}}$ and receiver $\mathbf{R}_{\mathrm{R}}$.

$a_{\mathbf{R_T}}$	$b_{\mathbf{R_T}}$	$a_{\mathbf{R}_{\mathbf{R}_\phi}}$	$b_{\mathbf{R}_{\mathbf{R}_\phi}}$	$a_{\mathbf{R}_{\mathbf{R}_\theta}}$	$b_{\mathbf{R}_{\mathbf{R}_\theta}}$
0.91	0.97	2.62	2.65	0.94	0.99

noted that in this case, being the antenna planar array deployed in the vertical plane, correlation is expected to behave differently among antenna elements placed in the same column of the planar array and antenna elements placed in different columns of the planar array. This is so because elevational angle spread has been measured (see [99]) to be much less than the azimuthal spread, therefore antenna elements within the same array column should have a higher correlation than those in different columns of the planar array. When estimating with the channel measurements the channel correlation at

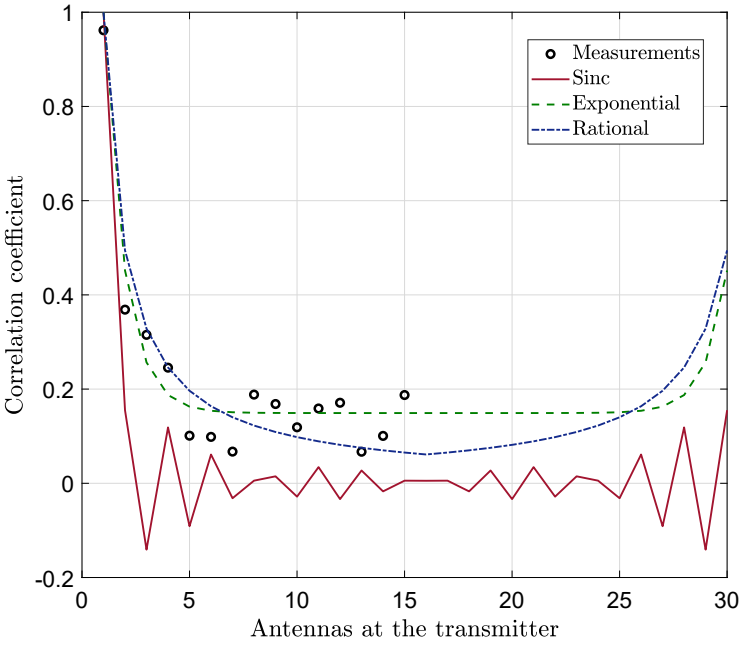

FIGURE 3.18: Measured correlation coefficients at transmitter versus fitted correlation coefficients (sinc, exponential and rational) at transmitter.

the receiver defined by (3.35), we also observe this symmetry behavior. Then, we provide different fits for the antenna elements deployed in the array columns (elevation) and in the array rows (azimuth). Again in both cases different correlation fitting functions have been tested ($\mathsf{sinc}\,(\cdot)$, $\mathsf{exp}\,(\cdot)$ and rational, see Fig. 3.19) and similarly to the transmit scenario the best fit both in azimuth (ϕ) and in elevation (θ) was obtained using rational functions, however with different parameters. Without loss of generality we number first the antenna elements in the first column of the array followed by the antenna elements placed in the second column as depicted in Fig. 3.17(b). In this scenario, the correlation matrix first row $r_{1k} = \frac{b_{\mathbf{R}_{\mathrm{R}_\theta}}}{a_{\mathbf{R}_{\mathrm{R}_\theta}}} \frac{a_{\mathbf{R}_{\mathrm{R}_\theta}}}{(k-1)+b_{\mathbf{R}_{\mathrm{R}_\theta}}}$ with $k = 1 \ldots 6$ and $r_{1k} = \frac{b_{\mathbf{R}_{\mathrm{R}_\phi}}}{a_{\mathbf{R}_{\mathrm{R}_\phi}}} \frac{a_{\mathbf{R}_{\mathrm{R}_\phi}}}{(k-N_v)+b_{\mathbf{R}_{\mathrm{R}_\phi}}}$ with $k = 7 \ldots 12$. The best fit coefficients $a_{\mathbf{R}_{\mathrm{R}_\phi}}$, $b_{\mathbf{R}_{\mathrm{R}_\phi}}$, $a_{\mathbf{R}_{\mathrm{R}_\theta}}$ and $b_{\mathbf{R}_{\mathrm{R}_\theta}}$ are given in Table 3.3. It is straightforward to build the correlation matrix with the correlation coefficients of the first row, taking into account the numbering used in the planar array and the relative position between antenna elements.

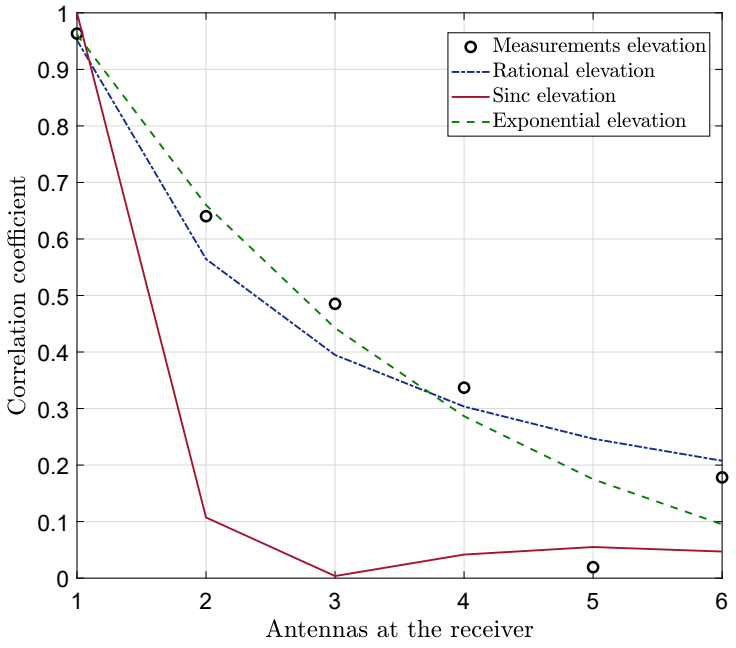

(a) Correlation at the receiver in elevation.

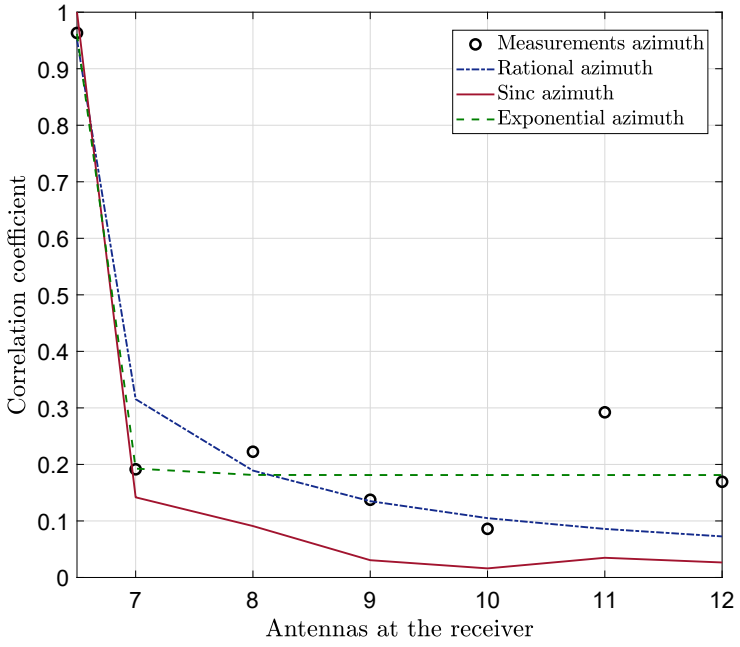

(b) Correlation at the receiver in azimuth.

FIGURE 3.19: Measured correlation coefficients at receiver vs fitted correlation coefficients (sinc, exponential and rational) at receiver: (a) Elevation (b) Azimuth.

3.5 Empirical evaluation of the achievable rates

The main objective of this section consist of analyzing the performance of the textile multi–antenna terminal in terms of achievable rates based on the normalized measured channel realizations, as well as on channel realizations synthetically generated using the statistical models derived in Section 3.4. To perform it, the MIMO achievable rate concept is briefly explored from a theoretical point of view taking into consideration the different transmission strategies that might be available. Then, the empirical results are presented and analyzed.

3.5.1 Achievable rates of MIMO systems

As it is well–known, the great benefit of MIMO systems over SISO consists of significantly improving the spectral efficiency of any communication system without increasing neither the transmitted power nor the bandwidth. The researches performed by Foschini [100], Winters [101] and Telatar [102] in the field of information theory opened a research area that is still growing. Concretely, it was Telatar [102] in the 90s who proposed the expressions of the capacity for MIMO systems equivalent to the expressions previously proposed by Shannon for SISO channels [103]. These expressions promise high spectral efficiency that increases linearly with the number of antennas [104, 105].

Attending to the specific case that is being handled in this Thesis, the system achievable rates depend on the normalized narrow–band small–scale fading $N \times M$ channel matrix $\mathbf{H}_{\text{norm}}$ (as in (3.22)) and on the received Signal–to–Noise ratio. Additionally, if precoding at the transmitter is used to overcome spatial interference, the achievable rate (in bits/s/Hz), for Gaussian input signal is given by [106]:

$$R = \log_2 \det \left(\mathbf{I}_N + \frac{\mathsf{SNR}}{\mathrm{Tr}\left\{\mathbf{Q}\right\}} \mathbf{H}_{\text{norm}} \mathbf{Q} \mathbf{H}_{\text{norm}}{}^{\dagger} \right), \tag{3.36}$$

where $\mathbf{I}_N$ is the $N \times N$ identity matrix, $\mathbf{Q}$ denotes the input covariance matrix chosen depending on the implemented precoding strategy and $\mathrm{Tr}\left\{\cdot\right\}$ is the trace operation.

In this Thesis we address two different transmission strategies, each of them characterized by different level of channel information (CSI) available at the transmitter:

- *Optimal precoder with CSI at the transmitter (CSIT)*: the transmitter needs to accurately track the instantaneous CSI ($\mathbf{H}_{\text{norm}}$), which may be feasible with the system working in Time Division Duplexing (TDD). It requires a matrix decomposition computation for every channel use since the precoder would instantaneously diagonalize the channel matrix and its squared singular values are given by the optimal water-filling (WF) power allocation [107]. Then $\mathbf{Q} = \mathbf{U}\Lambda\mathbf{U}^{\dagger}$, where $\mathbf{U}$ are the eigenvectors of $\mathbf{H}_{\text{norm}}^{\dagger}\mathbf{H}_{\text{norm}}$, and Λ is obtained from the classical WF power allocation algorithm.

- *Optimal precoder with no CSI at the transmitter (No–CSIT)*: the precoder does not perform any processing since it does not have any information about the channel, in which case $\mathbf{Q}$ is set equal to the identity matrix.

The achievable rate expression defined in (3.36) shows an upper limit subject to ideal operating conditions, mainly related to the correlation presented between the different subchannels of the MIMO system. There are different factors that may lead to not ideal conditions, among them we can highlight low scattering environments, the existence of LOS conditions, the antenna characteristics, etc. The influence of these factors usually results in an increase in the spatial correlation between the subchannels of the MIMO system, decreasing in this way the rank of the impulse response matrix and consequently the performance of the channel suffers a significant degradation. There are several authors [108, 109] that have shown this performance degradation in presence of spatial correlation and although the capacity still grows linearly with the SNR, when it is high, the scaling factor is lower than in the ideal uncorrelated case [108]. On the other hand, sometimes although the propagation environment is rich in scattering and low or null spatial correlation is presented, some phenomena which reduce the channel matrix rank occurs. These phenomena known as Keyhole or pinhole have been studied by different authors [94, 110]. They usually appear in situations where transmitter and receiver are very far apart or in situations in which propagation between transmitter and receiver occurs through effects such as diffractions or propagation by waveguide. Representative propagation environments for this second situation are corridors and tunnels [110].

In the next subsection, the performance of the textile multi–antenna terminal in the aforementioned O2I propagation environments will be evaluated. Moreover, the impact

that several factors (e.g. antennas configuration, spatial correlation or normalization) have in this performance will be analyzed.

3.5.2 Experimental results

In this subsection we evaluate the empirical achievable rates R of a relevant O2I scenario where the user is equipped with the wearable multi-antenna terminal and positioned indoors in an underground location. The performance of CSIT and No–CSIT is studied based on (3.36) using the measured channel matrices. The empirical achievable rates are compared with the results obtained with the model in (3.12) using synthetic channel samples with parameters estimated from our data as described in Section 3.4. The standard procedure of normalization of gain matrices by the Frobenius norm [73] was used to allow setting a SNR that is not affected by scale factors in the measurements or in the simulation. We define for our comparison $\mathsf{SNR}_{\text{ref}}$ as the average value of SNR in a region subject to random (zero–mean) shadow fading, i.e. the value after eliminating shadow fade variations. In the case of the empirical data, the distance–dependent path–loss is removed using the linear regression discussed in Section 3.4.2. This assumes that BS power control compensates for large–scale and path–loss variation due to changes in distance between base and user, but not for per–instantiation SNR variations due to shadowing. Then, the performance in terms of achievable rates is given not only by the multipath richness but also by the $\mathsf{SNR}_{\text{ref}}$ influence.

For the synthetic rates 3000 complex Gaussian matrices were generated to simulate the diffuse components and in the case of the Rician model, the specular component was generated as an all–ones deterministic matrix [111]. The spatial correlation matrices for the channel synthetic data correspond to the models described in Sec. 3.4.3.2. The shadow fades follow the Log–Normal fitted model described in Sec. 3.4.2, therefore also for the synthetic data, SNR accounts for random shadow fading with $\mathsf{SNR}_{\text{ref}}$ as its average value. For reference we also plot the results for simulated Rayleigh i.i.d. matrices.

We present the achievable rates for different antenna deployments at the transmitter $M = \{2, 4, 12, 30\}$ and $\mathsf{SNR}_{\text{ref}}(\text{dB}) = \{0, 15\}$. The first two scenarios $M = \{2, 4\}$ corresponds to realistic current communication scenarios, where the BS are still equipped with small number of antennas. The large antenna deployments $M = \{12, 30\}$ accounts

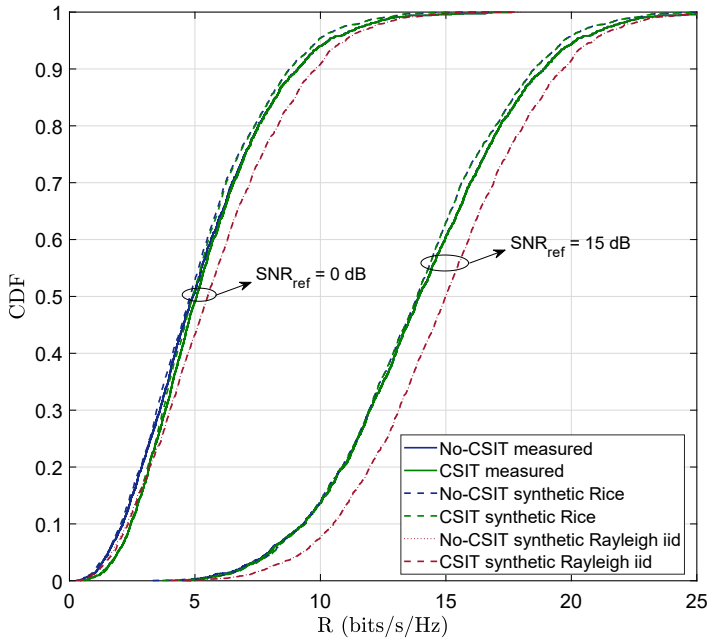

(a) Empirical and synthetic R for $M = 2$, $N = 12$ and $\mathsf{SNR}_{\text{ref}}(\text{dB}) = \{0, 15\}$.

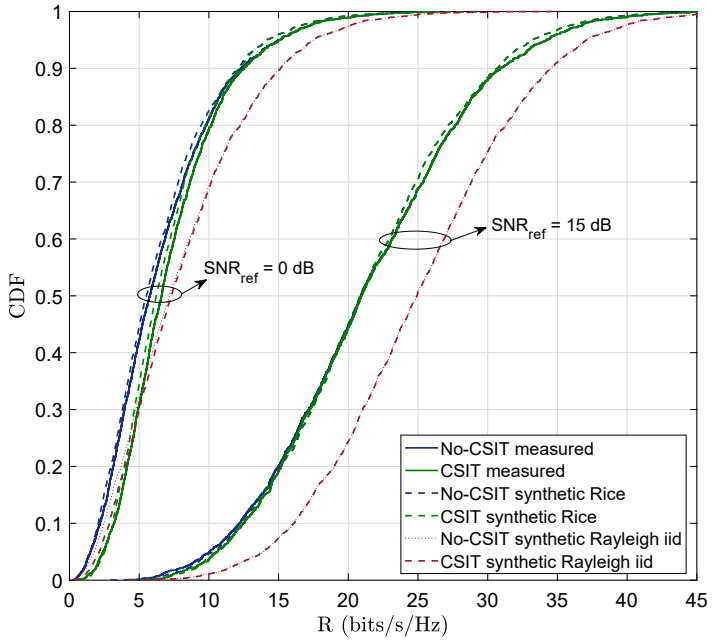

(b) Empirical and synthetic R for $M = 4$, $N = 12$ and $\mathsf{SNR}_{\text{ref}}(\text{dB}) = \{0, 15\}$.

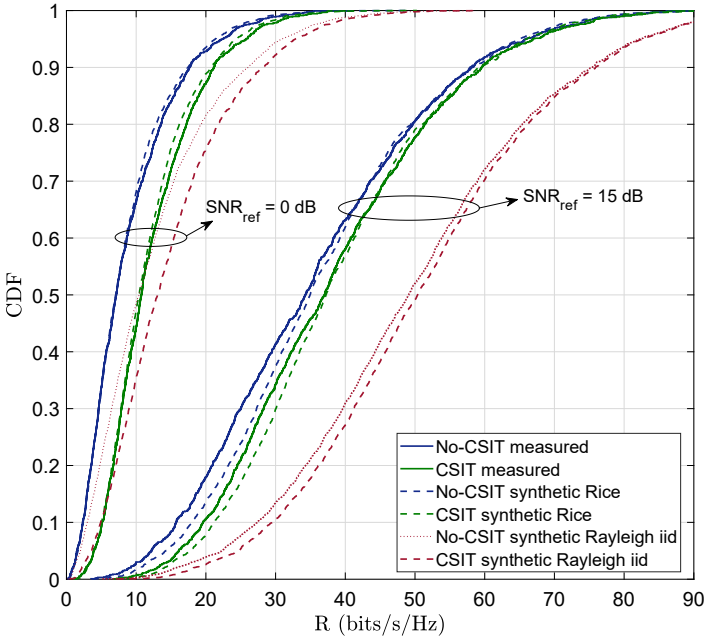

(c) Empirical and synthetic R for $M = 12$, $N = 12$ and $\mathsf{SNR}_{\text{ref}}(\text{dB}) = \{0, 15\}$.

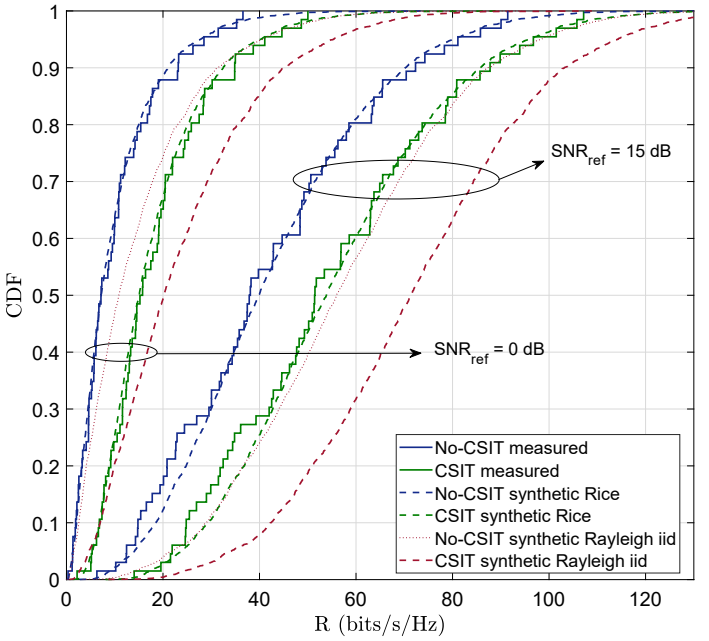

(d) Empirical and synthetic R for $M = 30$, $N = 12$ and $\mathsf{SNR}_{\text{ref}}(\text{dB}) = \{0, 15\}$.

FIGURE 3.20: Achievable rates obtained from the measurement campaign and comparison with Rayleigh iid and correlated Rice channel samples synthetically generated. Different antenna deployments are studied in the BS $M = \{2, 4, 12, 30\}$ and an array of $N = 12$ textile antennas is placed at the user end.

for more futuristic 5G scenarios, where much higher rates may be achieved enabling novel communication capabilities such as, high-resolution images, thermal vision, augmented and/or virtual reality and cognition, all candidates for future emergency systems.

Figure 3.20 shows that using the enhanced multi–antenna UE in the tested O2I propagation scenarios, at high SNR, we can achieve significant increases in data rates. As expected, as the number of antennas increases the spectral efficiency also increases, confirming the expected MIMO gains. Similarly, for high SNR and large number of antennas ($M = \{4, 12, 30\}$) we observe how CSIT outperforms the scenarios where CSI is not available at the transmitter.

Also, the rates obtained from these synthetic channel realizations are seen to match the empirical results very well (see Fig. 3.20). The predicted spectral efficiencies for the Rayleigh model are as expected the highest, illustrating that even in this heavily obstructed scenario such a model is overly optimistic.

3.5.2.1 Impact of different BS configurations on the empirical results

Since MIMO gains are strongly dependent on the lowest number of transmit or receive antennas, the impact of increasing the number of antennas at the BS when the number of antennas at the textile multi-antenna terminal is fixed to $N = 12$ is evaluated.

In Fig. 3.21 we provide the achievable rates averaged on the channel realizations for the measured channel data and for the Ricean synthetic data following the correlation models in Sec. 3.4.3.2. It is clearly appreciated the saturation effect with almost no additional rate gains for M greater than 20 in both cases. This behavior can be explained by the fact that the measured channel realizations are not Gaussian i.i.d. In addition, it is well–known [109] that Ricean distribution significantly limits the linear growth in spatial multiplexing gain. Moreover, it should be remarked that this behavior is independent of the transmission strategy employed, CSIT or No–CSIT. As expected, when channel knowledge is available at transmitter the achievable rates are higher than when is not available.

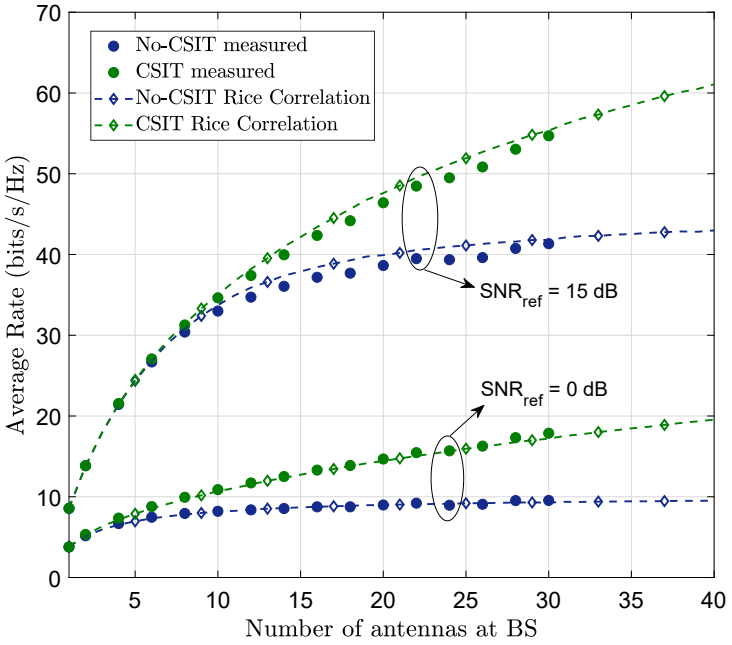

FIGURE 3.21: Comparison of average rates between the measured channel coefficients and synthetic Ricean coefficients with correlation when increasing the number of antennas at the BS with $\mathsf{SNR}_{\text{ref}}(\text{dB}) = \{0, 15\}$.

3.5.2.2 Impact of correlation on the empirical results

As discussed earlier in this chapter, spatial correlation plays an important role when referring to achievable rates of MIMO systems. Below, we compare the achievable rates reached by the measured channel realizations (correlated) and for Ricean synthetic data forcing no correlation, i.e. $\mathbf{R}_{\text{T}} = \mathbf{I}_M$ and $\mathbf{R}_{\text{R}} = \mathbf{I}_N$.

In Fig. 3.22 the average rates presented for synthetic data forcing the samples to be uncorrelated, illustrate the relevance of correlation in MIMO performance [109]. Differences from 2.8 bits/s/Hz to 13.7 bits/s/Hz and from 3.1 bits/s/Hz to 12.9 bits/s/Hz are appreciated for CSIT and No–CSIT transmission strategies respectively depending on the available SNR and with $M = 20$ dB. It is also well–known that for the transmission strategies that are being considered, when the channel is uncorrelated, both strategies perform significantly better than when there is correlation (see Fig. 3.21).

Fig. 3.23 shows how the presence of correlation modifies the distribution of the eigenvalues of the channel realizations, increasing the dispersion among them and making the power gain of the generated subchannels smaller, thus the number of significant subchannels usually tends to be reduced. Then, it is verified that including the correlation

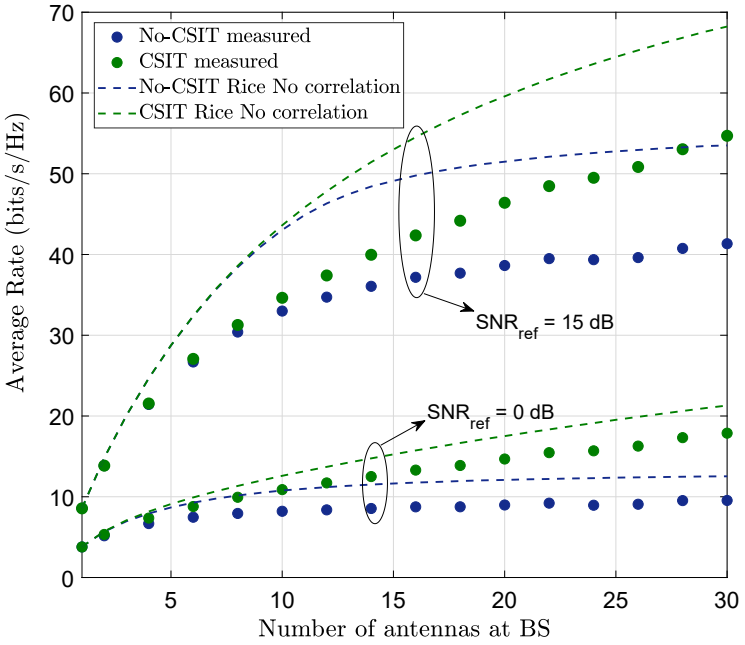

FIGURE 3.22: Comparison of average rates between the measured channel coefficients and synthetic Ricean coefficients without correlation when increasing the number of antennas at the BS with $\mathsf{SNR}_{\text{ref}}(\text{dB}) = \{0, 15\}$.

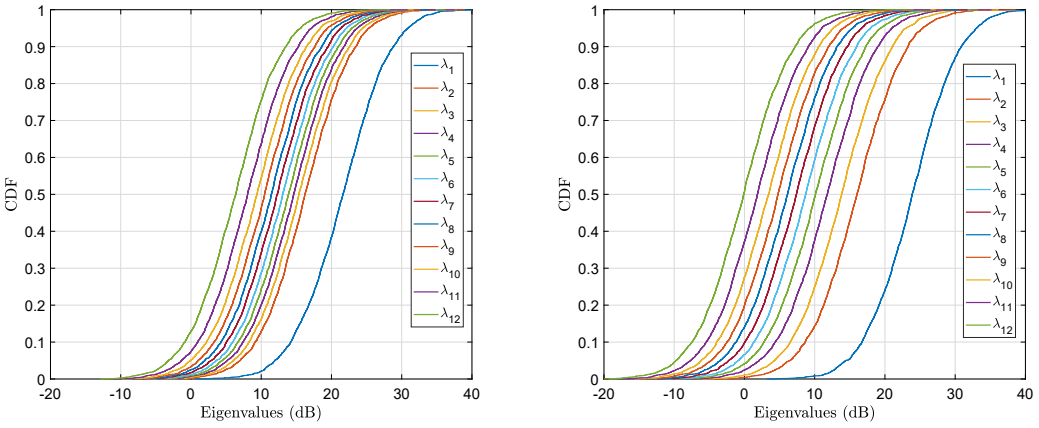

(a) Without correlation.

(b) With correlation.

FIGURE 3.23: Eigenvalues of 12×30 channel realizations based on simulation model (3.12) using parameters estimated from our data as described in Section 3.4 generated (a) without correlation and (b) with the correlation model defined in Section 3.4.3.2.

in the generation of synthetic channel samples it is of high relevance for an accurate match to the measured rates.

3.5.2.3 Impact of normalization on the empirical results

As it was mentioned above, selecting the appropriate normalization procedure is of high relevance with regard to the system performance. In particular, in this Thesis the normalization procedure presented in Subsection 3.4.1 was firstly employed. However, as it is shown in Fig. 3.24(a) some discrepancies between the performance reached with the measured data and the synthetic data were found, being especially appreciated in the tails of the CDFs. Indeed, the data synthetically generated do not properly describe the measured rates using that normalization procedure. Trying to look for a better match, we found that the SF factor is a crucial parameter of our O2I measured data that should not be disregarded if accurate performance results can be obtained. Additionally, as it is observed in Fig. 3.24(a) data rate values achieved with probabilities higher than 0.5 could be underestimated. Therefore, we added to the aforementioned normalization procedure the SF effect, reducing in this way the discrepances between the measured and synthetic results.

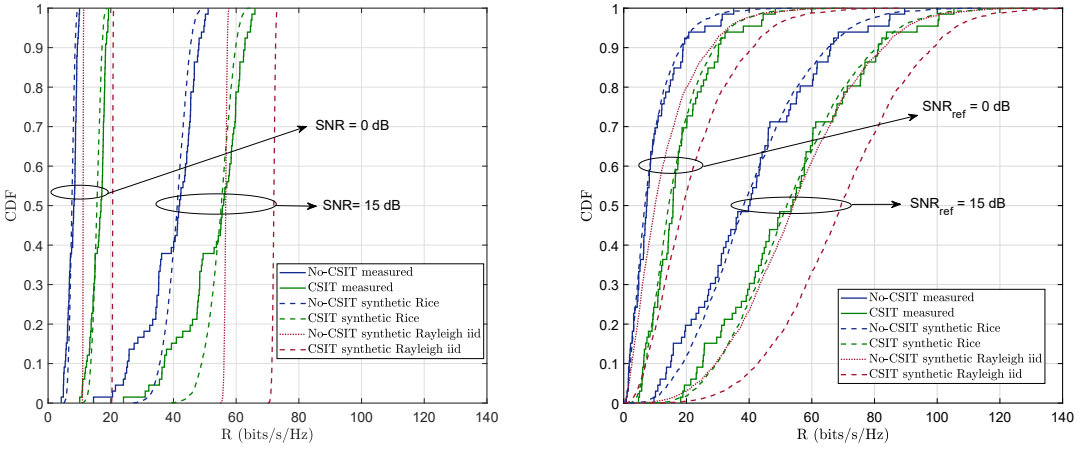

(a) Disregarding all the effects (G,PL and SF).

(b) Considering SF.

FIGURE 3.24: Normalization of 12×30 measured and synthetic channel realizations (a) Applying the normalization procedure presented in Subsection 3.4.1 (disregarding G, PL and SF) (b) Applying the normalization procedure presented in Subsection 3.4.1 with some nuances (considering SF) 3.4.3.2.

It seems clear that special attention should be paid to the specific behavior of the measured data and identify what parameters really define it and should not be dismissed by the normalization procedure since poorly estimations of the propagation environment could be obtained.

3.6 Conclusions

In this chapter, the performance of the textile multi–antenna terminal in terms of achievable rates has been empirically characterized using channel realizations measured in relevant O2I propagation environments from the reliable communications point of view. Different levels of channel knowledge at the transmitter (CSIT and No–CSIT) have been considered. In addition, these empirical rates have been compared with the ones achieved with synthetic channel samples that follow typical measured statistics such as Rayleigh or Rice. Among the main conclusions, we can highligth:

- The normalization of the channel matrices has a direct impact on performance of the system. Then, depending on the selected normalization procedure transmit power control should be taken into account or not.
- It has been demostrated that the achieved rates are consistenly lower than those obtained under the Rayleigh i.i.d. assumption, despite the fact this is a heavily obstructed NLOS scenario.
- As expected, it has been corroborated that if only the number of antennas of one end is increased while the other is fixed, then the achieved rates tend to saturate.
- The correlation has a big impact in the achieved rates. No considering/modeling it in a proper way may inccur in inaccurate estimates of the achievable rates.

In spite of these conclusions, some of them directly extracted from the characteristics of particular O2I propagation scenarios, it is clear that the textile antenna array significantly improves spectral efficiency.

Chapter 4

Enabling Future Public Safety Communication Infrastructure

This chapter analyzes the use of textile multi–antenna terminals to improve public safety communications whose most important needs are reliable connectivity, coverage and enough throughput to transfer any content that may be helpful in disaster situations. In particular, it is proposed that the textile technology is used in a rapidly deployable LTE-based network architecture proposal that envisions a two–hop relay network that seeks to reach locations with low coverage corresponding typically with O2I propagation environments. Thus, this technological approach pretend to eliminate the weakness of current Private Mobile Radio (PMR) systems.

4.1 Introduction

In the last ten years, a total of 6.090 disasters have been reported coming from both, natural hazards (biological, geophysical, climatological, hydrological and meteorological) and technological hazards (industrial, transport and miscellaneous) [112]. This makes an average of 600 disasters per year all over the world. This amount of disasters has implied that in total, over the last decade, 771.911 people were deceased under those circumstances and those affected, defined as the population requiring immediate assistance such as rescuing, basic survival needs, medical assistance and also those reported

injured or homeless [113], are close to 200 million people every year as depicted in Fig. 4.1.

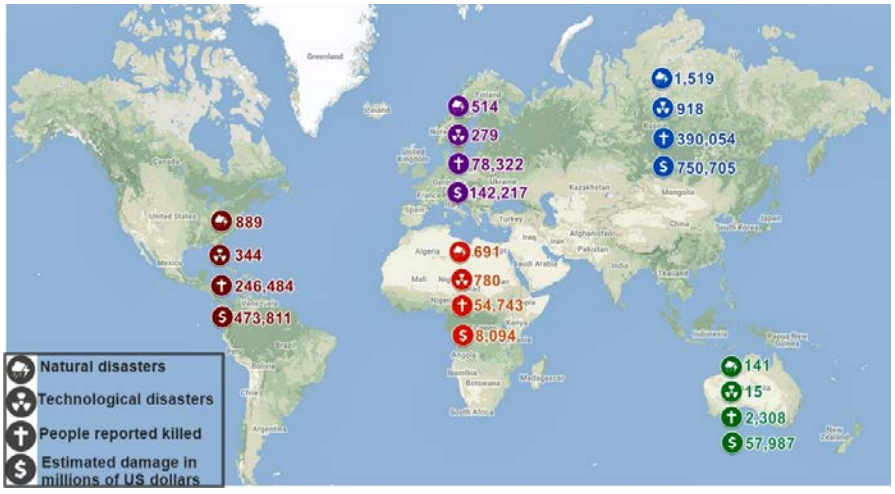

FIGURE 4.1: Disaster figures during the period of time from 2006 and 2015 per continent. Data collected from 2016 World Dissasters Red Cross report [112].

The type of the disaster and the data on the number of people affected are very useful information sources for disaster consciousness, for the definition of future strategies for lowering disaster impact and for the potential planning of a response. The reduction of disaster losses and disaster risk is the main goal of the Sendai Framework for Disaster Risk Reduction (DRR) 2015 – 2030 [114], proposing a broad approach focused on people and a change in emphasis from disaster management to disaster *risk* management. Many measures are to be addressed with this objective: structural, social, economic, educational, health, cultural, environmental, political, institutional and technological. However, even within this broad approach there is in most of the cases a first necessity for human intervention for emergency reaction after the disaster and this is where public protection, first responders and disaster relief personnel or emergency services come out. Concretely, Priority 4 "Enhancing disaster preparedness for effective response and to Build Back Better in recovery, rehabilitation and reconstruction" [114] copes with, among other, resilience of infrastructure, contingency programs, workforce training, disaster risk and emergency communications mechanisms, social technologies and hazard-monitoring telecommunications systems. Therefore, technology and, specially, communication and information systems are key tools that have always played and will play a very important role on disaster preparedness, managing and intervention [115–117].

A representative example in our everyday life are social networks, which have been a distributed source of information with the capacity of offering local access to information on site. For instance, Facebook and Twitter were used within the Ushahidi open–source crisis–mapping software in Haiti to collect data along with an SMS platform [118]. In addition, divers technologies are being explored in order to provide first responders with enhanced communication capabilities to overcome, resolve or alleviate emergency situations. In 2016, the application of wearable technology such as physiological sensors for health support among others, was one of the main programs for the U.S. Department of Homeland Security.

Hence, in view of the above the provision of decision making systems, early warning systems and real–time information acquisition systems are the main stakes to be addressed.

4.1.1 Legacy emergency systems vs future public safety networks

Novel trends in emergency communications to support first responders, disaster relief personnel and public protection [119] are underscoring the necessity of overriding legacy narrowband Private Mobile Radio (PMR) emergency systems such as the well–known Trans European Trunked Radio (TETRA). So far, critical communication systems have mainly been oriented to provide a rich set of voice-centric services (i.e. group call, direct mode or push-to-talk communications) [120].

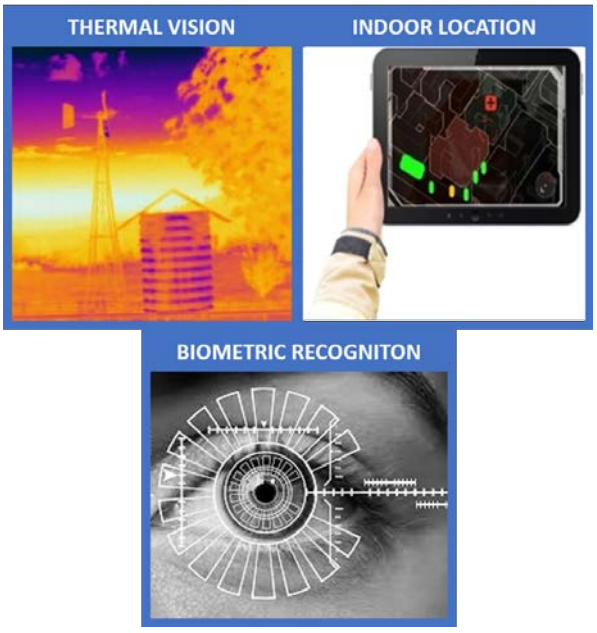

FIGURE 4.2: Examples of useful multimedia services during emergency interventions.

Additionally, in the past few years, also the first responder emergency groups have claimed that, to improve their success in solving any crisis, it would be very useful a seamless access to communication capabilities [121] such as, among others, biometric recognition, real–time thermal vision, augmented and/or virtual reality and cognition, video transmission, access remote databases or real-time high resolution maps. Indeed, multimedia data services based on broadband communication with extremely high reliability could produce a radical change in the outcome of any first responder intervention clearly implying a paradigm shift in emergency scenarios, moving from a voice-commanded to an image-commanded interaction with possibly augmented information backhaul support (see Fig. 4.2). Network solutions within immediate future wireless communication systems (LTE, LTE advanced-pro, 5G) are defining a novel portfolio of capabilities in order to make mobile networks capable of conveying critical communication services [122, 123]. Specifically, some of the key requirements that this portfolio of capabilities pretends to address go from reliable connectivity, availability, security, coverage, to high throughput (downlink and uplink) among others.

4.2 A Technological Solution to Support Future Emergency Networks

Disaster scenarios are particularly challenging and fully heterogeneous. Challenges include a communication infrastructure that may not be available, an extremely limited wireless coverage in specific emergency scenarios, such as garages, tunnels, etc. or not enough bandwidth to provide the aforementioned multimedia services. Among the novel portfolio of capabilities previously mentioned, future wireless technologies have widened the range of frequency bands to provide emergency services [124], allowing other bands usage and solving the propagation issue of very restricted frequency bands such as the exclusive 400 MHz or 700 MHz available for trunking services. Additionally, for full multimedia provision based on broadband transmission [125, 126], it is also necessary to deal with the user end point communication capabilities, in this case the first responder or rescuer, without compromising their seamless, lightweight and ultimately their portable features.

Hence, in view of the above, in this Thesis future wireless communication technologies are postulated as the choice for public safety broadband communication systems, examining the suitability of the different frequency bands, proposing network and physical layer solutions that seek to reliably reach locations with low or null coverage, all these to enable the provision of multimedia services. Such a solution is performed by combining some LTE-A features with the enhancement of the end user communication capabilities by means of large–scale MIMO technology. As it is shown in Fig. 4.3, we propose then an LTE-A network scenario, that could eventually consider a two–hop architecture based on relaying, to provide broadband service in scenarios with very low or null coverage, that are typically O2I propagation environments. It should be noted that a network architecture based on relay nodes allows for a rapidly deployable communication infrastructure anywhere and anytime. Furthermore, the relaying architecture will be further enhanced by providing the rescuer with wearable technology that implements a large number of antennas on the user side, overriding the typical scenario where the user equipment only possess one or at the most two antennas.

In summary, in the proposed network three main communication elements (BS, relay node (RN) and enhanced UE) and two main links can be distinguished. One of them

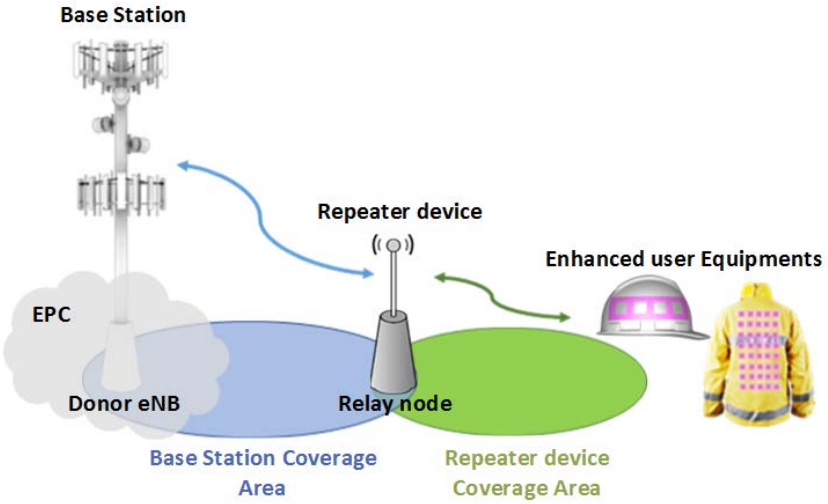

FIGURE 4.3: Architecture of the network proposal based on the 3GPP relay concept.

known as backhaul link is defined between the BS and the RN and gives rise to the base station coverage area, while the second one known as acces link defines the repeater device coverage area between the RN and the UE.

4.2.1 LTE network components and deployment

Donor eNB (DeNB) – Relay node: E-UTRAN supports relaying through a relay node wirelessly connected to an eNB or in other words to a BS, called Donor eNB [127] (see Fig. 4.3). This feature enables the coverage extension without the necessity of deploying a new fixed base station. The usage of these nodes is standardized from Release-10 of the LTE standard. Additionally, this feature is included in the scope of LTE-A (Release-10 and onwards).

Relay node – User Equipment: This feature provides the functionality to support connectivity to the network for remote UEs that are not "served by E-UTRAN". The standardization of this feature started in Release-12, and still continues in Release-13 [123].

Therefore, considering that the above features could improve the performance of public safety networks, now it is necessary to define the operation model. If we focus on the fire department case, one possible solution that we envisage is as follows. We propose that the fire truck has a relay node mounted on-board. Hence, focusing on coverage issues in garages or basements, the fire truck may park strategically to improve the

MIMO-relaying performance (required rates and coverage). On the other hand, one of the emergency staff members may wear a user equipment capable of acting as bridge. This UE would be connected to the Evolved Packet Core (EPC) via the Relay Node and would improve the communication capabilities of the staff members located deeper inside the garage or basement. In Fig. 4.4 an example of a temporary deployment for different emergency brigades is shown.

FIGURE 4.4: Example of temporary deployment for fire and medical brigades. Relay node mounted on the respective vehicles and textile antenna array deployed at the backside of the rescuers' jacket.

4.2.1.1 Relay node

In order to seek a deeper understanding of the relay technology defined in the LTE-A standard, we next cite and define the different categories in which relay nodes can be classified attending to different criteria such as their use of the spectrum [128], the level of the protocol stack in which the user traffic is transmitted and the functions enabled in the control plane [129] or the transparency they present regarding to the user [130].

- Spectrum use: Two types of relays can be distinguished depending on the use of the spectrum in the different links: in–band and out–of–band. In the first case, the link between the base station and the relay shares the same frequency as the link between the relay and the UE. On the other case, the link between the BS and the RN does not share the same frequency as the link between the RN and the UE.

- Transparency: The main difference between non–transparent and transparent operation modes lies in how framing information is transmitted. In non-transparent mode, the relay nodes transmit frame header information mainly containing scheduling information that it is useful for the nodes to know when they can transmit and receive information. Conversely, in transparent operation mode relay nodes do not transmit frame header information.

- Level in the protocol stack: Layer 1, 2 and 3 relay nodes can be distinguished in this category. Layer 1 relays (also known as repeaters) act amplifying and forwarding the downlink and uplink signals between the BS and the UE, just like a simple analog amplifier. Then, it is possible to extend the coverage area of an existing base station to locations where it cannot reach by itself. It should be noted that Layer 1 relays work in a non-transparent mode and typically the noise from the link between the base station and the relay is amplified in the next link. Regarding, layer 2 and 3 relays essentially decode the incoming signal and re-modulate and re-encode it before the amplified version is forwarded. These types of relays avoid drawbacks such us noise being amplified and re-transmitted. The main difference between layer 2 and 3 relays resides in the fact that the last type performs some processing (i.e. ciphering, data segmentation/concatenation/reassembly) before re–modulate and re–encode the signal again.

From now on, attending to the protocol stack classification we will assume an amplify–and–forward (AF) relay scenario.

4.2.2 Textile multi-antenna terminals (UE)

To enable high spectral efficiency necessities of current public safety networks, the textile antenna technology, which allows us to deploy MIMO–based personal area networks in the proximity of the human body, appears to be a promising solution due to the physical layer improvement it offers [7]. As mentioned previously, the main idea behind this technology consists of embedding a large textile antenna array which acts as a transmitter/receiver at the user's garments, bringing the benefits of massive MIMO directly to the user's end.

In the following sections, two different multi–antenna terminal designs are considered. One of them consists of an 8×5 textile planar array deployed in the backside of a jacket and whose main characteristics are described in [7, 131] and summarized in Table 4.1. The other design considered below is the 1×4 textile array design to be conformed on a safety helmet working at 4.9 GHz and whose main features were described in Chapter 2.

TABLE 4.1: Design features of the planar textile antenna array deployed at the backside of a jacket.

Working Frequency	2.5 GHz
Planar array size	8×5
Inter–element distance	0.66λ
Dielectric substrate	Common felt
Metallization	Electrotextile material
Total array perimeter	2104 mm
Backward power levels	-20 dB
Bandwidth	70 MHz

Finally, it is worth noting that the central frequencies used by the aforementioned textile multi–antenna terminals could be valid for a real implementation of the technological proposal presented in this chapter. The textile terminal working at 2.5 GHz would cover LTE bands 7 and 41 operating in FDD and TDD modes respectively [132]. On the other hand, the textile terminal working at 4.9 GHz would cover the current public safety frequency band [133] in United States.

4.3 MIMO-Relaying Scenario Modeling

Focusing in the uplink, a two–hop single relay scenario with multiple antennas at the source/UE (M), relay node (W) and destination/BS (N) working in an amplify–and–forward mode (Layer 1 relay) is analyzed. The relay node is assumed to work in half–duplex mode. This means that communication from source to relay and from relay to destination is performed in two different time slots. Additionally, it is assumed that there is no direct link between the source and destination. The system model architecture is depicted in Fig. 4.5.

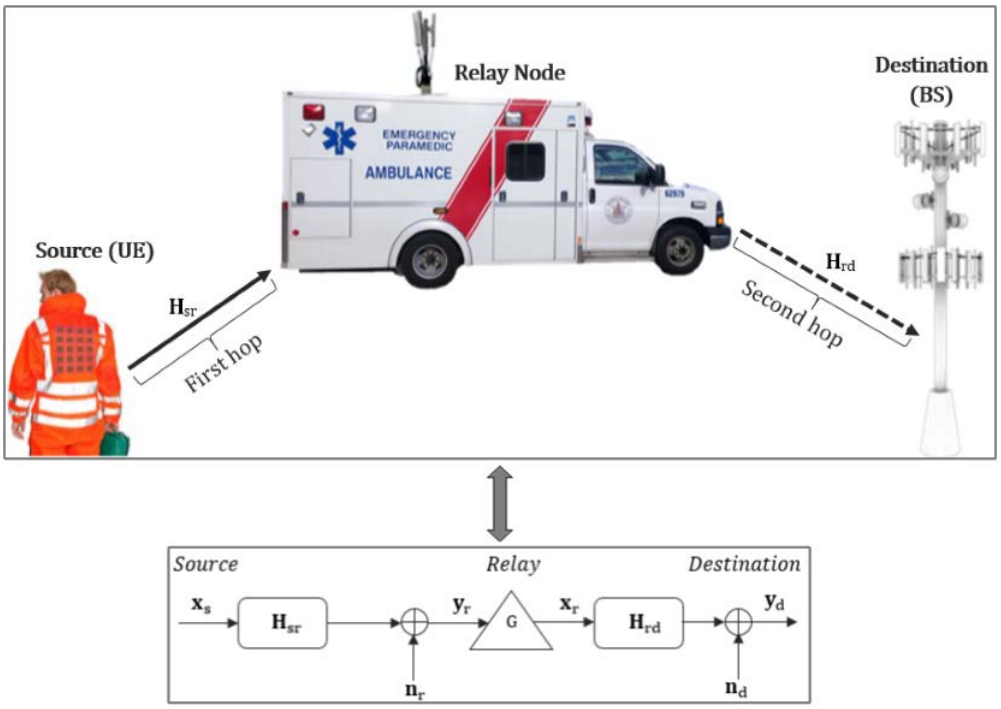

FIGURE 4.5: System model of a two–hop half–duplex single relay scenario working in the uplink.

During the first time slot, the transmitted signal from the source propagates through the first–hop channel, and the received signal at the relay is given by

$$\mathbf{y}_r = \sqrt{\mathsf{SNR}_{sr}}\mathbf{H}_{sr}\mathbf{x}_s + \mathbf{n}_r \tag{4.1}$$

where $\mathbf{x}_s$ is the $M \times 1$ transmitted signal vector with normalized power, $\mathbf{H}_{sr}$ is the $W \times M$ channel matrix between the source and the relay, SNR_{sr} is the SNR of the source–relay link and $\mathbf{n}_r$ is the $W \times 1$ relay noise vector with normalized variance.

During the second time slot, the relay amplifies the received signal defined in (4.1) and forwards it to the destination. The received signal at the UE is as follows:

$$\mathbf{y}_{\mathrm{d}} = \sqrt{\mathsf{SNR}_{\mathrm{rd}}}\mathbf{H}_{\mathrm{rd}}\mathbf{F}\mathbf{H}_{\mathrm{sr}}\mathbf{x}_{\mathrm{s}} + \begin{bmatrix}\sqrt{\mathsf{SNR}_{\mathrm{rd}}}\mathbf{H}_{\mathrm{rd}}\mathbf{F} & \mathbf{I}\end{bmatrix}\begin{bmatrix}\mathbf{n}_{\mathrm{r}} \\ \mathbf{n}_{\mathrm{d}}\end{bmatrix} \tag{4.2}$$

where $\mathbf{H}_{\mathrm{rd}}$ is the $N \times W$ channel matrix between the relay and the destination, $\mathbf{F}$ is the $W \times W$ relay amplification factor, $\mathsf{SNR}_{\mathrm{rd}}$ is the relay–destination link SNR and $\mathbf{n}_{\mathrm{d}}$ is the $N \times 1$ destination noise vector with normalized variance.

4.3.1 Channel Model

In our analysis, the first hop channel $\mathbf{H}_{\mathrm{sr}}$ defined between the UE equipped with MIMO textile technology and the relay node, is modeled to take into account the textile antenna parameters and radiation patterns in transmission and reception and the surrounding scattering environment. Each element h_{wm} in the channel matrix $\mathbf{H}_{\mathrm{sr}}$ is described by the Green's function sampled at the position of the w-th receiving antenna $\mathbf{p}'_w$ given that the point source is located at the m-th transmitting antenna ($\mathbf{p}_m$) [134]:

$$\begin{aligned} h_{wm} = \int\int & \mathcal{G}_m(\theta,\phi)\mathcal{G}'_w(\theta',\phi')S(\mathbf{k}'(\theta',\phi'),\mathbf{k}(\theta,\phi)) \\ & e^{-j\mathbf{k}(\theta,\phi)\mathbf{p}_m}e^{j\mathbf{k}'(\theta',\phi')\mathbf{p}'_w}d\mathbf{k}'(\theta',\phi')d\mathbf{k}(\theta,\phi) \end{aligned} \tag{4.3}$$

where $\mathcal{G}_m(\theta,\phi)$ and $\mathcal{G}'_w(\theta',\phi')$ represent the radiation patterns in azimuth (ϕ) and elevation (θ) at the transmitter and receiver, respectively, $\mathbf{k}(\theta,\phi)$ and $\mathbf{k}'(\theta',\phi')$ are the wave vector space at the transmitter and receiver, respectively, and $S(\mathbf{k}'(\theta',\phi'),\mathbf{k}(\theta,\phi))$ is the channel scattering function, which relates the plane wave's emitting and receiving directions, $\mathbf{k}$ and $\mathbf{k}'$, respectively. It must be noticed that this channel model assumes single–polarized antennas as the ones described in Chapter 2 and therefore the transmit and receive vector fields, together with the channel scattering function can be considered scalars. However, this model could be easily extended to further consider different polarizations if we work with vectorial fields and a dyad transformation function as scattering [135, 136].

The vector space can be sampled into D plane waves at the transmitter and D' plane waves at the receiver to cover the entire space. Then, the channel matrix can be decomposed [137] into the product of five matrices as follows

$$\mathbf{H}_{\text{sr}} = \mathbf{B}_R^{\dagger} \Sigma_R \mathbf{H}_{\text{iid}} \Sigma_T \mathbf{B}_T \tag{4.4}$$

where $\mathbf{B}_R$ $(D' \times W)$ and $\mathbf{B}_T$ $(D \times M)$ given by (4.5) and (4.6) are the beamforming matrices depending on the antenna geometry and radiation patterns, $\mathbf{H}_{\text{iid}}$ $(D' \times D)$ is a complex Gaussian random matrix with i.i.d. components and variance one, and Σ_R and Σ_T are normalized diagonal matrices whose main diagonal is shaped with the corresponding angular power spectra. It should be noticed that the term $\mathbf{B}_R^{\dagger}\Sigma_R$ models the correlation at the transmitter, while the term $\Sigma_T \mathbf{B}_T$ models the correlation at the receiver.

$$\mathbf{B}_T = \begin{bmatrix} \mathcal{G}_1(\theta_1, \phi_1) e^{-j\mathbf{k}_1 \cdot \mathbf{p}_1} & \dots & \mathcal{G}_M(\theta_D, \phi_D) e^{-j\mathbf{k}_1 \cdot \mathbf{p}_M} \\ \vdots & \ddots & \vdots \\ \mathcal{G}_1(\theta_1, \phi_1) e^{-j\mathbf{k}_D \cdot \mathbf{p}_1} & \dots & \mathcal{G}_M(\theta_D, \phi_D) e^{-j\mathbf{k}_D \cdot \mathbf{p}_M} \end{bmatrix} \tag{4.5}$$

$$\mathbf{B}_R = \begin{bmatrix} \mathcal{G}_1(\theta'_1, \phi'_1) e^{j\mathbf{k}'_1 \cdot \mathbf{p}'_1} & \dots & \mathcal{G}_1(\theta'_D, \phi'_D) e^{j\mathbf{k}'_D \cdot \mathbf{p}'_1} \\ \vdots & \ddots & \vdots \\ \mathcal{G}_W(\theta'_1, \phi'_1) e^{j\mathbf{k}'_1 \cdot \mathbf{p}'_W} & \dots & \mathcal{G}_W(\theta'_D, \phi'_D) e^{j\mathbf{k}'_D \cdot \mathbf{p}'_W} \end{bmatrix} \tag{4.6}$$

The MC between antenna elements in transmission and reception is then captured via the coupling matrices $\mathbf{C}_T$ $(M \times M)$ and $\mathbf{C}_R$ $(W \times W)$. The resulting channel matrix is given by

$$\mathbf{H}_{\text{sr}} = \mathbf{C}_R \mathbf{B}_R^{\dagger} \Sigma_R^{1/2} \mathbf{H}_{\text{iid}} \Sigma_T^{1/2} \mathbf{B}_T \mathbf{C}_T \tag{4.7}$$

On the other hand, the second hop channel $\mathbf{H}_{\text{rd}}$, is modeled by a Rayleigh i.i.d. fading distribution, assuming a full–scattering environment and large spacing among antennas at both, the relay and the BS.

4.3.2 Relay amplification factor

We assume that the relay node simply applies a linear transformation on the received signal $\mathbf{y}_{\mathrm{r}}$ by means of the relay amplification factor $\mathbf{F}$ defined as follows:

$$\mathbf{F} = \beta \mathbf{I}_W \tag{4.8}$$

Parameter β is defined in order to achieve the relay–destination link $\mathsf{SNR}_{\mathrm{rd}}$ [138, 139], that enables to reach a certain power level that we would like it to be constant in the whole link. This will be particularly true if considering the same power level in both links, then from now we assume that the power employed by the source to transmit $\mathbf{x}_{\mathrm{s}}$ (P_T^{UE}) and the power employed by the relay node to transmit $\mathbf{y}_{\mathrm{r}}$ (P_T^{RN}) are equal to 1. Taking this into account, then β has to ensure that:

$$\mathbb{E}\left[\beta^2 \mathbf{y}_{\mathrm{r}}^{\dagger} \mathbf{y}_{\mathrm{r}}\right] = \beta^2 \left(\mathsf{SNR}_{\mathrm{sr}} \left\|\mathbf{H}_{\mathrm{sr}}\right\|_F^2 + 1\right) = 1 \tag{4.9}$$

then β is given by

$$\beta = \sqrt{\frac{1}{\mathsf{SNR}_{\mathrm{sr}} \left\|\mathbf{H}_{\mathrm{sr}}\right\|_F^2 + 1}} \tag{4.10}$$

It should be remarked, that in our model the power is assumed to be allocated uniformly over all the antennas.

4.4 Validation of the proposed network deployment

In this section, as a proof of concept the performance of the proposed technological solution that combines textile multi-antenna terminals and relaying architectures is validated. On the one hand, paying attention only to the UE-(RN/BS) link, the spectral efficiency gains as well as the power gains, both arisen from the use of the textile multi–antenna UE are evaluated. On the other hand, the optimal location of the relay node is found attending to the requirement of a reliable connectivity.

4.4.1 High speed connectivity

LTE-A allows 8×8 MIMO implementations in the downlink (i.e. 8 antennas in the BS and 8 antennas in the UE) and 4×4 MIMO in the uplink (i.e. 4 antennas in the UE and 4 antennas in the BS). In this section, the uplink throughput requirement is evaluated to show the benefits derived from the usage of the proposed textile multi-antenna terminals (both, conformed in a helmet and deployed at the backside of a jacket). The focus is in the uplink, since undoubtedly it has the most restrictive performance, specifically, in the link between the UE and a MIMO–RN in communication scenarios with extremely reliable connectivity conditions requiring a two-hop architecture or between the UE and the multi–antenna BS for a one-hop architecture.

To obtain the uplink data rate gain, a metric is proposed, Δ_R, that allows us to measure the relative data rate gain when comparing a single–antenna UE whose propagation scenario is characterized by the channel matrix $\mathbf{H}_{W\times 1}$ with a multiple antenna UE using the channel $\mathbf{H}_{W\times M}$. The gain is computed by getting the enhanced UE throughput with respect to that obtained by a single-antenna UE when the transmitted power is the same and there is no channel knowledge available. The general expression is given by

$$\Delta_R\,[bits/s/Hz] = \log_2\left[\frac{\det\left(\mathbf{I}_W + \frac{\mathsf{SNR}}{M}\mathbf{H}_{W\times M}{\mathbf{H}_{W\times M}}^{\dagger}\right)}{\det\left(\mathbf{I}_W + \mathsf{SNR}\mathbf{H}_{W\times 1}{\mathbf{H}_{W\times 1}}^{\dagger}\right)}\right] \tag{4.11}$$

where SNR represents the total link the Signal–to–Noise ratio, $\mathbf{I}_W$ is the $W \times W$ identity matrix and $\mathbf{H}_{W\times M}$, $\mathbf{H}_{W\times 1}$ denote the narrowband MIMO $W \times M$ and SIMO $W \times 1$ channel matrices, respectively. It must be noticed that both channel matrices are generated following $\mathbf{H}_{sr}$ channel model in (4.7).

Then, based on the above metric the performance of the proposed textile multi–antenna terminals, both deployed in a helmet ($M = 4$) and in the backside of a jacket ($M = 40$) and when the BS/RN is integrated by $N/W = \{4, 8, 40\}$ antennas is evaluated. In should be remarked, that this evaluation scenario expands the typical LTE-advanced uplink MIMO scenario, where the BS would only have $N/W = 4$ antennas as mentioned at the beginning of this section. A total of 500 channel realizations are generated based on the channel model described in Section 4.3 and the antenna design parameters obtained in Chapter 2 and in [140]. Specifically, for the beamforming matrix, $\mathbf{B}_T$, corresponding to the UE side where the textile antenna array is deployed, the geometry assumes an inter-element distance of ($\approx 0.6\lambda$ for the helmet UE and 0.66λ for the jacket UE) to define the antenna positions $\mathbf{p}_m$, and the simulated radiation patterns are used for $\mathcal{G}_m(\theta, \phi)$. Concerning the mutual coupling, despite it could have been neglected, the values obtained around -19 dB for the helmet UE and -20 dB for the jacket are considered. Finally, to characterize the scattering function at the transmitter side, full angular dispersion that is uniformly modeled is assumed. At the BS/RN side for simplicity, ideal antennas without mutual coupling and omnidirectional radiation patterns are considered. Regarding the characterization of the scattering function at the receiver side, it is taken into consideration that the angular spread may be smaller than at the transmitter side. Then, it is assumed negligible angular spread in elevation and a narrow angular spread in azimuth of approximately 30°, trying to get a worst case performance. To define the receiving antenna positions $\mathbf{p}'_w$, a linear array integrated by W antennas with inter-element distance of $\lambda/2$ is considered.

In order to study the data rate gains obtained when using one single antenna ($M = 1$) or several antennas ($M > 1$) in the UE, we apply (4.11) with $\mathbf{H}_{W\times M}$ and $\mathbf{H}_{W\times 1}$ generated following the aforementioned procedure. In Fig. 4.6, the complementary cumulative distribution function (CCDF) of the data rate gains assuming a specific SNR value of 15 dB is provided. In this scenario, for 50% of the channel realizations, we can get up rate gains from 8 bits/s/Hz up to 21.5 bits/s/Hz or from 11.5 bits/s/Hz up to 123 bits/s/Hz depending on the employed textile multi–antenna terminal (helmet or jacket) and the number of antennas deployed at the BS/RN with respect to the corresponding SIMO scenario. These data rate gains along with the available bandwidth may lead to improve emergency communications allowing the provision of high throughput multimedia services. For instance, if the available bandwidth is 20 MHz, since the reached gains

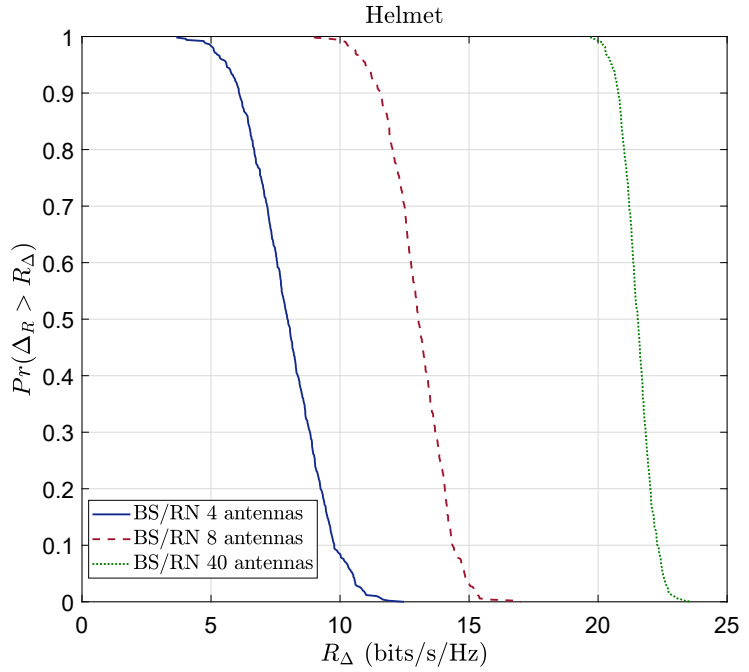

(a) 1×4 textile antenna array integrated in a helmet

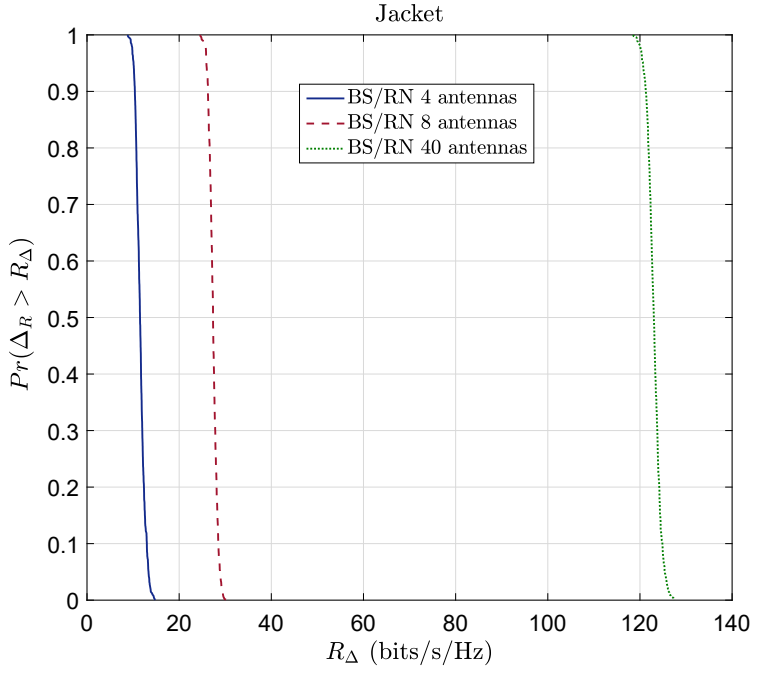

(b) 8×5 textile antenna array integrated in the backside of a jacket

FIGURE 4.6: CCDF of the relative data rate gain for the helmet and the jacket textile multi–antenna terminals according to different antenna configurations available at the BS/RN $= \{4, 8, 40\}$. The CCDF represents the probability that a certain gain value is achieved.

may offer throuhputs increments of up to $\Delta_R \times B = 230$ Mbps with a probability of 0.5 when the jacket multi–antenna terminal is employed and $W/N = 4$, then it would

be possible to provide services like real-time thermal vision, Multi–person video call or E-health whose required throughputs are 50, 90 and 150 Mbps respectively [141].

Taking into account that the highest data rate gains are obtained when using the textile antenna array deployed in the backside of a jacket since a larger number of antennas can be deployed at the UE, from now on the simulations will be performed for the 2.5 GHz planar textile antenna array.

4.4.2 Power saving and coverage analysis

4.4.2.1 Multi-antenna terminal power gain

With the use of the textile multi-antenna proposal, a post-processing power gain with respect to a SIMO system, which results from the MIMO processing and that can be interpreted as a reduction of the required SNR to achieve a target rate ($R_{\text{objective}}$), can be obtained. Specifically, this power gain is defined in (4.12) as the difference between the SNR required to achieved a target rated if the UE only possesses one antenna and the SNR required to achieved the same target rate if the UE possesses more than one antenna.

$$G_{\text{textile}}\,[dB] = 10\log_{10}\left(\frac{2^{R_{\text{objective}}}-1}{2^{\frac{R_{\text{objective}}}{\min(M,N/W)}}-1}\right) \tag{4.12}$$

where $R_{\text{objective}}$ represents the required rate in bits/s/Hz that allows to provide an specific multimedia service and it is calculated in (4.13) as an approximation of the achievable rate for MIMO systems [142] when no channel knowledge at the transmitter is being considered.

$$R_{\text{objective}} \approx \min\left(M, N/W\right)\log_2\left(1+\mathsf{SNR}\right) \tag{4.13}$$

Fig. 4.7 illustrates this post-processing power gain for four different target rates which depending on the available bandwidth could enable several multimedia services. For instance, if B = 20 MHz multimedia services whose required throughput (obtained as $R_{\text{objective}} \times B$) ranges from 40 Mbps up to 300 Mbps may be offered. Concerning the post-processing gains, logically these are higher as the target rate increases since the required SNR is smaller when the UE is integrated by multiple antennas than when it

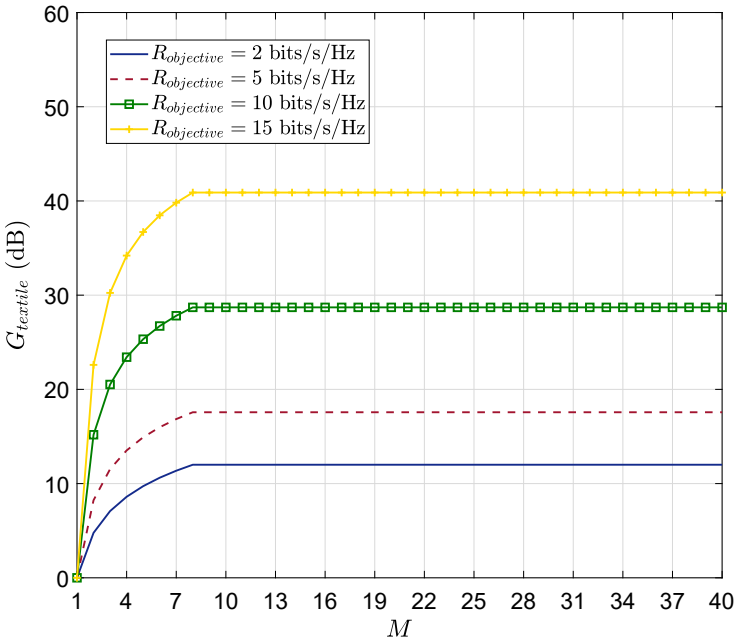

(a) BS/RN integrated by 8 antennas.

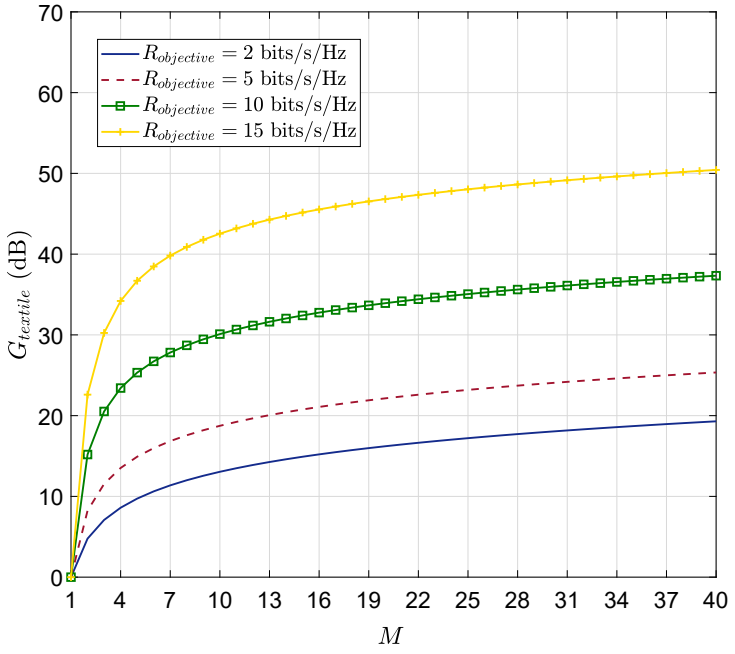

(b) BS/RN integrated by 40 antennas.

FIGURE 4.7: Achieved power gain for four target rates when different number of antennas are deployed at the textil multi-antenna terminal (backside of a jacket) and when the BS/RN is integrated by 8 and 40 respectively.

is integrated only by one antenna. Particularly, gains ranging from 12 dB to 41 dB (see Fig. 4.7(a)) and from 19 dB to 51 dB (see Fig. 4.7(b)) can be reached depending on the number of antennas deployed at the BS/RN and the target rate when 40 antennas are

deployed at the user end. As expected by its definition, it is also worth noting that the reached post-processing power gains are restricted to the minimum number of antennas at the transmitter or the receiver, this behavior is clearly shown in Fig. 4.7(a) where from 8 antennas onwards the gain remains constant.

4.4.2.2 Received power range

Once we have quantified the post-processing gain derived from the use of the textile array, we evaluate the power improvement in one of the considered hostile environments in emergency communications, specifically an outdoor-to-indoor propagation environment. It should be noted that the power is directly related with the coverage range. Then, it is considered that a power improvement implies a coverage extension.

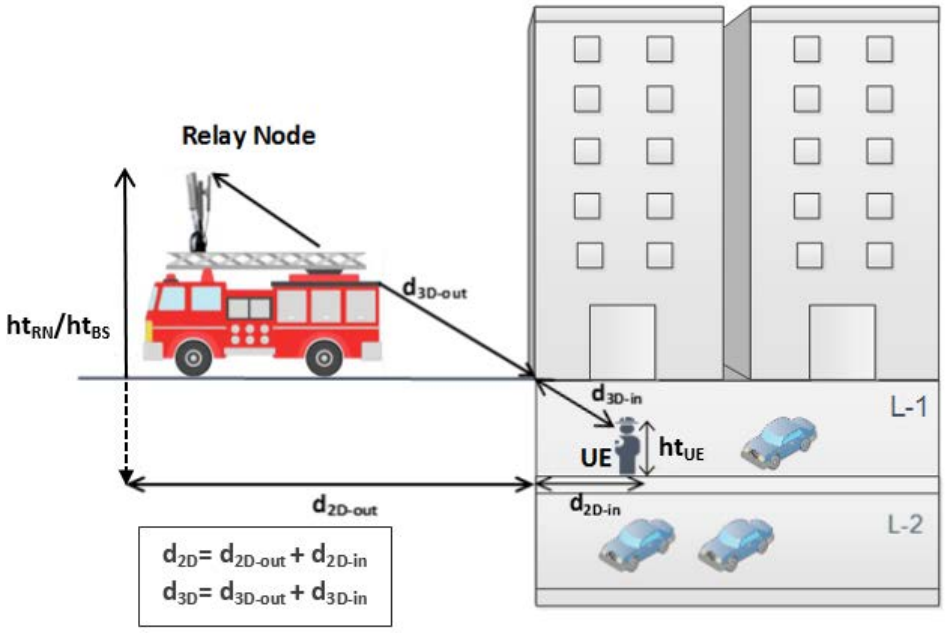

FIGURE 4.8: Parameters defined in the 3D channel model.

The power received by the BS/RN (depending if we are in a single–hop or two–hop scenario) in an Outdoor-to-Indoor propagation environment, assuming isotropic receiving antennas will be given as

$$P_R^{\mathrm{BS/RN}}\,[dBm] = P_T^{\mathrm{UE}} + G_{\mathrm{textile}} - P_{L_{O2I}} \tag{4.14}$$

where P_T^{UE} is the UE effective radiated power (ERP), G_{textile} represents the MIMO gain shown in the previous subsection and $P_{L_{O2I}}$ defined in (4.15) represents the O2I path–loss model provided by 3GPP taking into consideration a 3D channel model in an urban micro (UMi) small cell [143].

$$P_{L_{O2I}}\,[dB] = P_{L_b} + P_{L_{tw}} - P_{L_{in}} \tag{4.15}$$

here, P_{L_b} represents basic path-loss, $P_{L_{tw}}$ defines the loss through wall and $P_{L_{in}}$ gives the loss inside.

$$P_{L_b}(d_{3D})\,[dB] = PL_{3D-UMI}\,(d_{3D}) \tag{4.16}$$

$$P_{L_{tw}}\,[dB] = 20 \tag{4.17}$$

$$P_{L_{in}}(d_{2D-in})\,[dB] = 0.5 d_{2D-in} \tag{4.18}$$

Additionally, it must be noticed that parameters in (4.16) and (4.18) are represented in Fig. 4.8, except the term PL_{3D-UMI} that represents the losses of a 3D-UMi O2O scenario. In the event that the link between the transmitter and the receiver is determined to be LOS, PL_{3D-UMI} is defined as follows:

if 10 m $< d_{2D} < d'_{BP}$:

$$P_{L_{3D-UMI}}(d_{3D})\,[dB] = 22\log_{10}(d_{3D}) + 28 + 20\log_{10}(f_c) \tag{4.19}$$

if $d'_{BP} < d_{2D}$:

$$\begin{aligned} P_{L_{3D-UMI}}(d_{3D})\,[dB] = {} & 40\log_{10}(d_{3D}) + 28 + 20\log_{10}(f_c) \\ & -9\log_{10}((d'_{BP})^2 + (ht_{BS}/ht_{RN} - ht_{UE})^2) \end{aligned} \tag{4.20}$$

and d'_{BP} is the break point distance given by:

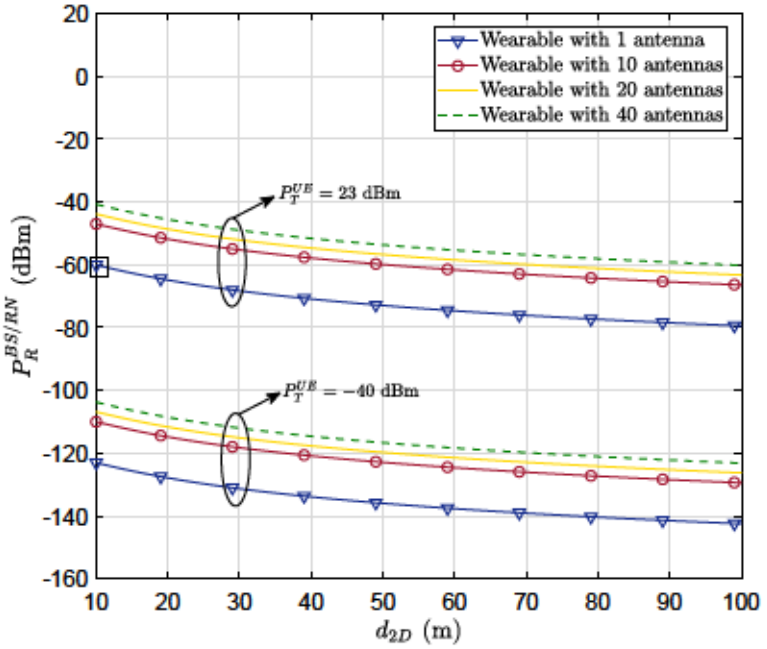

(a) $R_{\text{objective}} = 2$ bits/s/Hz

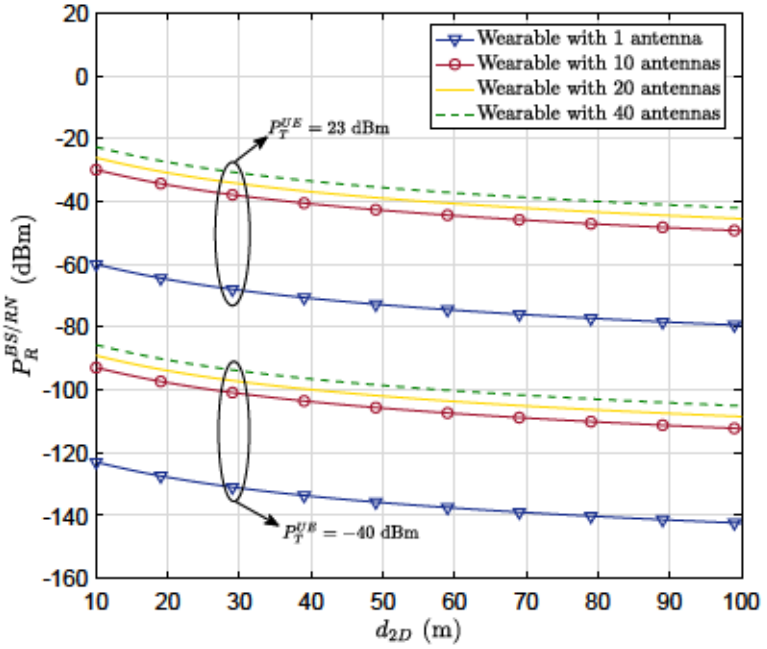

(b) $R_{\text{objective}} = 10$ bits/s/Hz

FIGURE 4.9: Power received (P_R) in an O2I scenario for two different required rates $R_{\text{objective}} = \{2, 10\}$ bits/s/Hz when the number of antennas at the BS is $N = 40$ and different antenna configurations are presented at the jacket. $P_T^{UE} = \{-40, 23\}$ dBm takes the minimum and maximum UE transmitted power values defined by the LTE standard. $ht_{UE} = 1.5$ m and $ht_{RN}/ht_{BS} = 10$ m. $d_{2D\ in} = 5$ m.

$$d'_{BP}\,[m] = \frac{4(ht_{BS}/ht_{RN} - 1)(ht_{UE} - 1)f_o}{c} \tag{4.21}$$

where ht_{BS}/ht_{RN} and ht_{UE} are respectively BS or RN height and the UE height.

Fig. 4.9 illustrates how the received power range is incremented as the number of antennas at the UE increases. Attending to Fig. 4.9(a), it is clearly shown how the received power range is improved. For instance, if we focus on the specific distance at which $P_R^{\mathrm{BS/RN}} = -60$ dBm, the improvement ranges from 41 m (wearable with $M = 10$ antennas) to 88 m (wearable with $M = 40$ antennas) with respect to single–antenna UEs. Additionally, comparing Fig. 4.9(a) and Fig. 4.9(b) it is verified how the power range increment increases as the required rates increase since the difference between the SNR needed to reach an specific rate when the UE has only one antenna and when it has multiple antennas is also higher. For instance, if we focus again on evaluating the specific distance at which $P_R^{\mathrm{BS/RN}} = -60$ dBm when the UE has $M = 10$ antennas compare to the case when only has one antenna, we appreciate a distance improvement of 41 m for $R_{\mathrm{objective}} = 2$ bits/s/Hz. If conversely, $R_{\mathrm{objective}} = 10$ bits/s/Hz a range distance of hundreds of meters can be reached.

In view of the results, we can verify the received power improvement and consequently also the coverage improvement derived from the use of the textile multi-antenna terminal.

4.4.3 Optimal relay allocation

As it has been previously mentioned, the communication link in emergency communications must be reliable since vital information is involved. Due to this fact, scenarios presenting low SNR are perfect candidates for the deployment of a MIMO-based relay solution not only because of its capability of extending coverage, but also of improving the transmission reliability. To illustrate that, in this section we evaluate the best location for the relay node with the aim of ensuring that an specific multimedia service which requires a determined average achievable rate is permanently provided. For instance, imagine that after an earthquake medical services need to use E-Health multimedia service, whose required rate is 150 Mbps [141] in order to perform a surgery in an underground gallery. Or imagine that during a fire in an underground multi-storey car

park firefighters need real–time thermal vision, whose required rate is 50 Mbps [141], in order to look for potential victims through thick smoke.

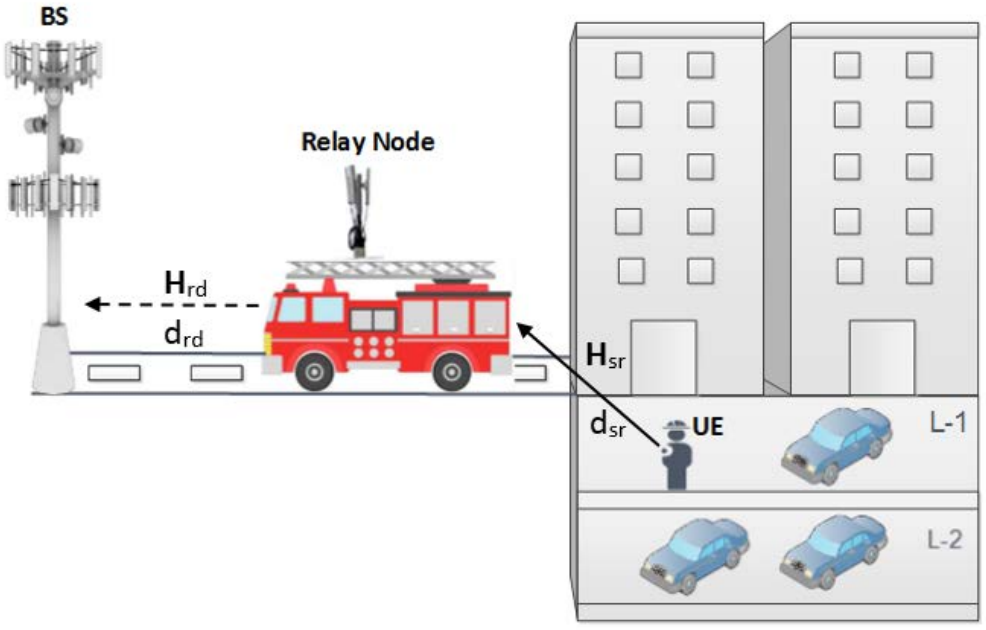

FIGURE 4.10: Schematic of the distance model.

To carry out these simulations, the SNR model described below assumes an path–loss exponent of $\alpha_{\mathrm{O2I}} = 3.32$ as the one measured in Chapter 3, for the O2I propagation link (established between the UE and the RN) with the UE equipped with textile antennas placed underground and an path–loss exponent of $\alpha_{\mathrm{O2O}} = 3$ for the O2O propagation link established between the RN and the BS in an urban area (this value is extracted from Table 3.1). In this model, the position of the relay location is normalized, in Fig. 4.10 the distances model is presented.

$$\mathsf{SNR}_{\mathrm{sr}} = P_T^{\mathrm{UE}} (1 - d_{sr})^{\alpha_{\mathrm{O2I}}} \tag{4.22}$$

where d_{sr} represents the distance between the source and the relay node and the power transmitted by the source is defined as $P_T^{\mathrm{UE}} = \mathsf{SNR}_{\mathrm{ref}} 1^{\alpha_{\mathrm{O2I}}}$ where $\mathsf{SNR}_{\mathrm{ref}}$ denotes the average value of the total link SNR that enables to establish an specific power level in the whole link.

$$\mathsf{SNR}_{\mathrm{rd}} = P_T^{\mathrm{RN}} d_{rd}^{-\alpha_{\mathrm{O2O}}} \tag{4.23}$$

where d_{rd} is the distance between the relay node and the destination.

Finally, the achievable rates of the amplify–and–forward half–duplex MIMO-based two-hop single relay channel, with $\mathbf{F}$ as in (4.8) and (4.10) can be written as follows [144, 145]:

$$R = \frac{1}{2}\log_2 \det\left(\mathbf{I}_N + \frac{4\mathsf{SNR}_{\mathrm{rd}}\mathsf{SNR}_{\mathrm{sr}}}{M}\frac{\mathbf{H}_{\mathrm{rd}}\mathbf{H}_{\mathrm{sr}}\mathbf{H}_{\mathrm{sr}}^{\dagger}\mathbf{H}_{\mathrm{rd}}^{\dagger}}{2\mathsf{SNR}_{\mathrm{rd}}\mathbf{H}_{\mathrm{rd}}\mathbf{H}_{\mathrm{rd}}^{\dagger} + 2\mathsf{SNR}_{\mathrm{sr}}\left\|\mathbf{H}_{\mathrm{sr}}\right\|_F^2\mathbf{I}_N + \mathbf{I}_N}\right) \quad (4.24)$$

Since the transmission is completed in two different time instances, the spectral efficiency is reduced by half and the SNR of each of the links are doubled.

Next, the results of analyzing the optimal relay position to maximize the achieved capacity for different antenna configurations are presented. In this particular case, we consider the same number of antennas in all communications ends $M = W = N = \{1, 4, 8, 20, 30, 40\}$ and study the impact of the $\mathsf{SNR}_{\mathrm{ref}}$ level on the optimization. Simulations are performed generating 500 channel samples using the channel model presented in Section 4.3. The plots include as a reference the required rates to provide different multimedia services, showing which is the best relay configuration (position) to offer them permanently.

From Fig. 4.11 it is possible to corroborate that the relay node presence is specially useful to extend the coverage region, of course this coverage extension is higher when high $\mathsf{SNR}_{\mathrm{ref}}$ levels are available. For instance, when $\mathsf{SNR}_{\mathrm{ref}} = -6$ dB it would be possible to permanently provide E-Health service when $M = W = N = 40$ from 0.05 to 0.235 distances. However, when $\mathsf{SNR}_{\mathrm{ref}} = -3$ dB for the same antenna configuration it would be possible to permanently provide E-Health service from 0.05 to 0.385 normalized distances.

On the other hand, as expected as the SNR levels increase, the peak achievable rate values reached by the relay network also increase. That means that inside a certain coverage region it would be possible to permanently offer more multimedia services with the same antenna configuration. For example, if the antenna configuration is $M = W = N = 8$ and the $\mathsf{SNR}_{\mathrm{ref}}$ is -6 dB or -3 dB (see Figs.4.11(a) and 4.11(b)), then only Bi-directional remote controlling and Real–time thermal vision could be constantly provided. On the other hand, if $\mathsf{SNR}_{\mathrm{ref}} = 0$ dB (see Fig. 4.11(c)), Multi-person video call service could also be among the provided multimedia services. Finally, if $\mathsf{SNR}_{\mathrm{ref}} = 3$ dB (see Fig. 4.11(d)), then all the multimedia services could be permanently offered including E-Health service.

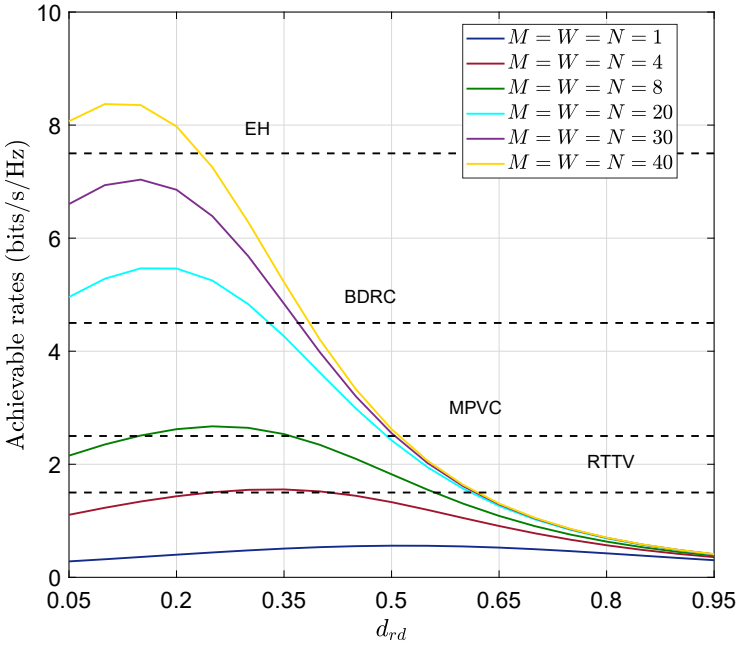

(a) $\mathsf{SNR}_{\mathrm{ref}} = -6$ dB

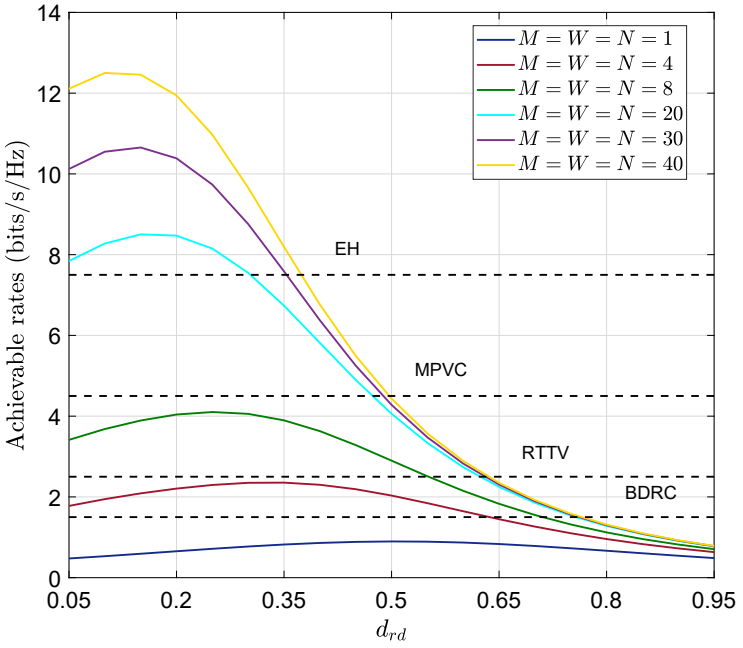

(b) $\mathsf{SNR}_{\mathrm{ref}} = -3$ dB

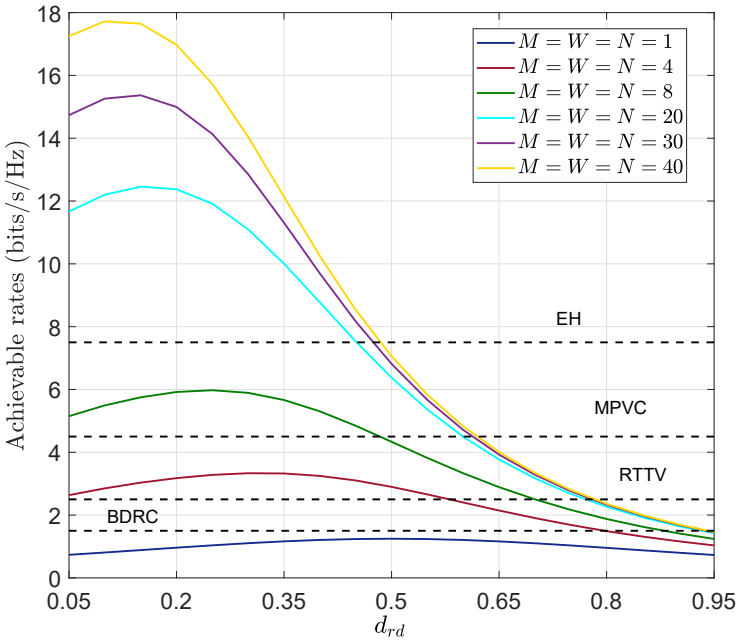

(c) $\mathsf{SNR}_{\text{ref}} = 0$ dB

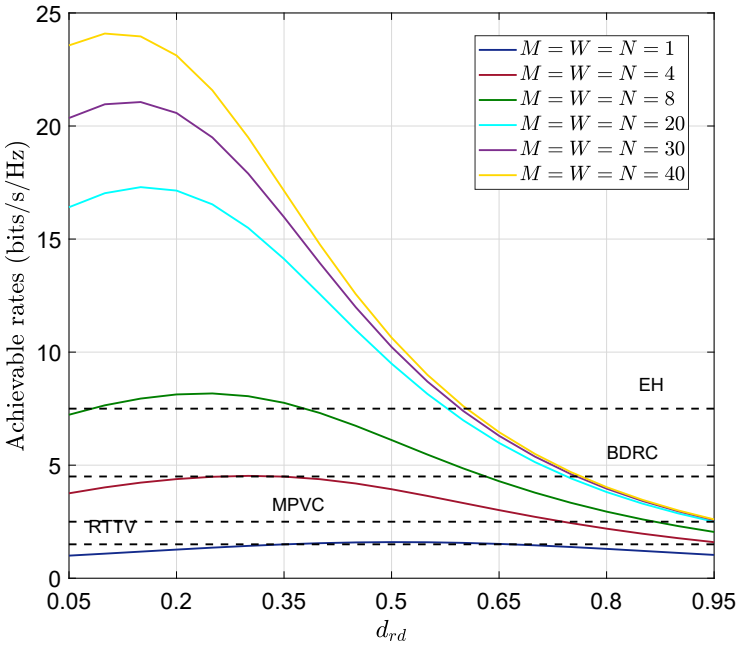

(d) $\mathsf{SNR}_{\text{ref}} = 3$ dB

FIGURE 4.11: Relation between the normalized relay location and the achieved rate at different SNR regimes and antenna configurations, considering $M = W = N$. The dotted lines represent the required rates of E-Health (EH), Multi-person video call (MPVC), Real–time thermal vision (RTTV) and Bi–directional remote controlling (BDRC) multimedia services when the available bandwidth is $B = 20$ MHz.

Furthermore, from the results in Fig. 4.11 we can obtain the optimal relay position leading to maximize the number of available multimedia services that can be permanently provided. Of course, this position varies depending on the different antenna configurations.

4.5 Conclusions

This chapter proposes a network and physical layer solution based on LTE-A and future 5G capabilities to improve public safety communications, which are currently conveyed through narrow–band PMR systems like TETRA mainly focused on offering limited voice services. Based on that, the main contributions of this chapter can be summarized as follows:

- Suggestion of an LTE–based two–hop link network to reach locations with low or null coverage and a physical layer improvement via the deployment of a textile multi–antenna terminal at the user side.
- Introduction of the device technology and network elements required to implement such a network concept.
- Validation of the physical layer improvement via the rate gain and power benefits evaluation.
- Possible design criterion based on the reliable connectivity principle that considers a constant provision of determined multimedia services. Specifically, the optimal relay location is found while trying to maximize the performance of the amplify–and–forward relay network in terms of achievable rates.

Simulation results illustrate the viability of the proposed design, specifically for low SNR scenarios where the relay node will allow us to extend the coverage and the MIMO textile technology to improve the capacity.

Chapter 5

Conclusions and Future Work

5.1 Conclusions

Currently, there is an exponential demand of higher data rates and always on connectivities derived from the huge proliferation of smart devices and novel multimedia services (i.e. augmented information, E-health, etc.). To deal with these communications needs, large–scale MIMO technology is postulated as a key component within the next mobile generation of wireless communications (5G) due to the immense improvements in throughput and spectral efficiency it offers. Nevertheless, the deployment of large number of antennas at the user end is a real challenge due to the limited space available.

Therefore, in this dissertation the feasibility of textile multi–antenna terminals has been analyzed as a technological solution to overcome the aforementioned limitations.

Firstly, the design of textile antenna arrays at the user's garment was explored. It was proven that the design of textile multi–antenna terminals can be implemented at any frequency. In particular, in this Thesis since textile multi–antenna terminals could be understood as key enablers of future public safety communications, three different center frequencies (2.5, 3.5 and 4.9 GHz) corresponding to possible future public safety frequency bands were considered. The planar arrays working at 2.5 GHz and 3.5 GHz were specifically designed to be deployed in the backside of a jacket, while the conformal array working at 4.9 GHz was designed to be integrated in safety helmets. In this latest design it is corroborated that the working frequency can be slightly shifted due to the bend effect, then it is of relevant importance to take this detail into account during

the design stage of textile multi–antenna terminals. Additionally, with technological solutions as the multi–antenna terminals working in the very close proximity of the human body it is also particularly important to evaluate the power absorbed by the human tissue when it is exposed to electromagnetic fields. In this dissertation it is verified that the proposed solution complies with the standardized limits ensuring the safety of the users.

Secondly, using the textile multi–antenna terminal working at 3.5 GHz previously designed, the statistical channel modeling of relevant O2I propagation environments from the communications point of view (low coverage) has been performed through a measurement campaign. We have measured in Valparaíso (Chile) $30 \times 12 \times 72 \approx 26.000$ different channel fading samples, that have been carefully processed to extract all the relevant information required for the channel modeling. The final aim of the statistical characterization was to provide models for all the key parameters that affect the performance of the communication system in terms of achievable rates and then, to empirically evaluate the performance improvement thanks to the usage of enhanced multi–antenna terminals. We concluded that the normalization of the channel matrices has a big impact on the performance of the system. Moreover, as the presence of the direct component increases, the performance of the system in terms of achievable rates decreases (Ricean scenarios reach lower rates than Rayleigh scenarios). We also conclude that correlation plays an important role on the channel characterization and not considering it may lead to inaccurate estimates of achievable rates. On the other hand, as expected we corroborated that the achievable rates tend to saturate if the number of antennas at both communication ends does not grow in the same way. Finally, we empirically demonstrate the spectral efficiency improvement derived from the use of textile multi–antenna terminals.

Lastly, in order to enable future public safety communications and overcoming the weakness of current narrow–band PMR systems, we propose a physical layer improvement through the usage of textile multi–antenna terminals together with a two-hop LTE-based network proposal. On the one hand, the improvement in terms of data rate gain, power and coverage gain derived from the use of textile multi–antenna terminals is analyzed. The benefits offered by the textile solution are verified. On the other hand, the optimal relay position based on the need for reliable connectivity is evaluated. Concretely, depending on the available SNR and MIMO configuration and the specific position of

the relay node, we are able to predict what multimedia services will be permanently provided.

5.2 Future Directions

Based on the research state followed in this Thesis, future research lines can be split into three main blocks.

With respect to the textile-based MIMO antennas designed in this Thesis:

- Future wireless communication systems at millimeter waves are atracting great interest compare to those that work at infra–millimetrics frequencies since they offer advantages such as higher available bandwidth and low interference with adjacent networks [146]. With respect to the antennas technology, the size of the radiating elements are significantly reduced and thus the number of antennas directly deployed at the user end could significantly increased and consequently also the achievable rates. Then, a new design of the textile multi–antenna terminal could be performed at different millimeter wave frequencies. Of course, a new selection of materials will be required, but also new SAR characterization.
- With regard to the evaluation of the human exposure to textile antennas, a new analysis should be performed in the millimeter frequencies band, being possible to take into consideration different postures of the body models since changes in postures can modify the antenna performance and consequently the power absorption.

Regarding the channel model proposed in this Thesis as a future work it will be interesting to:

- Development of an alternative channel model in which the estimation of the K–factor takes into account not only the amplitude, but also the phase of the channel fading coefficients. To do it, it will be necessary to perform specific measurement campaigns considering specific movement geometries (i.e. straight line) as the one consider in [81].

- Perform other O2I studies applicable to wideband communication requirements for different sets of scenarios and distances and particularly for different frequency bands. Specifically, the comparison of the mmWave option vs lower frequencies such as considered in this Thesis is a highly relevant topic. This implies studying the tradeoff between high path–losses (i.e. low SNR and lower coverage) at mmWave frequencies in relation to the multi–antenna methods required to achieve adequate data rates within a limited bandwidth.

With regard to the technological proposal to enable future public safety communications:

- Verify its feasibility in a real test scenario where the LTE network architecture including a relay node will be deployed. The main idea would consist of validating the attributes of the proposal as in this Thesis was performed via simulation in Chapter 4. Then, an experimental characterization of the data rate and power gains derived from the use of the textile proposal would be obtained, as well as the design principle of the relay network based on its optimal position when trying to ensure reliable high data rate multimedia services.

Finally, a key aspect not covered by this dissertation and that deserve a depth study with the future aim of industrializing the textile multi–antenna terminal, is the hardware design. Specifically, the design concerning the radio frequency (RF) chains whose main tasks consist of up–converting the data streams to the desired frequency in transmission and down–converting and amplifying the target signal at reception. In particular, current designs of large–scale MIMO transmitters and receivers usually require dedicated RF chains per each antenna element. Hence, this makes the hardware complexity grow and consequently the physical size, portability and cost of textile multi–antenna terminals also grow with. Then, it would be desirable to explore hardware solutions that implements hybrid precoding (HP) whose main goal is reducing the number of RF chains by splitting the precoding implementation into digital baseband processing, bandpass modulation and analog processing [147]. Therefore, the feasibility of the textile multi–antenna terminal would be theoretically and empirically characterized following the new design criteria.

Bibliography

[1] A. Osseiran, J. F. Monserrat, and P. Marsch, *5G mobile and wireless communications technology*. Cambridge University Press, 2016.

[2] J. G. Andrews, S. Buzzi, W. Choi, S. V. Hanly, A. Lozano, A. C. Soong, and J. C. Zhang, "What will 5G be?," *IEEE Journal on Selected Areas in Communications*, vol. 32, no. 6, pp. 1065–1082, 2014.

[3] S. Chen and J. Zhao, "The requirements, challenges, and technologies for 5G of terrestrial mobile telecommunication," *IEEE Communications Magazine*, vol. 52, no. 5, pp. 36–43, 2014.

[4] M. Agiwal, A. Roy, and N. Saxena, "Next Generation 5G Wireless Networks: A Comprehensive Survey," *IEEE Communications Surveys Tutorials*, vol. 18, no. 3, pp. 1617–1655, 2016.

[5] F. Boccardi, R. Heath, A. Lozano, T. Marzetta, and P. Popovski, "Five disruptive technology directions for 5G," *IEEE Communications Magazine*, vol. 52, pp. 74–80, February 2014.

[6] A. Jamil, M. Z. Yusoff, and N. Yahya, "Current issues and challenges of mimo antenna designs," *2010 International Conference on Intelligent and Advanced Systems*, pp. 1–5, 2010.

[7] M. Sánchez-Fernández, A. Tulino, E. Rajo-Iglesias, J. Llorca, and A. G. Armada, "Blended antenna wearables for an unconstrained mobile experience," *IEEE Communications Magazine*, vol. 55, pp. 160–168, April 2017.

[8] B. K. Lau and Z. Ying, "Antenna design challenges and solutions for compact MIMO terminals," *2011 International Workshop on Antenna Technology (iWAT)*, pp. 70–73, March 2011.

[9] P. Fletcher, M. Dean, and A. Nix, "Mutual coupling in multi-element array antennas and its influence on MIMO channel capacity," *Electronics Letters*, vol. 39, no. 4, pp. 342–344, 2003.

[10] V. Jungnickel, V. Pohl, and C. Von Helmolt, "Capacity of MIMO systems with closely spaced antennas," *IEEE Communications Letters*, vol. 7, no. 8, pp. 361–363, 2003.

[11] J. Ren, W. Hu, Y. Yin, and R. Fan, "Compact printed MIMO antenna for UWB applications," *IEEE Antennas and Wireless Propagation Letters*, vol. 13, pp. 1517–1520, 2014.

[12] S. Shoaib, I. Shoaib, N. Shoaib, X. Chen, and C. G. Parini, "Design and Performance Study of a Dual-Element Multiband Printed Monopole Antenna Array for MIMO Terminals," *IEEE Antennas and Wireless Propagation Letters*, vol. 13, pp. 329–332, 2014.

[13] Y.-J. Ren, "Ceramic based small LTE MIMO handset antenna," *IEEE Transactions on Antennas and Propagation*, vol. 61, no. 2, pp. 934–938, 2013.

[14] C. A. Balanis, "Antenna Theory: Analysis & Design, John Willey & Sons," *Inc. Publication*, 1997.

[15] G. A. Deschamps, "Microstrip microwave antennas," *Proceedings of the Third Symposium on the USAF Antenna Research and Development Program*, pp. 18–22, 1953.

[16] J. Howell, "Microstrip antennas," *IEEE Transactions on Antennas and Propagation*, vol. 23, no. 1, pp. 90–93, 1975.

[17] K.-L. Wong and W.-H. Hsu, "A broad-band rectangular patch antenna with a pair of wide slits," *IEEE Transactions on Antennas and Propagation*, vol. 49, no. 9, pp. 1345–1347, 2001.

[18] Y. Li, Chair, Luk, and Lee, "Broadband triangular patch antenna with a folded shorting wall," *IEEE Antennas and Wireless Propagation Letters*, vol. 3, pp. 189–192, 2004.

[19] X. Dai, T. Zhou, and G. Cui, "Dual-Band Microstrip Circular Patch Antenna With Monopolar Radiation Pattern," *IEEE Antennas and Wireless Propagation Letters*, vol. 15, pp. 1004–1007, 2016.

[20] L. Han, W. Zhang, X. Chen, G. Han, and R. Ma, "Design of Compact Differential Dual-Frequency Antenna With Stacked Patches," *IEEE Transactions on Antennas and Propagation*, vol. 58, pp. 1387–1392, April 2010.

[21] J. Anguera, L. Boada, C. Puente, C. Borja, and J. Soler, "Stacked H-shaped microstrip patch antenna," *IEEE Transactions on Antennas and Propagation*, vol. 52, no. 4, pp. 983–993, 2004.

[22] D. M. Pozar, "Microstrip antennas," *Proceedings of the IEEE*, vol. 80, no. 1, pp. 79–91, 1992.

[23] O. Ahmed and A.-R. Sebak, "Mutual coupling effect on ultrawideband linear antenna array performance," *International Journal of Antennas and Propagation*, vol. 2011, 2011.

[24] C. Hertleer, A. Tronquo, H. Rogier, L. Vallozzi, and L. V. Langenhove, "Aperture-Coupled Patch Antenna for Integration Into Wearable Textile Systems," *IEEE Antennas and Wireless Propagation Letters*, vol. 6, pp. 392–395, 2007.

[25] Q. Bai and R. Langley, "Crumpled integrated AMC antenna," *Electronics Letters*, vol. 45, pp. 662 –663, June 2009.

[26] I. Locher, M. Klemm, T. Kirstein, and G. Trster, "Design and Characterization of Purely Textile Patch Antennas," *IEEE Transactions on Advanced Packaging*, vol. 29, pp. 777–788, Nov 2006.

[27] M. Tanaka and J.-H. Jang, "Wearable microstrip antenna," *IEEE Antennas and Propagation Society International Symposium. Digest. Held in conjunction with: USNC/CNC/URSI North American Radio Sci. Meeting*, vol. 2, pp. 704–707, June 2003.

[28] B. Sanz-Izquierdo, J. C. Batchelor, and M. I. Sobhy, "Button antenna on textiles for wireless local area network on body applications," *IET Microwaves, Antennas Propagation*, vol. 4, pp. 1980–1987, November 2010.

[29] A. Tsolis, W. Whittow, A. Alexandridis, and J. Vardaxoglou, "Embroidery and related manufacturing techniques for wearable antennas: challenges and opportunities," *Electronics*, vol. 3, no. 2, pp. 314–338, 2014.

[30] M. Klemm, I. Locher, and G. Troster, "A novel circularly polarized textile antenna for wearable applications," *7th European Conference on Wireless Technology*, pp. 285–288, Oct 2004.

[31] L. Vallozzi, H. Rogier, and C. Hertleer, "Dual Polarized Textile Patch Antenna for Integration Into Protective Garments," *IEEE Antennas and Wireless Propagation Letters*, vol. 7, pp. 440–443, 2008.

[32] E. K. Kaivanto, M. Berg, E. Salonen, and P. de Maagt, "Wearable Circularly Polarized Antenna for Personal Satellite Communication and Navigation," *IEEE Transactions on Antennas and Propagation*, vol. 59, pp. 4490–4496, Dec 2011.

[33] H. Lee, J. Tak, and J. Choi, "Wearable Antenna Integrated into Military Berets for Indoor/Outdoor Positioning System," *IEEE Antennas and Wireless Propagation Letters*, vol. 16, pp. 1919–1922, 2017.

[34] J. Tak and J. Choi, "An All-Textile Louis Vuitton Logo Antenna," *IEEE Antennas and Wireless Propagation Letters*, vol. 14, pp. 1211–1214, 2015.

[35] S. Shahid, M. Rizwan, M. A. B. Abbasi, H. Zahra, S. M. Abbas, and M. A. Tarar, "Textile antenna for body centric WiMAX and WLAN applications," *2012 International Conference on Emerging Technologies*, pp. 1–5, Oct 2012.

[36] "IEEE Recommended Practice for Measurements and Computations of Radio Frequency Electromagnetic Fields With Respect to Human Exposure to Such Fields, 100 KHz-300 GHz," *IEEE Std C95.3-2002*, 2002.

[37] Y. F. Cao, X. Y. Zhang, and T. Mo, "Low-profile conical-pattern slot antenna with wideband performance using artificial magnetic conductors," *IEEE Transactions on Antennas and Propagation*, vol. 66, pp. 2210–2218, May 2018.

[38] M. J. Ackerman, "The Visible Human Project," *Proceedings of the IEEE*, vol. 86, pp. 504–511, March 1998.

[39] M. Fernandez, H. G. Espinosa, D. V. Thiel, and A. Arrinda, "Wearable slot antenna at 2.45 GHz for off-body radiation: Analysis of efficiency, frequency shift, and body absorption," *Bioelectromagnetics*, vol. 39, no. 1, pp. 25–34, 2018.

[40] J. W. Wallace, W. Ahmad, Y. Yang, R. Mehmood, and M. A. Jensen, "A Comparison of Indoor MIMO Measurements and Ray-Tracing at 24 and 2.55 GHz," *IEEE Transactions on Antennas and Propagation*, vol. 65, no. 12, pp. 6656–6668, 2017.

[41] J. W. Wallace, M. A. Jensen, A. L. Swindlehurst, and B. D. Jeffs, "Experimental characterization of the MIMO wireless channel: Data acquisition and analysis," *IEEE Transactions on Wireless Communications*, vol. 2, no. 2, pp. 335–343, 2003.

[42] D. Chizhik, J. Ling, P. W. Wolniansky, R. A. Valenzuela, N. Costa, and K. Huber, "Multiple-input-multiple-output measurements and modeling in Manhattan," *IEEE Journal on Selected Areas in Communications*, vol. 21, no. 3, pp. 321–331, 2003.

[43] R. Zhang, X. Lu, J. Zhao, L. Cai, and J. Wang, "Measurement and modeling of angular spreads of three-dimensional urban street radio channels," *IEEE Transactions on Vehicular Technology*, vol. 66, no. 5, pp. 3555–3570, 2017.

[44] V. Kristem, S. Sangodoyin, C. U. Bas, M. Kaeske, J. Lee, C. Schneider, G. Sommerkorn, C. J. Zhang, R. S. Thomae, and A. F. Molisch, "3D MIMO Outdoor-to-Indoor Propagation Channel Measurement," *IEEE Transactions on Wireless Communications*, vol. 16, no. 7, pp. 4600–4613, 2017.

[45] S. Wyne, A. F. Molisch, P. Almers, G. Eriksson, J. Karedal, and F. Tufvesson, "Outdoor-to-indoor office MIMO measurements and analysis at 5.2 GHz," *IEEE Transactions on Vehicular Technology*, vol. 57, no. 3, pp. 1374–1386, 2008.

[46] Q. Zheng, J. Zhang, H. Yu, Y. Zhang, and L. Tian, "Propagation statistic characteristic of 3D MIMO channel in outdoor-to-indoor scenario with different antenna heights," *Wireless Personal Multimedia Communications (WPMC), 2016 19th International Symposium on*, pp. 411–416, 2016.

[47] M. C. Jeruchim, P. Balaban, and K. S. Shanmugan, *Simulation of communication systems: modeling, methodology and techniques*. Springer Science & Business Media, 2006.

[48] A. Paulraj, R. Nabar, and D. Gore, *Introduction to Space-Time Wireless Communications*. Cambridge university press, 2003.

[49] T. S. Rappaport *et al.*, *Wireless communications: principles and practice*, vol. 2. Prentice Hall PTR New Jersey, 1996.

[50] G. Durgin, T. S. Rappaport, and H. Xu, "Measurements and models for radio path loss and penetration loss in and around homes and trees at 5.85 GHz," *IEEE Transactions on Communications*, vol. 46, no. 11, pp. 1484–1496, 1998.

[51] G. Durgin, T. S. Rappaport, and H. Xu, "5.85-GHz radio path loss and penetration loss measurements in and around homes and trees," *IEEE Communications Letters*, vol. 2, no. 3, pp. 70–72, 1998.

[52] S. Y. Seidel and T. S. Rappaport, "914 MHz path loss prediction models for indoor wireless communications in multifloored buildings," *IEEE Transactions on Antennas and Propagation*, vol. 40, no. 2, pp. 207–217, 1992.

[53] F. Hansen and F. I. Meno, "Mobile fading—Rayleigh and lognormal superimposed," *IEEE Transactions on Vehicular Technology*, vol. 26, no. 4, pp. 332–335, 1977.

[54] G. Tzeremes and C. G. Christodoulou, "Use of Weibull distribution for describing outdoor multipath fading," *IEEE Antennas and Propagation Society International Symposium*, vol. 1, pp. 232–235, June 2002.

[55] V. M. Rodrigo-Peñarrocha, J. Reig, L. Rubio, H. Fernández, and S. Loredo, "Analysis of small-scale fading distributions in vehicle-to-vehicle communications," *Mobile Information Systems*, vol. 2016, 2016.

[56] P. Almers, E. Bonek, A. Burr, N. Czink, M. Debbah, V. Degli-Esposti, H. Hofstetter, P. Kyösti, D. Laurenson, G. Matz, *et al.*, "Survey of channel and radio propagation models for wireless MIMO systems," *EURASIP Journal on Wireless Communications and Networking*, vol. 2007, no. 1, p. 019070, 2007.

[57] S. Oh and N. Myung, "MIMO channel estimation method using ray-tracing propagation model," *Electronics Letters*, vol. 40, no. 21, pp. 1350–1352, 2004.

[58] S. Loredo, A. Rodríguez-Alonso, and R. P. Torres, "Indoor MIMO channel modeling by rigorous GO/UTD-based ray tracing," *IEEE Transactions on Vehicular Technology*, vol. 57, no. 2, pp. 680–692, 2008.

[59] A. A. Saleh and R. Valenzuela, "A statistical model for indoor multipath propagation," *IEEE Journal on Selected Areas in Communications*, vol. 5, no. 2, pp. 128–137, 1987.

[60] T. Zwick, C. Fischer, and W. Wiesbeck, "A stochastic multipath channel model including path directions for indoor environments," *IEEE journal on Selected Areas in Communications*, vol. 20, no. 6, pp. 1178–1192, 2002.

[61] M. Debbah and R. R. Muller, "MIMO channel modeling and the principle of maximum entropy," *IEEE Transactions on Information Theory*, vol. 51, pp. 1667–1690, May 2005.

[62] A. G. Burr, "Capacity bounds and estimates for the finite scatterers MIMO wireless channel," *IEEE Journal on Selected Areas in Communications*, vol. 21, pp. 812–818, June 2003.

[63] W. Weichselberger, M. Herdin, H. Ozcelik, and E. Bonek, "A stochastic MIMO channel model with joint correlation of both link ends," *IEEE Transactions on Wireless Communications*, vol. 5, pp. 90–100, Jan 2006.

[64] C.-K. Wen, S. Jin, K.-K. Wong, J.-C. Chen, and P. Ting, "On the ergodic capacity of jointly-correlated Rician fading MIMO channels," *2011 IEEE International Conference on Acoustics, Speech and Signal Processing (ICASSP)*, pp. 3224–3227, 2011.

[65] G. J. Foschini, M. J. Gans, and J. M. Kahn, "Fading correlation and its effect on the capacity of multielement antenna systems," *IEEE Transactions on Communications*, vol. 48, pp. 502–513, March 2000.

[66] M. K. Çolakoğlu and M. Şafak, "On the MIMO channel capacity predicted by Kronecker and Müller models," *Wireless Personal Communications*, vol. 47, no. 1, pp. 91–100, 2008.

[67] F. R. Farrokhi, G. J. Foschini, A. Lozano, and R. A. Valenzuela, "Link-optimal space-time processing with multiple transmit and receive antennas," *IEEE Communications Letters*, vol. 5, pp. 85–87, March 2001.

[68] M. Sánchez-Fernández, S. Zazo, and R. Valenzuela, "Simplifying the beamforming optimality region for practical MIMO scenarios," *IEEE Communication Letters*, vol. 10, Nov. 2006.

[69] J. Salz and J. H. Winters, "Effect of fading correlation on adaptive arrays in digital mobile radio," *IEEE transactions on Vehicular Technology*, vol. 43, no. 4, pp. 1049–1057, 1994.

[70] D.-S. Shiu, G. J. Foschini, M. J. Gans, and J. M. Kahn, "Fading correlation and its effect on the capacity of multielement antenna systems," *IEEE Transactions on Communications*, vol. 48, no. 3, pp. 502–513, 2000.

[71] M. Rodríguez, R. Feick, R. A. Valenzuela, and D. Chizhik, "Achieving Near Maximum Ratio Combining Diversity Gains With Directive Antennas," *IEEE Transactions on Vehicular Technology*, vol. 66, no. 9, pp. 7782–7796, 2017.

[72] F. Silva, R. Feick, R. A. Valenzuela, M. S. Derpich, and L. Ahumada, "Measurement-Based Evaluation of Spectral Efficiencies in Outdoor-Indoor Multiuser MISO Systems in Femto-Cells," *IEEE Transactions on Wireless Communications*, vol. 15, pp. 5889–5903, Sept 2016.

[73] S. Loyka and G. Levin, "On physically-based normalization of MIMO channel matrices," *IEEE Transactions on Wireless Communications*, vol. 8, pp. 1107–1112, March 2009.

[74] Z. Tang and A. S. Mohan, "Experimental investigation of indoor MIMO Ricean channel capacity," *IEEE Antennas and Wireless Propagation Letters*, vol. 4, pp. 55–58, 2005.

[75] C. J. Wang, K. A. Remley, A. T. Kirk, R. J. Pirkl, C. L. Holloway, D. F. Williams, and P. D. Hale, "Parameter estimation and uncertainty evaluation in a low Rician K-factor reverberation-chamber environment," *IEEE Transactions on Electromagnetic Compatibility*, vol. 56, no. 5, pp. 1002–1012, 2014.

[76] L. J. Greenstein, D. G. Michelson, and V. Erceg, "Moment-method estimation of the Ricean K-factor," *IEEE Communications Letters*, vol. 3, no. 6, pp. 175–176, 1999.

[77] A. Abdi, C. Tepedelenlioglu, M. Kaveh, and G. Giannakis, "On the estimation of the K parameter for the Rice fading distribution," *IEEE Communications letters*, vol. 5, no. 3, pp. 92–94, 2001.

[78] C. Tepedelenlioglu, A. Abdi, and G. B. Giannakis, "The Ricean K factor: estimation and performance analysis," *IEEE Transactions on Wireless Communications*, vol. 2, no. 4, pp. 799–810, 2003.

[79] Y. Chen and N. C. Beaulieu, "Maximum likelihood estimation of the K factor in Ricean fading channels," *IEEE Communications Letters*, vol. 9, no. 12, pp. 1040–1042, 2005.

[80] K. E. Baddour and T. J. Willink, "Improved estimation of the Ricean K-factor from I/Q fading channel samples," *IEEE Transactions on Wireless Communications*, vol. 7, no. 12, pp. 5051–5057, 2008.

[81] T. J. Willink and G. W. K. Colman, "Measurement-based analysis of cross-layer adaptation for MIMO in mobile urban environments," *IET Communications*, vol. 7, pp. 697–705, May 2013.

[82] Y. Hikiyama, H. Tsutsui, and Y. Miyanaga, "MIMO propagation scenario discrimination for adaptive wireless communication systems," *2013 13th International Symposium on Communications and Information Technologies (ISCIT)*, pp. 674–679, Sept 2013.

[83] S. Zhu, T. S. Ghazaany, S. M. Jones, R. A. Abd-Alhameed, J. M. Noras, T. Van Buren, J. Wilson, T. Suggett, and S. Marker, "Probability Distribution of Rician K-Factor in Urban, Suburban and Rural Areas Using Real-World Captured Data," *IEEE Transactions on Antennas and Propagation*, vol. 62, no. 7, pp. 3835–3839, 2014.

[84] C. Oestges, B. Clerckx, D. Vanhoenacker-Janvier, and A. Paulraj, "Impact of diagonal correlations on MIMO capacity: application to geometrical scattering models," *IEEE 58th Vehicular Technology Conference. VTC 2003-Fall*, vol. 1, pp. 394–398, Oct 2003.

[85] S. Oh and N. Myung, "MIMO channel estimation method using ray-tracing propagation model," *Electronics Letters*, vol. 40, no. 21, pp. 1350–1352, 2004.

[86] S. Büyükçorak and G. Karabulut Kurt, "Simulation and measurement of spatial correlation in MIMO systems with ray tracing," *5th International Conference on Signal Processing and Communication Systems (ICSPCS)*, pp. 1–5, Dec 2011.

[87] D. P. McNamara, M. A. Beach, and P. N. Fletcher, "Spatial correlation in indoor MIMO channels," *The 13th IEEE International Symposium on Personal, Indoor and Mobile Radio Communications*, vol. 1, pp. 290–294, Sep. 2002.

[88] P. L. Kafle, A. Intarapanich, A. B. Sesay, J. Mcrory, and R. J. Davies, "Spatial correlation and capacity measurements for wideband MIMO channels in indoor office environment," *IEEE Transactions on Wireless Communications*, vol. 7, pp. 1560–1571, May. 2008.

[89] J. Tsai and B. D. Woerner, "The fading correlation function of a circular antenna array in mobile radio environment," *GLOBECOM'01. IEEE Global Telecommunications Conference*, vol. 5, pp. 3232–3236, 2001.

[90] W. Lee, "Effects on correlation between two mobile radio base-station antennas," *IEEE Transactions on Communications*, vol. 21, no. 11, pp. 1214–1224, 1973.

[91] W. R. Braun and U. Dersch, "A physical mobile radio channel model," *IEEE Transactions on Vehicular Technology*, vol. 40, no. 2, pp. 472–482, 1991.

[92] L. Xin and N. Zai-ping, "Spatial fading correlation of circular antenna arrays with laplacian PAS in MIMO channels," *IEEE Antennas and Propagation Society Symposium*, vol. 4, pp. 3697–3700, 2004.

[93] K. I. Pedersen, P. E. Mogensen, and B. H. Fleury, "Spatial channel characteristics in outdoor environments and their impact on BS antenna system performance," *48th IEEE Vehicular Technology Conference (VTC- 98). Pathway to Global Wireless Revolutiong*, vol. 2, pp. 719–723, May 1998.

[94] D. Gesbert, H. Bolcskei, D. Gore, and A. Paulraj, "MIMO wireless channels: Capacity and performance prediction," *Global Telecommunications Conference (Globecom-00)*, vol. 2, pp. 1083–1088, 2000.

[95] J.-P. Kermoal, L. Schumacher, K. I. Pedersen, P. E. Mogensen, and F. Frederiksen, "A stochastic MIMO radio channel model with experimental validation," *IEEE Journal on Selected Areas in Communications*, vol. 20, no. 6, pp. 1211–1226, 2002.

[96] F. C. Tenoudji, "Correlation and covariance matrices of a complex random vector," *Analog and Digital Signal Analysis*, pp. 467–481, 2016.

[97] K. Pedersen, P. Mogensen, and B. Fleury, "A stochastic model of the temporal and azimuthal dispersion seen at the base station in outdoor propagation environments," *IEEE Transactions on Vehicular Technology*, vol. 49, pp. 437 – 447, Mar. 2000.

[98] M. Sánchez-Fernández, S. Zazo, and R. Valenzuela, "Performance comparison between beamforming and spatial multiplexing for the downlink in wireless cellular systems," *IEEE Transactions on Wireless Communications*, vol. 6, pp. 2427–2431, July 2007.

[99] H. Xu, M. Gans, N. Amitay, R. A. Valenzuela, T. Sizer, R. Storz, D. Taylor, M. McDonald, and C. Tran, "MIMO channel capacity for fixed wireless: measurements and models," *IEEE 54th Vehicular Technology Conference. (VTC Fall-01). Proceedings*, vol. 2, pp. 1068–1072, Oct 2001.

[100] G. J. Foschini, "Layered space-time architecture for wireless communication in a fading environment when using multi-element antennas," *Bell Labs Technical Journal*, vol. 1, no. 2, pp. 41–59, 1996.

[101] J. Winters, "On the capacity of radio communication systems with diversity in a Rayleigh fading environment," *IEEE Journal on Selected Areas in Communications*, vol. 5, no. 5, pp. 871–878, 1987.

[102] E. Telatar, "Capacity of multi-antenna Gaussian channels," *European Transactions on Telecommunications*, vol. 10, no. 6, pp. 585–595, 1999.

[103] C. E. Shannon, "Communication in the presence of noise," *Proceedings of the IEEE*, vol. 86, no. 2, pp. 447–457, 1998.

[104] G. Raleigh and J. M. Cioffi, "Spatio-temporal coding for wireless communications," *Proceedings of GLOBECOM'96. 1996 IEEE Global Telecommunications Conference*, vol. 3, pp. 1809–1814, 1996.

[105] G. J. Foschini and M. J. Gans, "On limits of wireless communications in a fading environment when using multiple antennas," *Wireless Personal Communications*, vol. 6, no. 3, pp. 311–335, 1998.

[106] A. Goldsmith, S. Jafar, N. Jindal, and S. Vishwanath, "Capacity limits of MIMO channels," *IEEE Journal on Selected Areas in Communications*, vol. 21, pp. 684–702, June 2003.

[107] H. Huang, C. Papadias, and S. Venkatesan, *MIMO Communication for Cellular Networks*. Springer New York, 2012.

[108] C.-N. Chuah, D. N. C. Tse, J. M. Kahn, R. A. Valenzuela, *et al.*, "Capacity scaling in MIMO wireless systems under correlated fading," *IEEE Transactions on Information Theory*, vol. 48, no. 3, pp. 637–650, 2002.

[109] A. Tulino, A. Lozano, and S. Verdú, "Impact of antenna correlation on the capacity of mutiantenna channels," *IEEE Transactions on Information Theory*, vol. 51, pp. 2491 – 2509, July 2005.

[110] D. Chizhik, G. Foschini, and R. Valenzuela, "Capacities of multi-element transmit and receive antennas: Correlations and keyholes," *Electronics Letters*, vol. 36, no. 13, p. 1, 2000.

[111] R. U. Nabar, H. Bolcskei, and A. J. Paulraj, "Diversity and outage performance in space-time block coded Ricean MIMO channels," *IEEE Transactions on Wireless Communications*, vol. 4, pp. 2519–2532, Sept 2005.

[112] D. Sanderson and A. Sharma, *World Disasters Report. Resilience: saving lives today, investing for tomorrow*. International Federation of Red Cross and Red Crescent Societies, 2016.

[113] D. Guha-Sapir and R. Below, "Collecting Data on disasters: Easier said than done," *Asian Disaster Management News*, vol. 12, no. 2, pp. 9–10, 2006.

[114] "Sendai Framework for Disaster Risk Reduction 2015 - 2030," tech. rep., United Nations Office for Disaster Risk Reduction, 2015.

[115] I. Kamen, "A new approach to disaster communication and control systems," *Electrical Engineering*, vol. 81, pp. 535–541, July 1962.

[116] T. C. Chan, J. Killeen, W. Griswold, and L. Lenert, "Information Technology and Emergency Medical Care during Disasters," *Academic Emergency Medicine*, vol. 11, no. 11, pp. 1229–1236, 2004.

[117] R. Shaw, T. Izumi, and P. Shi, "Perspectives of Science and Technology in Disaster Risk Reduction of Asia," *International Journal of Disaster Risk Science*, vol. 7, pp. 329–342, Dec 2016.

[118] J. Heinzelman and C. Waters, "Crowdsourcing crisis information in disaster-affected Haiti," special report, United States Institute of Peace, 2010.

[119] S. Acharya and K. C. Budka, "Telecommunications in vertical markets: Challenges and opportunities," *Bell Labs Technical Journal*, vol. 16, pp. 1–4, Dec 2011.

[120] K. C. Budka, T. Chu, T. L. Doumi, W. Brouwer, P. Lamoureux, and M. E. Palamara, "Public safety mission critical voice services over LTE," *Bell Labs Technical Journal*, vol. 16, pp. 133–149, December 2011.

[121] A. R. McGee, M. Coutière, and M. E. Palamara, "Public safety network security considerations," *Bell Labs Technical Journal*, vol. 17, no. 3, pp. 79–86, 2012.

[122] T. Doumi, M. F. Dolan, S. Tatesh, A. Casati, G. Tsirtsis, K. Anchan, and D. Flore, "LTE for public safety networks," *IEEE Communications Magazine*, vol. 51, no. 2, pp. 106–112, 2013.

[123] TS 22.346, "Isolated Evolved Universal Terrestrial Radio Access Network (E-UTRAN) Operation for Public Safety; Stage 1," Tech. Rep. Release 13, 3GPP, 2014.

[124] A. Kumbhar, F. Koohifar, I. Güvenç, and B. Mueller, "A Survey on Legacy and Emerging Technologies for Public Safety Communications," *IEEE Communications Surveys Tutorials*, vol. 19, no. 1, pp. 97–124, 2017.

[125] GreenTouch Application Taxonomy Project, "GreenTouch Application Taxonomy," tech. rep., GreenTouch, Feb. 2012.

[126] J. Orlosky, K. Kiyokawa, and H. Takemura, "Virtual and Augmented Reality on the 5G Highway," *Journal of Information Processing*, vol. 25, pp. 133–141, 2017.

[127] TS 36.300, "Evolved Universal Terrestrial Radio Access (E-UTRA) and Evolved Universal Terrestrial Radio Access Network (E-UTRAN); Overall description; Stage 2," Tech. Rep. Release 13, 3GPP, 2010.

[128] TR 36.912, "Feasibility study for further advancements for E-UTRA (LTE-advanced)," Tech. Rep. Release 13, 3GPP, 2016.

[129] M. Iwamura, H. Takahashi, and S. Nagata, "Relay technology in LTE-advanced," *NTT DoCoMo Technical Journal*, vol. 12, no. 2, pp. 29–36, 2010.

[130] H. Holma and A. Toskala, *LTE advanced: 3GPP solution for IMT-Advanced*. John Wiley & Sons, 2012.

[131] E. Crespo-Bardera, M. Sánchez-Fernández, A. Garcia-Armada, A. G. Martín, and A. F. Durán, "Analysis of a LTE-based textile massive MIMO proposal for public safety networks," in *2017 IEEE 86th Vehicular Technology Conference (VTC-Fall)*, pp. 1–5, Sept 2017.

[132] TS 36.101, "Evolved Universal Terrestrial Radio Access (E-UTRA); User Equipment (UE) radio transmission and reception," Tech. Rep. Release 13, 3GPP, 2016.

[133] F. C. Commission, "FCC 02-47," 2002. https://www.fcc.gov/auction/n3.

[134] D. Chizhik, "Slowing the time-fluctuating MIMO channel by beam forming," *IEEE Transactions on Wireless Communications*, vol. 3, pp. 1554–1565, Sept 2004.

[135] T. Svantesson, "A physical MIMO radio channel model for multi-element multi-polarized antenna systems," in *IEEE Vehicular Technology Conference*, vol. 2, pp. 1083 – 1087, Oct. 2001.

[136] M. L. Pablo-González, M. Sánchez-Fernández, and E. Rajo-Iglesias, "Combination of the three types of diversity to design high-capacity compact MIMO terminals," *IEEE Antennas and Wireless Propagation Letters*, vol. 13, pp. 1309–1312, 2014.

[137] P. N. Fletcher, M. Dean, and A. R. Nix, "Mutual coupling in multi-element array antennas and its influence on MIMO channel capacity," *Electronics Letters*, vol. 39, pp. 342–344, Feb 2003.

[138] L. Jiang, L. Thiele, and V. Jungnickel, "Modeling and measurement of MIMO relay channels," *Vehicular Technology Conference (VTC-Spring)*, pp. 419–423, 2008.

[139] T. Q. Duong, L.-N. Hoang, and V. N. Q. Bao, "On the performance of two-way amplify-and-forward relay networks," *IEICE Transactions on Communications*, vol. 92, no. 12, pp. 3957–3959, 2009.

[140] M. Sánchez-Fernández, A. Tulino, E. Rajo-Iglesias, J. Llorca, and A. G. Armada, "Blended Antenna Wearables for an Unconstrained Mobile Experience," *IEEE Communications Magazine*, vol. 55, pp. 160–168, April 2017.

[141] E. Commission, *Communication from the Commission to the European Parliament, the Council, the European Economic and Social Committee and the Committee of the Regions. Connectivity for a competitive digital single market - Towards a European gigabit society.* Brussels, COM (2016) 587 Final.

[142] M. Kang and M.-S. Alouini, "Capacity of MIMO Rician channels," *IEEE Transactions on Wireless Communications*, vol. 5, no. 1, pp. 112–122, 2006.

[143] TR 36.873, "Study on 3D channel model for LTE," Tech. Rep. Release 12, 3GPP, 2016.

[144] P. Herhold, E. Zimmermann, and G. Fettweis, "On the performance of cooperative amplifyand-forward relay networks," *European Transactions on Telecommunications*, vol. 16, 2005.

[145] M. Herdin, "MIMO amplify-and-forward relaying in correlated MIMO channels," *Information, Communications and Signal Processing, 2005 Fifth International Conference on*, pp. 796–800, 2005.

[146] S. L. Cotton, W. G. Scanlon, and P. S. Hall, "A simulated study of co-channel inter-ban interference at 2.45 ghz and 60 ghz," *The 3rd European Wireless Technology Conference*, pp. 61–64, Sep. 2010.

[147] L. Liang, W. Xu, and X. Dong, "Low-Complexity Hybrid Precoding in Massive Multiuser MIMO Systems," *IEEE Wireless Communications Letters*, vol. 3, pp. 653–656, Dec 2014.

Errata

Chapter 2: Textile MIMO Antennas for the User End

- On page 13, Equation (2.1) should read: (remove normalization)

$$BW = f_H - f_L \tag{2.1}$$

where f_H and f_L represents the upper and lower frequency values at which the reflected power by the antenna is still less than 10% .

Chapter 4: Enabling Future Public Safety Communication Infrastructure

- On page 95, Figure 4.5 should read:

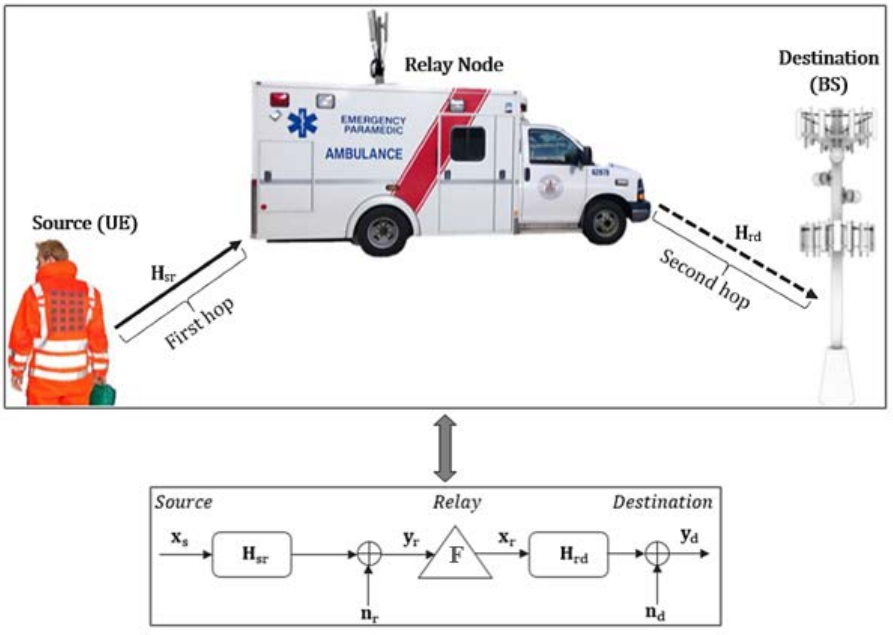

FIGURE 4.5: System model of a two–hop half–duplex single relay scenario working in the uplink.

- On page 108, Equation (4.22) should read: (missing negative sign)

$$\mathsf{SNR}_{\mathrm{sr}} = P_T^{\mathrm{UE}} \left(1 - d_{sr}\right)^{-\alpha_{\mathrm{O2I}}} \tag{4.22}$$

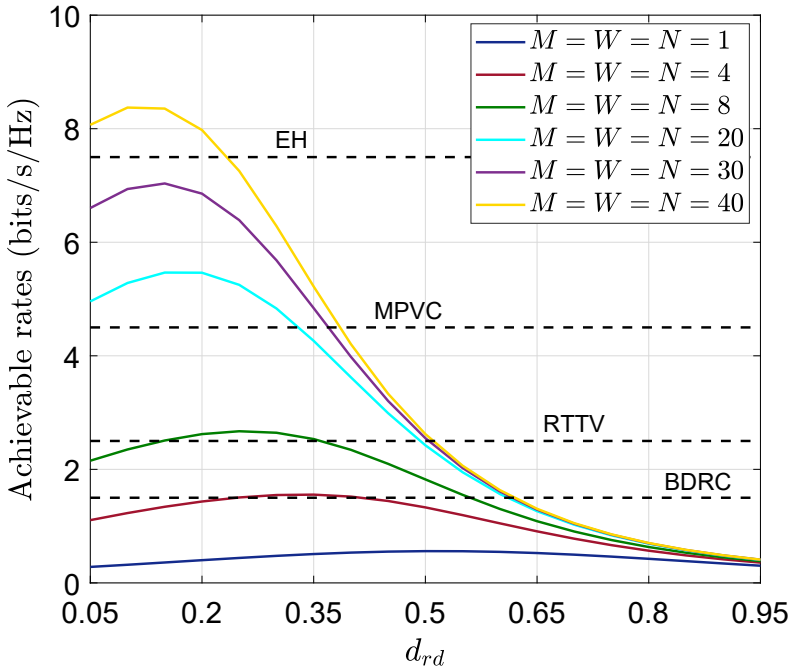

(a) $\mathrm{SNR}_{\mathrm{ref}} = -6$ dB

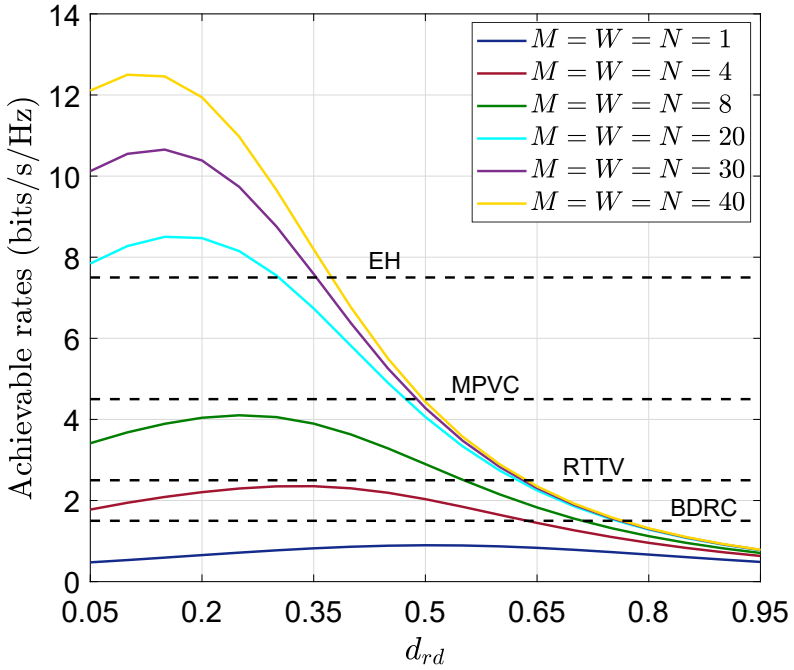

(b) $\mathrm{SNR}_{\mathrm{ref}} = -3$ dB

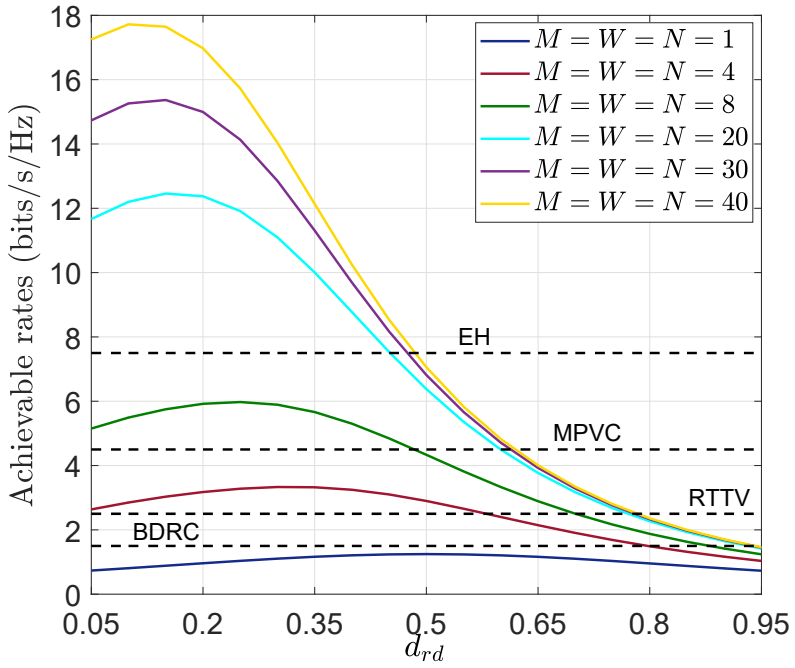

(c) $\mathsf{SNR}_{\text{ref}} = 0$ dB

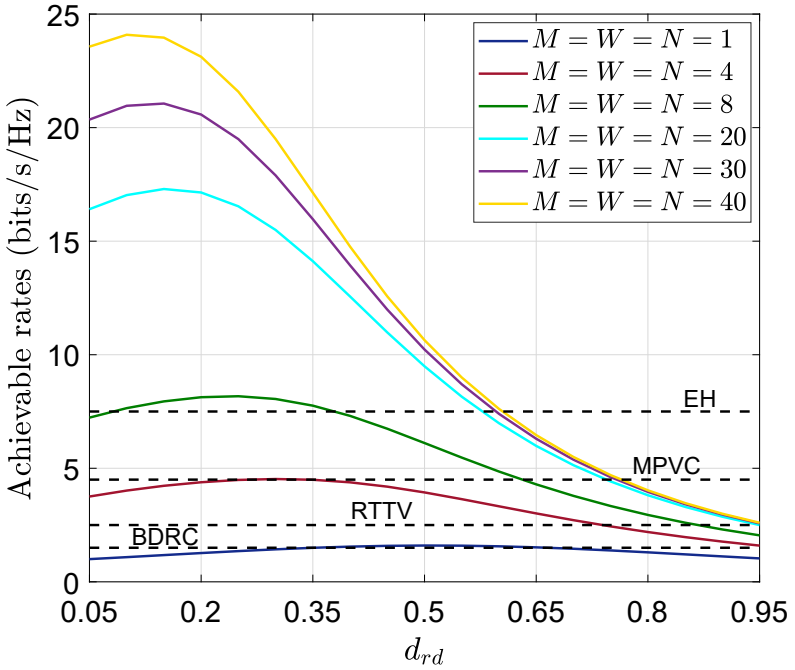

(d) $\mathsf{SNR}_{\text{ref}} = 3$ dB

FIGURE 4.11: Relation between the normalized relay location and the achieved rate at different SNR regimes and antenna configurations, considering $M = W = N$. The dotted lines represent the required rates of E-Health (EH), Multi-person video call (MPVC), Real–time thermal vision (RTTV) and Bi–directional remote controlling (BDRC) multimedia services when the available bandwidth is $B = 20$ MHz.